THE UNIVERSITY OF CHICAGO

BIDIRECTIONAL MULTI-PHOTON COMMUNICATION BETWEEN REMOTE SUPERCONDUCTING RESONATORS

A DISSERTATION SUBMITTED TO
THE FACULTY OF THE PRITZKER SCHOOL OF MOLECULAR ENGINEERING
IN CANDIDACY FOR THE DEGREE OF
DOCTOR OF PHILOSOPHY

BY
JOEL GREBEL

CHICAGO, ILLINOIS
JUNE 2023

CONTENTS

LIST OF FIGURES

LIST OF TABLES

ACKNOWLEDGMENTS

The University of Chicago community has been essential to completing this work. There are always temporary setbacks when doing experiments, but the supportive and collaborative environment both in our lab and the rest of the university made it possible to eventually succeed.

I'd like to first thank my advisor Andrew Cleland. His sharp but kind critiques during group meetings consistently improve the quality of our experiments. He is also an excellent teacher who is able to concisely explain complex topics in a manner that people new to the subject can understand.

Thanks as well to my thesis committee, Aashish Clerk and Alex High. My defense was a surprisingly nice experience.

When I joined the lab in 2015, the group had just moved from UCSB to UChicago and we had to set up the lab in a brand new building with a new cleanroom. Luckily we had two graduate students who made the move and helped with the transition. Kevin Satzinger taught me good cleanroom habits that were instrumental for completing my device fabrication. His systematic documentation of work and clear communication style was a model for how people would share information within our group. Greg Peairs set up the computer infrastructure for our lab. While we didn't share any experiments, he did help reintroduce me to my current favorite hobby.

A number of other graduate students started in the group at the same time as me. Youpeng Zhong built the electronics setup widely used in our lab for cryogenic measurements and wrote a python application we used to generate layouts for fabricating devices. He would also patiently explain how these useful tools work when asked and helped enhance them when needed. Hung-Shen Chang fabricated the first qubits in our lab at UChicago and was my desk neighbor for many years. Ming-Han Chou and I spent a lot of time in the cleanroom together for our respective projects, his complex fabrication procedures were impressive. Rhys Povey brought much of the UChicago community together with the many events that

he organized.

Two postdocs joined our lab in that first year. Étienne Dumur showed me that organized code is important for building large and useful applications. I also appreciated that he would organize group movie nights and rock climbing excursions. Audrey Bienfait was my primary mentor in my first few years as a graduate student. She was always willing to answer my many (many) questions. I aspire to do scientific work as quickly and meticulously as her.

It has been great to work with the graduate students that came later. Chris Conner and I worked together several times fixing the dilution refrigerators and upgrading the measurement code, he always kindly agreed to help with these necessary maintenance procedures. Haoxiong Yan's solid technical foundation made him an excellent person to bounce ideas off of. He also set up the electronics rack I used for my final experiment. It was fun to discuss different experimental topics with Yash Joshi due to his curious and social personality. Hong Qiao has an optimistic and practical approach to research which I found useful as I could be somewhat pessimistic about experiments. Jacob Miller helped export our lab wiki to its new home, our lab relies on it constantly for documentation. Xuntao Wu shared a two-person office with me in my final year. His enthusiasm for machine learning optimizers was infectious.

Our most recent postdoc Gustav Andersson freely shares his many creative experimental ideas. He successfully encouraged our group to eat more lunches together which I hope will continue.

I'd like to note several people in our school's administration and staff. Mary Pat McCullough made otherwise stressful administrative tasks much easier with her expert help. It would have been impossible to complete the fabrication in this work without Peter Duda's technical leadership at our cleanroom. Sally Wolcott managed the business side of the cleanroom and was a positive presence in the community. I enjoyed talking with Anna Mukhortova in the cleanroom when she was a process engineer during my first few years. Sunanda Prabhu-Gaunkar's mixtures of science and art were a pleasure to see.

I've had the opportunity to interact with a number of other students and postdocs outside our group. Elizabeth Ashley's honest perspectives about graduate life were refreshing to hear. Yuxin Wang came to nearly every journal club that I organized and contributed with good questions. The Awschalom group has been a friendly neighbor in the ERC LL2 basement with Paul Jerger, Alex Bourassa, Erzsebet Vincent, Kevin Miao, Sam Whiteley, Berk Diler and Yeghishe Tsaturyan. We have also been helped over the years by our fellow superconducting circuit researchers in the Schuster lab: Nate Earnest, Vatsan Chakram, Kan-Heng Lee, Tanay Roy, Ankur Agrawal, Sasha Anferov, Gabrielle Roberts, Kevin He, and Abigail Shearrow.

Finally, I'd like to thank my sister and parents for their love and support.

ABSTRACT

The field of quantum communication involves sending quantum states from one location to another. This has potential applications in building secure communication channels through quantum cryptography as well as in sharing resources between quantum computers that are part of a quantum network. Quantum communication protocols based on multi-photon states can support greater transmitted information density than those relying on single photon states. Bidirectional communication in a waveguide would further increase channel efficiency. At microwave frequencies, recent experiments have encoded multi-photon states in a superconducting resonator, deterministically transmitted them as wave packets into a waveguide, and captured them at remote nodes. However, while bidirectional communication has been demonstrated with single photon states, remote communication using multi-photon wave packets have been limited to a single propagation direction. In this thesis we present an experiment demonstrating bidirectional multi-photon transfers between two remote tunable resonators in a superconducting system, enabling single-pass on-demand transfers of photon superposition states. A second project is also presented that discusses the design and fabrication of a Josephson Parametric Amplifier with wide bandwidth, high gain, and low added noise. This amplifier incorporates innovations from previously demonstrated designs into a single device to improve performance while still being simple enough to fabricate in an academic cleanroom.

CHAPTER 1

INTRODUCTION

There are variety of quantum technologies currently being developed for a large number of potential applications. Reasonable people may disagree about the potential of specific technologies for specific applications, as well as the timeline for when they will be available for widespread use. However it is fascinating to see how quickly we are learning about what is possible and developing real devices. While these applications can sometimes blur lines between fields, we can divide quantum technologies into a few general categories: computation, communication, and sensing.

The goal of quantum computation is to leverage the large parameter space of many interacting quantum systems to provide a computational advantage over classical computing systems for a number of specific algorithms. Quantum computers were initially proposed for their potential to simulate other quantum systems more accurately [1]. It was later worked out that by constructively and destructively interfering the amplitudes of different states it is possible to solve certain computational problems faster than a classical computer [2, 3, 4, 5]. Due to the difficulty in isolating and controlling a large number of quantum systems, current quantum computers have not yet shown an advantage over classical computers for useful algorithms (although for some toy problems they have arguably passed this threshold [6, 7, 8]). This thesis will include one practical contribution to the development of these systems: a simple low noise and wide bandwidth amplifier. See Chapter 3 for more information and motivation for developing this device, and Chapter 4 for amplifier design and measurement.

A second major application for quantum technologies is sensing, where by reading out a small number of quantum systems we gather information about the environment. Quantum sensing is much more likely to have useful applications in the near future than quantum computing, because implementations rely on a much smaller number of quantum systems. While the entanglement between quantum systems and their environment is a disadvantage in quantum computing, this entanglement is a key feature in quantum sensing enabling

improved precision beyond what may be possible classically [9]. For example, by measuring multiple quantum systems at different points in space we can reconstruct magnetic and electric fields associated with biological systems in-situ [10]. This thesis is not particularly relevant for quantum sensing, but the topic is mentioned for completeness. For more information about quantum sensors see [9].

Finally, quantum communication involves transferring quantum states between remote nodes [11]. Early applications that are currently being constructed are primarily focused on cryptographic properties of quantum networks [12, 13]. However there may also be a need in the future for quantum computers to share complex quantum states between remote nodes in a quantum internet [14]. Quantum communication will be the second major focus of this thesis. See chapter 5 for additional motivation and background about our quantum network testbed for transmitting complex resonator states between remote cavities.

CHAPTER 2

SUPERCONDUCTING CIRCUIT OVERVIEW

This thesis will discuss the development of two classes of devices with relevant applications to quantum information science and engineering. The devices themselves are composed of individual parts that will be described in this chapter. Topics include the materials that make up the devices, models that describe how the components behave under reasonable operating conditions, and theoretical tools that enable us to combine systems together.

While the field of superconducting circuits is still relatively new compared to older disciplines such as quantum optics, it has started to accumulate a large body of knowledge that can be overwhelming to newcomers. To help navigate this large amount of information, review articles and theses are essential. Some useful general overviews of the field are [15, 16], and some theses of graduate students in our lab who worked with superconducting circuits [17, 18].

2.1 Materials

2.1.1 Superconductors

A superconductor is a material that when cooled below a certain critical temperature, has no direct current (DC) electrical resistance and expels fields of magnetic flux [19]. At these low temperatures, electrons in the material bind together as Cooper pairs [20]. These pairs form a condensate that can be described by a macroscopic wavefunction with well defined phase φ and approximately constant amplitude. The fact that the quantum behavior of a large number of particles can be fully described by φ is a powerful tool in designing circuits that exploit quantum phenomena.

The absence of DC resistance is a useful property that when combined with the Josephson effect (section 2.3.1) enables us to build superconducting circuits with low loss where the quantum properties of microwave electromagnetic fields can be directly observed and

manipulated. Apart from known coupling to external waveguides and dielectric loss, the remaining sources of loss in these systems are still being actively explored, however they are typically modeled as a distributed collection of two-level systems interacting with a given device, most likely present at the interfaces between substrates and vacuum [21]. The most common superconducting metals used in the field include aluminum (Al) and niobium (Nb), although tantalum (Ta) is an increasingly popular material used to make devices with lower loss [22, 23]. All devices described in this thesis use Al for the superconducting metal. Al has a critical temperature around 1.2 K [24] corresponding to a superconducting gap Δ_{Al} at 0 K of 0.18 meV[25]. This gap can be thought of as half the energy required to break a Cooper pair.

2.1.2 Dielectrics

Dielectrics are used as substrates for our devices, usually either sapphire or high resistivity silicon. We also use dielectrics as insulating materials for making multilayer structures. For example, a parallel plate capacitor can have a dielectric material supporting the top pad from the base layer metal. Among commonly used dielectrics at cryogenic temperatures and microwave frequencies, silicon dioxide (SiO_2) is approximately an order of magnitude lossier than silicon nitride (SiN) which is an order of magnitude lossier than amorphous silicon (a-Si) [26]. We use a combination of a-Si and SiN to create the capacitors and crossovers for the amplifier described in chapter 4.

Although SiO_2 has relatively high loss, it can be deposited as a temporary insulating layer that is removed at the end of a fabrication process using a vapor hydrofluoric acid (VHF) etch in order to create multilayer devices with low dielectric loss. We will use this "vacuum gap" process to form airbridges[1] in the resonator communication experiment discussed in chapter 5.

1. see section 2.2.5

2.2 Linear components

2.2.1 Waveguides

A signal line separated by an insulating gap from a ground plane lets a microwave signal propagate at a speed $v_w = \frac{c}{\sqrt{\epsilon_{\text{eff}}}}$, where c is the speed of light in vacuum, and ϵ_{eff} is the effective dielectric constant of the waveguide which is a function of the waveguide geometry as well as the dielectric constant of the substrate. Modeling the waveguide as a lossless transmission line [27], we can equivalently express the propagation velocity as $v_w = \frac{1}{\sqrt{L_w C_w}}$ as a function of the inductance per length L_w and capacitance per length to ground C_w as shown in Fig. 2.1a. The characteristic impedance of such a waveguide is given by $Z_w = \sqrt{\frac{L_w}{C_w}}$, so we can either design the transmission line properties using ϵ_{eff} and Z_w or L_w and C_w depending on the situation.

One of the simplest circuit geometries to fabricate on a two-dimensional plane is a co-planar waveguide (CPW)[27], requiring only a single photolithography step[2]. As the name suggests, a CPW consists of metal on a single layer as shown in Fig. 2.1b and c. ϵ_{eff} for a CPW is roughly given by the average of the dielectric constants of the substrate and free space above the CPW.

The relative width of the center conductor to the width of the gaps on the side control the waveguide impedance by varying C_w. A 2:1 center/gap ratio is approximately $50\,\Omega$ at microwave frequencies for a CPW on a sapphire substrate, with a capacitance per length $C_w = 173\,\text{pF/m}$ and inductance per length $L_w = 402\,\text{nH/m}$[18]. Note that these values are independent of the absolute size of the waveguide, but to efficiently use the space on a given chip the center and gap widths are usually a few μm. We target $50\,\Omega$ for many CPW lines because the external coaxial cables we connect to the sample are also $50\,\Omega$. Matching impedances minimizes signal reflections at connections [27]. This waveguide geometry corresponds with a signal velocity $v_t \approx 0.4 \cdot c \approx 1.2 \cdot 10^8 \text{m/s}$. In other words it takes a little over 8 ns for

2. See Appendix B for more information on fabricating devices in the cleanroom

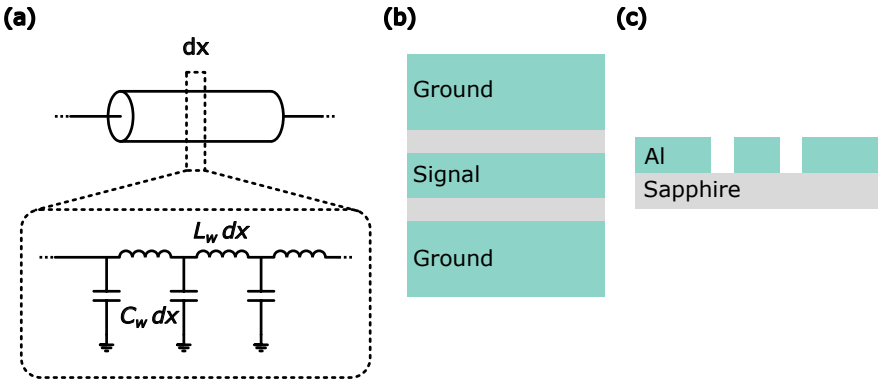

Figure 2.1: **Lossless transmission line and CPW.** **(a)** A lossless transmission line is modeled as being composed of alternating infinitesimal series inductances L_w and capacitances to ground C_w. As is depicted here, a cartoon of a coaxial cable is commonly used as a symbol for a transmission line where the inner line is the signal and the outer shell is ground. **(b)** Top and **(c)** side view of a coplanar waveguide (CPW). A CPW is formed from a single metal layer on top of an insulating substrate, here Al and Sapphire (Al2O3). The center trace is the signal line and is separated from ground planes on either side by a gap.

a signal to travel 1 m.

These waveguides connect between circuit components such as capacitors, inductors, and resonators as will be discussed in the following sections.

2.2.2 Inductors

Since a CPW section has an inductance per length L_t as mentioned in the previous section, we can make a lumped element inductor by using a section of CPW. Lumped element here means that the wavelength λ of the signal is much larger than the component, and so we can approximate the distributed inductances and capacitances as discrete circuit elements. For a signal frequency $f = 5\,\text{GHz}$, $\lambda = \frac{1}{f\sqrt{L_w C_w}} \approx 2.4\,\text{cm}$. Most of our circuit structures have sizes on the order of a few hundred μm and so are well within the lumped element regime. For larger structures such as the 2 m long waveguide used for the experiment in chapter 5, a single lumped element circuit description is not sufficient.

2.2.3 Capacitors

A capacitor can be made between separated metal sections either between two metal layers (parallel plate capacitor) or within a single metal layer (in-plane). In general, for a given target capacitance a parallel plate capacitor will take up less space on the chip and better confine electric fields than an in-plane capacitor. However, it is more challenging to fabricate parallel plate capacitors due to the additional process steps required to make multiple layers, and the intervening dielectric is usually lossier than a crystalline substrate. For this reason, we use in-plane capacitors for coupling between qubits and resonators. We also capacitively couple signal lines for coherently driving these components.

A parallel plate capacitor will be used for the amplifier presented in chapter 4. The capacitance C_p for a parallel plate capacitor is given by

$$C_p = \frac{\epsilon_d \epsilon_0 A}{d}, \tag{2.1}$$

where ϵ_d is the dielectric constant of the dielectric in between the metal plates, ϵ_0 is the electric constant, A is the area between the plates, and d is the plate separation. While the capacitance of a parallel plate capacitor can be well described by this equation, in-plane capacitances can be difficult to precisely predict without finite-element simulations.

2.2.4 Waveguide resonators

If we terminate a CPW line by either connecting the center to ground (a short) or ending it with a small capacitance to ground (an open), a signal will fully reflect off the end. If the waveguide has a short or an open on each end, the signal will form standing waves for certain signal frequencies (resonances). At the resonance frequency ω_0, at a short boundary the voltage will be zero (voltage node) and the current will oscillate between a maximum and minimum value (current antinode). Similarly, at an open boundary the current will be zero (current node) and the voltage will oscillate (voltage antinode). This behavior at

boundaries (and current/voltage nodes/antinodes in general) is used to couple components together, which means energy can transfer between them. Near voltage antinodes we can capacitively couple two components, and near current antinodes we can inductively couple two components.

A waveguide of length l that is shorted on both ends or open on both ends (half-wave resonator) can support resonances of signals with wavelengths $\lambda = \frac{2\pi c}{\omega_0\sqrt{\epsilon_{\text{eff}}}}$ that satisfy $l = \frac{n\lambda}{2}$, where n is a positive integer. A waveguide that has one end shorted and the other open (quarter-wave resonator) can support resonances of signals with wavelengths that satisfy $l = \frac{(2n+1)\lambda}{4}$ where n is an integer. These length formulas show that for a given ω_0 the shortest CPW resonator we can make will be $\lambda/4$. From a different equivalent perspective, a resonator of length l will support a spectrum of resonances separated by the resonator's free spectral range ω_{FSR}. For half-wave resonators $\omega_{\text{FSR}\lambda/2} = \frac{\pi c}{l\sqrt{\epsilon_{\text{eff}}}}$ while quarter-wave resonators will have $\omega_{\text{FSR}\lambda/4} = \frac{\pi c}{2l\sqrt{\epsilon_{\text{eff}}}}$

Near a resonance frequency ω_0, waveguide resonators can be modeled using lumped element electrical components [27]. These circuit models make it simpler to numerically simulate devices and predict their properties. Depending on the waveguide resonator they can be modeled as a capacitor C, inductor L, and resistor R either in series or in parallel with each other. The resonant frequency of an RLC resonator is given by $\omega_0 = \frac{1}{\sqrt{LC}}$ and has a characteristic impedance of $Z_r = \sqrt{\frac{L}{C}}$. Table 2.1 summarizes the RLC models of several waveguide resonators. The derivations are similar to those in chapter 6 of [27], generalized for the nth mode of each resonator using the lengths defined above. The internal quality factor $Q_i = \frac{\beta}{2\alpha}$, where $\beta = \frac{\omega}{v}$ and α the loss, is a dimensionless characterization of the loss in a resonator. For series resonators, $Q_i = \frac{\omega_0 L}{R}$ and for parallel resonators $Q_i = \omega_0 RC$.

Type	RLC model	L	C	R
2 short	Series	$\frac{nZ_0\pi}{2\omega_0}$	$\frac{2}{nZ_0\pi\omega_0}$	$\frac{nZ_0\pi}{2Q_i}$
2 open	Parallel	$\frac{2Z_0}{n\pi\omega_0}$	$\frac{n\pi}{2\omega_0 Z_0}$	$\frac{2Q_iZ_0}{n\pi}$
1 open 1 short (coupling near open)	Parallel	$\frac{4Z_0}{(2n+1)\pi\omega_0}$	$\frac{(2n+1)\pi}{4\omega_0 Z_0}$	$\frac{4Q_iZ_0}{(2n+1)\pi}$
1 open 1 short (coupling near short)	Series	$\frac{(2n+1)Z_0\pi}{4\omega_0}$	$\frac{4}{(2n+1)Z_0\pi\omega_0}$	$\frac{(2n+1)Z_0\pi}{4Q_i}$

Table 2.1: **CPW resonator lumped element models.** Modeling waveguide resonators as *RLC* lumped element resonators near their resonant frequencies. Depending on the type of resonator, the lumped element components are either combined in series or in parallel. Z_0 is the characteristic impedance of the CPW line, ω_0 the resonant frequency, and n the harmonic mode of the resonator.

The effective dielectric constant ϵ_{eff} for a resonator may be affected by additional loading circuit elements on the waveguide, such as crossovers. For equally spaced airbridge crossovers, each with capacitance to ground[3] 1 aF, the frequency of a quarter-wave resonator at around 5 GHz will decrease linearly by about 2.5 MHz for each added crossover. Dielectrics in the crossovers would linearly increase this effect as well.

CPW waveguide resonators made of superconductors with thicknesses ~ 100 nm without Josephson junctions (section 2.3.1) behave linearly to a good approximation[4]. Modeling the circuit classically, one way of describing a linear resonator is that the equivalent inductance and capacitance of the resonator derived from a lumped-element model[5] near a resonance frequency will not depend on the energy contained in the resonator. Modeling the circuit using quantum theory, a linear resonator's resonances (modes) can be well approximated

3. 1 aF is approximately the capacitance for a 6x4 μm^2 airbridge as used for the experiments in chapter 5

4. Designing the waveguide to have high kinetic inductance [28] is another way to have nonlinearity apart from Josephson junctions

5. Note that each resonator mode has a different lumped-element model representation

by the quantum harmonic oscillator[6]. For more details on the quantization of a classical electromagnetic resonator, see [29, 30].

A quantum harmonic oscillator is a system with infinite equally spaced energy levels and has the Hamiltonian

$$H = \hbar\omega_0 \left(a^\dagger a + \frac{1}{2} \right), \tag{2.2}$$

where a is the lowering operator with $[a, a^\dagger] = 1$. We can also write the harmonic oscillator's Hamiltonian in terms of its lumped element inductance L and capacitance C, with charge Q on C and flux Φ through L [17]

$$H = \frac{Q^2}{2C} + \frac{\Phi^2}{2L}, \tag{2.3}$$

where Q and Φ obey the commutation relation $[Q, \Phi] = i\hbar$. We can relate a to the resonator's lumped element parameters with

$$a = \frac{1}{\sqrt{2\hbar}} \left(\sqrt{\frac{C}{L}}\Phi + i\sqrt{\frac{L}{C}}Q \right). \tag{2.4}$$

2.2.5 Airbridges

A crossover is a bridge of metal that galvanically connects (direct electrical connection) the ground planes on either side of a CPW line. These bridges reduce the impedance between the ground planes, which increases the frequency of spurious modes away from the device frequencies [31]. Multilayer crossovers can be made by first depositing a dielectric insulator and then depositing a top metal layer on top forming the bridge. The dielectric is placed directly on the transmission line, and so it can contribute to unwanted loss in the circuit. Crossovers with no dielectric below the top metal layer are called airbridges. We follow a

6. It is a tradition that every thesis related to superconducting circuits must include an introduction to the quantum harmonic oscillator

similar process for fabricating airbridges as in [32], with a 200 nm SiO_2 height instead of 1 μm. The advantage of an airbridge with a lower height is that the fabrication process is simpler, however due to the new fabrication process we should check that these airbridges do not contribute to resonator loss.

The characterization measurement for the airbridges is shown in Fig. 2.2. As a proxy for the loss contributed by each airbridge, we measure the internal quality factor Q_i of several CPW resonators inductively coupled to a measurement line. The normalized transmission $\tilde{S}_{21}$ for an inductively coupled, quarter-wave resonator is given by [17]

$$\frac{1}{\tilde{S}_{21}} \approx 1 + \frac{Q_i}{Q_c^*} e^{i\phi} \frac{1}{1 + i2Q_i \delta x}, \tag{2.5}$$

where by $\tilde{S}_{21}$ is normalized to give off-resonant transmission $|\tilde{S}_{21}| = 1$, Q_c^* is a rescaled coupling factor due to normalization [33](will just be referred to as Q_c), ϕ is the phase, and $\delta x = (\omega - \omega_0)/\omega_0$. By fitting the transmission data through the measurement line as a function of the signal frequency (Fig. 2.2) we can extract Q_i for different powers P incident on the resonator. P can be roughly estimated by dividing the values of the attenuators along the input line from the VNA output power. For our inductively coupled quarter-wave resonators, the average photon number in the resonator due to P is given by [17]

$$n = \frac{2Q_c}{\omega_0} \left(\frac{Q_i}{Q_i + Q_c} \right)^2 \frac{P}{\hbar \omega_0}. \tag{2.6}$$

Fig. 2.2 shows data from two experiments with eight CPW resonators each that had different numbers of airbridges on each resonator. Q_i increases with P due to saturation of two-level systems weakly coupled to the resonator [33]. At low photon powers we can see that for a short 30 s VHF etch there is significant variation in the resonator loss between resonators with Q_i ranging from roughly 10^4 to 10^5. This corresponds to a $T_1 = \frac{Q_i}{\omega_r} \approx 0.4\,\mu$s to 4 μs for $\omega_r/2\pi = 4$ GHz. For a longer 3 min. VHF etch the Q_i of these lower height airbridges does not depend on the airbridge spacing indicating airbridges no longer dominate the loss

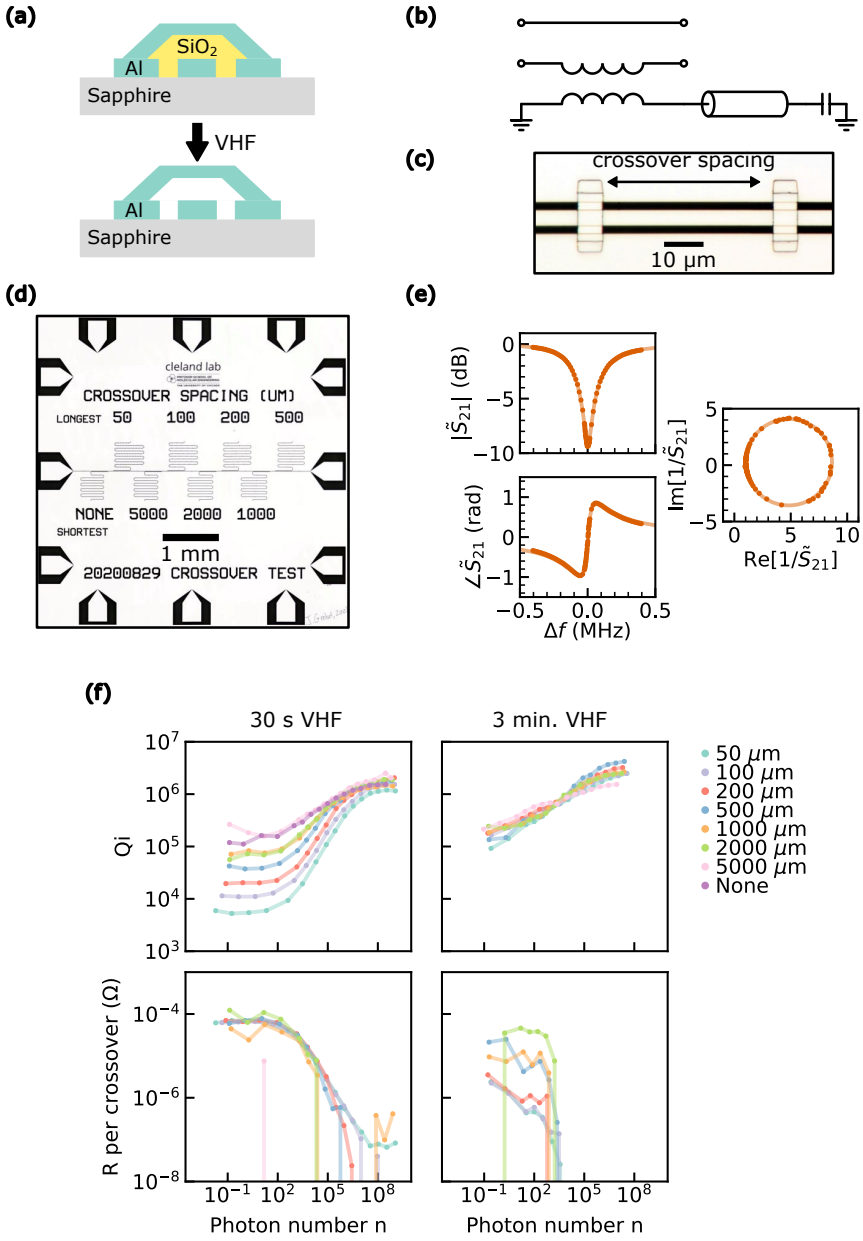

Figure 2.2: **Airbridge loss test (a)** Side-cut cartoon of airbridge fabrication. An SiO2 crossover has three layers formed by an Al base, SiO2 dielectric, and Al top layer. A vapor HF (VHF) etch releases the crossover to form an airbridge. **(b)** Circuit diagram of resonator test of airbridge loss **(c)** Microscope image of CPW with crossovers. The spacing between crossovers/airbridges are varied in the test. **(d)** Microscope image of the test chip. **(e)** Example $\tilde{S}_{21}$ data (points) and fit (line) to 1000 μm spacing resonator at population $n \approx 2000$, with $Q_i \approx 1.5 \times 10^5$ **(f)** The quality factor and calculated resistance per crossover of resonators with different crossover spacings is plotted as a function of photon number in the resonators, for both a 30 s and 3 min. VHF etch. For the 30 s etch, increasing the density of crossovers clearly increases the resonator loss, and the resistance per crossover can be calculated at low power. For the 3 min. VHF etch, within a factor of two all resonators have similar quality factors, and resistance per crossover does not show a clear trend.

in the device.

2.3 Nonlinear components

When going through different overviews and introductions of the superconducting circuit field [16, 15] it is striking how much of the field can be described as interacting resonators with some added nonlinearity. The complexity that comes from this nonlinearity both enables interesting new applications and is a constant source of difficulties. For the circuit designer, the challenge is then choosing the correct amount of nonlinearity needed for a given application. After first reviewing some fundamental nonlinear components we will incorporate them into a variety of resonant structures.

2.3.1 Josephson junctions

For the purposes of this thesis, a Josephson junction can be thought of as a nearly lossless nonlinear inductor. In contrast to typical linear inductors, whose inductance is the same for any applied current, the Josephson junction's effective inductance L_J varies with the magnitude of an applied current [34]

$$L_J(I_J) = L_{J0}\frac{1}{\sqrt{1-(I_J/I_c)^2}} \tag{2.7}$$

$$= L_{J0}\left[1+\frac{1}{2}\left(\frac{I_J}{I_c}\right)^2+\cdots\right], \tag{2.8}$$

where $L_{J0} = \frac{\Phi_0}{2\pi I_c}$ is the Josephson Inductance, $\Phi_0 = \frac{h}{2e}$ is the flux quantum, h is Planck's constant, e is the electron charge, and I_c is the Josephson junction's critical current. When the current rises above the Josephson junction's critical current, the junction is no longer lossless.

More fundamentally, a Josephson tunnel junction is made whenever two bulk superconducting materials are separated by a thin insulating barrier [35], shown in Fig. 2.3c. The

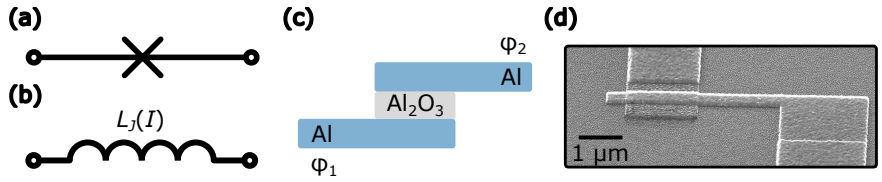

Figure 2.3: **Josephson junctions (a)** The electrical circuit symbol for a Josephson junction is an X. **(b)** The junction can be modeled as an inductance with value L_J as defined in the main text. **(c)**Josephson junctions are formed by placing an insulating barrier between two superconducting metals, here the metals are both Al and the insulating barrier is Al oxide, formed by oxidizing Al. The superconducting metal on either side of the insulating barrier has phases φ_1 and φ_2.**(d)** Scanning Electron Microscope (SEM) image of a Josephson junction.

macroscopic phase φ of the superconductor changes across the junction. This phase difference $\delta = \varphi_1 - \varphi_2$ determines the junction's current I_J and voltage V_J through the Josephson relations [19]

$$I_J = I_c \sin(\delta) \tag{2.9}$$

$$V_J = \frac{\Phi_0}{2\pi}\frac{d\delta}{dt}, . \tag{2.10}$$

We can derive the nonlinear inductance stated in Eq. 2.7 by noting that $L_J = I_J \left(\frac{dI_J}{dt}\right)^{-1}$.

We could also model a capacitance C_J and resistance R_J in parallel with the inductance L_J for Josephson junctions as described by the resistively and capacitively shunted junction (RCSJ) model [36, 37]. We can estimate an order of magnitude for C_J by modeling a junction as a parallel plate capacitor with an area $A = 0.2\,\mu\text{m} \times 1\,\mu\text{m} = 0.2\,\mu\text{m}^2$, dielectric constant $\epsilon_d = 11.4$ for Al_2O_3 at GHz frequencies, and $d \approx 2\,\text{nm}$ for the oxide thickness. Using Eq. 2.1 we get $C_J \approx 2\,\text{fF}$ which is small enough to ignore for the experiments here. Similarly, while there may be loss associated with the junction we don't have precise values for R_J and so will lump it into the total loss of the component it is associated with.

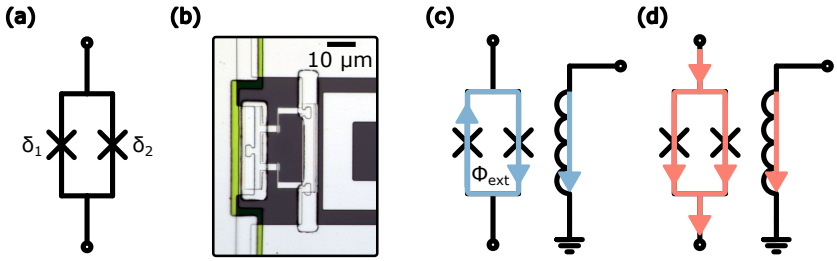

Figure 2.4: **DC SQUID. (a)** A DC SQUID is made with two Josephson junctions in a loop, with phase differences across each junction δ_1 and δ_2. **(b)** A microscope picture of a SQUID, used in the amplifier from chapter 4. **(c)** A current generated on an on chip flux line generates a current that circles around the SQUID loop. From an alternative perspective, the flux line generates a flux Φ_{ext} that passes through the loop **(d)** We would like to minimize coupling to stray coupling current that goes through both junctions in the same direction.

2.3.2 DC SQUID

When two Josephson junctions interrupt a loop of superconducting metal, the inductance of the loop L_s becomes a function of the amount of external magnetic flux threading the loop Φ_{ext}. If both junctions have identical critical current I_c, L_s can be written as [38]

$$L_s\left(\Phi_{\text{ext}}\right) = \frac{\Phi_0}{4\pi I_c \cos\left(\pi \frac{\Phi_{\text{ext}}}{\Phi_0}\right) \sin\left(\delta\right)}, \tag{2.11}$$

where $\delta = \frac{\delta_1+\delta_2}{2}$ is the average of the phase differences δ_1, δ_2 across the two junctions. By routing on-chip control lines near these loops, we can dynamically control the magnetic flux Φ_{ext} and thus the loop inductance, and as a result the resonance frequency of the resonator that the loop is part of (Fig. 2.4c). We use SQUIDs as part of our qubits, amplifiers, and tunable resonators.

We simulate SQUIDs during the design process[7] to maximize the coupling to the SQUID so that we can tune our devices with smaller currents. We also want to minimize stray coupling where current flows parallel to both junctions, as this can introduce additional complicated dynamics when parametrically driving the SQUID as discussed in section 3.4.

7. using software such as Sonnet or HFSS for example

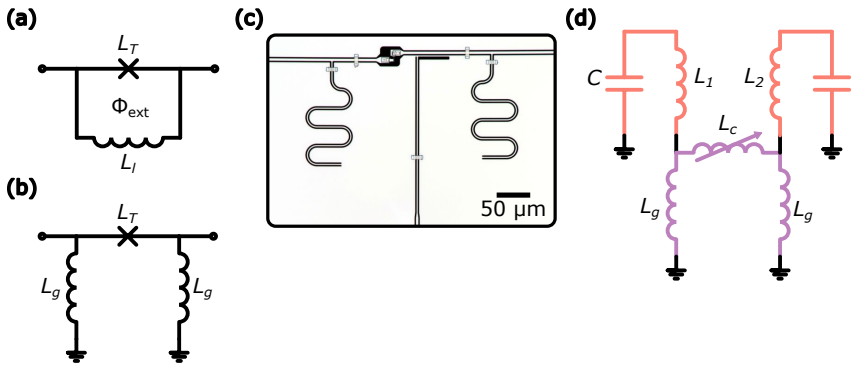

Figure 2.5: **RF SQUID and Tunable Coupler. (a)** The phase drop δ across RF SQUID junction is a function of the junction inductance L_T, the loop's linear inductance L_l, and the external flux Φ_{ext} applied to the loop. **(b)** The tunable inductive coupler is an RF SQUID with two equal inductances L_g to ground **(c)** A microscope picture of the tunable coupler, showing two CPW inductors to ground, a central flux line, and many crossovers to ensure currents flow across ground planes correctly. This coupler is used for the experiment in chapter 5. **(d)** At low photon powers and weak coupling we can estimate the coupling between two LC resonators (red) (capacitance C and inductances L_1 and L_2) by modeling the coupler (purple) junction as a tunable inductance with the value $L_c = L_T/\cos(\delta)$, where δ can be solved for as a function of external flux in Eq. 2.12

2.3.3 RF SQUID

When a single Josephson junction interrupts a loop of superconducting metal, the effective loop inductance also varies as a function of external bias (shown in Fig. 2.5a) with the phase δ and external flux bias Φ_{ext} related by [39]

$$\delta + \frac{L_l}{L_T}\sin(\delta) = 2\pi\frac{\Phi_{\text{ext}}}{\Phi_0}, \tag{2.12}$$

where L_l is the linear inductance of the loop and L_T is the junction inductance when $\delta = 0$ (L_{J0}).

2.3.4 Tunable coupler

We use RF SQUIDs for making inductive couplers between various circuit elements with a tunable coupling strength (Fig. 2.5c). Originally designed for coupling two transmon qubits together [40, 39] these couplers have also been used for coupling qubits to a surface

acoustic wave resonator [41] and delay line [42, 43], and superconducting transmission lines [44, 45, 46]. As shown in Fig. 2.5b, the coupler includes a junction with bare inductance L_T and two linear inductances to ground with value L_g.

For this and the components that will be discussed later, we would like to operate them in a linear regime, and then add nonlinearity for more accurate calculations if necessary. In the case of this coupler, if it is placed between two LC resonators with low average photon numbers as shown in Fig. 2.5d, the effective mutual inductance will be approximately [47, 18]

$$M = \frac{L_g^2}{2L_g + L_w + L_T/\cos\delta}, \tag{2.13}$$

where δ is the phase difference across the junction and $L_w \approx 0.1\,\text{nH}$ accounts for any stray linear inductance due to wiring in the loop. The coupling g (for weak coupling) is then

$$g = \frac{M}{2}\sqrt{\frac{\omega_1\omega_2}{(L_g + L_1)(L_g + L_2)}}. \tag{2.14}$$

This expression comes from quantizing [30] two inductively coupled LC resonators, and rewriting the interaction term in the form $\hbar g(a_1 + a_1^\dagger)(a_2 + a_2^\dagger)$ using Eq. 2.4. As is done in section 5.1.1 we can also use the linearized coupler circuit directly in circuit simulations to calculate resonator loss due to coupling to an infinite transmission line.

When designing these couplers, it is useful to note the two limits of the junction inductance L_T. If the junction inductance is large relative to the linear inductance ($L_T \gg L_l$), the range of coupling magnitudes will be small. When $L_T < L_l$, the loop enters a hysteretic regime in Eq. 2.12 and also limits the coupling strength [17].

2.3.5 Transmon Qubit

For the purposes of quantum computation we would like a good qubit. A qubit is a two-level quantum system whose state can be initialized, read out, arbitrarily controlled, and has a long lifetime [48]. For applications in quantum communication, we additionally would like

to send the qubit's information through a waveguide to a different qubit.

If we label the two levels of the qubit as $|g\rangle$ and $|e\rangle$, the state of the qubit $|\psi_q\rangle$ is given by $|\psi_q\rangle = \alpha|g\rangle + \beta|e\rangle$. Because $|\psi_q\rangle$ is a pure state, $|\alpha|^2 + |\beta|^2 = 1$. One common representation of a qubit state is the Bloch sphere as shown in Fig. 2.6b, in which the qubit state is defined as a vector located on the surface of the sphere[8]. We can equivalently define α and β in terms of variables θ and ϕ with $\alpha = \cos\frac{\theta}{2}$, $\beta = e^{i\phi}\sin\frac{\theta}{2}$, where on the Bloch sphere θ is the polar angle while ϕ is the azimuthal angle. In Cartesian coordinates the state of the qubit will then be given by $x = \sin\theta\cos\phi, y = \sin\theta\sin\phi, z = \cos\theta$. Changing the state of a qubit involves rotating the state vector around the Bloch sphere, for example a π pulse involves a $\theta = \pi$ rotation around an axis in the xy plane while a $\pi/2$ pulse means $\theta = \pi/2$.

In the field of superconducting circuits we do not typically make qubits out of systems that have only two levels. Instead we make nonlinear resonators (Fig. 2.6a), where the frequency ω_{ge} of a microwave drive required to excite the resonator from its ground state $|g\rangle$ to its first excited state $|e\rangle$ is different than the frequency ω_{ef} needed to go from $|e\rangle$ to the second excited state $|f\rangle$. If the nonlinearity is weak, we can represent the Hamiltonian of such a nonlinear resonator in terms of its anharmonicity $\alpha = \omega_{ef} - \omega_{ge}$ [15],

$$H = \hbar\omega_{ge}a^\dagger a + \frac{\alpha}{2}a^\dagger a^\dagger aa. \tag{2.15}$$

For a high enough α we can ignore higher energy levels and approximate the nonlinear resonator as a two level system by staying in the lowest two energy levels.

One widely used superconducting qubit is the transmon[9] [50]. As shown in Fig. 2.6c a frequency-tunable transmon has a similar circuit as an LC oscillator but with the inductor replaced with a SQUID[10]. Varying the flux through the SQUID changes its effective inductance L_s and the resonance frequency of the resonator. The Hamiltonian is

8. For a more general mixed state representation of the qubit, the vector will be located inside the sphere

9. The transmon is a special form of a Cooper pair box [49]

10. Instead of the SQUID a transmon may also have only a single Josephson junction. In that case the transmon would not be tunable, but would also be less sensitive to magnetic flux noise

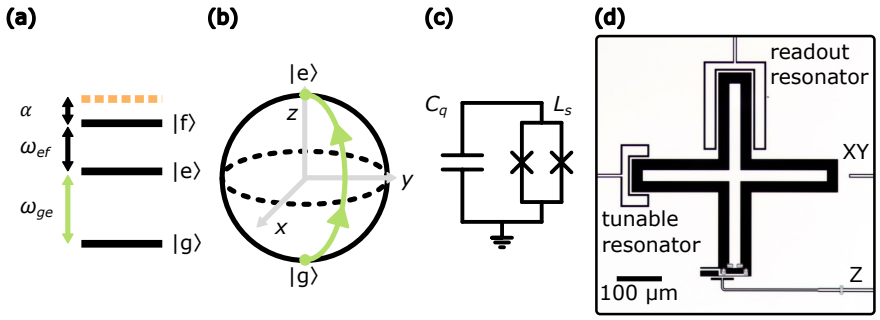

Figure 2.6: **Transmon qubit.** **(a)** Qubit energy levels showing frequencies ω_{ge} and ω_{ef} required to excite the qubit from states $|g\rangle \rightarrow |e\rangle$ and $|e\rangle \rightarrow |f\rangle$, respectively. The transition frequency $\omega_{ef} = \omega_{ge} + \alpha$, where α is the anharmonicity, which is negative for transmons. **(b)** Bloch sphere representation of a qubit, with pure states represented as a vector on the surface and mixed states inside. Applying a drive at ω_{ge} (XY drive) rotates a state around an axis in the XY plane. Tuning the qubit frequency varies the phase (Z rotation) in the qubit's reference frame (not shown).**(c)** Circuit for grounded transmon qubit with capacitance C_q and tunable inductance L_s. **(d)** Microscope of a qubit used for the experiment in chapter 5. Flux line for qubit Z (frequency) tuning is shown at the bottom, capacitively coupled XY (microwave) drive line on the right, capacitively coupled readout resonator on top, and capacitively coupled tunable resonator to the left.

$$H = \frac{Q^2}{2C_q} - \frac{\Phi_0}{2\pi} I_0(\Phi_{\text{ext}}) \cos(\delta). \tag{2.16}$$

The transmon design optimizes the choice of C_q and I_0 to minimize the qubit's sensitivity to charge noise, while keeping sufficient anharmonicity to maintain the two-level approximation. We make transmon qubits using a planar capacitor (capacitance C_q) and a DC SQUID with equal junctions (tunable critical current $I_0(\Phi_{\text{ext}}) = 2I_c \cos(\pi \frac{\Phi_{\text{ext}}}{\Phi_0})$), following the Xmon design [40]. The Xmon design[11] provides a specific planar geometry that makes it straightforward to couple to other systems with either capacitive or inductive coupling.

The transmon Hamiltonian can also be written in terms of energies E_c and E_J as [15]

$$H = 4E_c n^2 - E_J \cos(\delta), \tag{2.17}$$

11. The Xmon grounds the bottom capacitor plate and SQUID, however there are other transmon designs that leave both metal islands electrically floating

where $E_c = \frac{e^2}{2C_q}$ is the charging energy, with e the single electron charge, $n = Q/2e$ is the number of Cooper pairs on C_q, and C_q should technically be a sum of all the capacitances including the junctions' but we approximate as just that of the planar capacitor. $E_J = \frac{I_0\Phi_0}{2\pi}$ is the Josephson energy. To be in the transmon regime, we require $E_J \gg E_c$. We usually design the qubit anharmonicity[12] $\alpha_q = -E_c$ to be around 215 MHz with $C_q = 90$ fF. For a qubit with a resonance of around $\omega_q/2\pi = \left(\sqrt{8E_JE_C} - E_C\right)/h = 5$ GHz we can check that $E_J/E_C = 68$, so we are in the correct regime for our usual qubit operating frequencies.

2.3.6 Tunable Resonator

An ideal tunable resonator would be a linear harmonic oscillator with long lifetime whose frequency we can arbitrarily control. A CPW resonator can be made with long lifetimes and a SQUID is a tunable inductor, so combining these elements is one way of making tunable resonators [51, 52]. The addition of the SQUID does add some undesired nonlinearity though, and this will need to be accounted for in our models. For the experiments that will be discussed here, the SQUID was placed near the end of the resonator, however it is also possible to get tunability with the SQUID in the middle [53]. For small detunings from zero flux bias it is possible to approximate the resonator using a lumped element model from table 2.1. However, the approximations used in deriving the lumped element models breaks down for larger detunings and it becomes necessary to use a more complete transmission line model.

If the SQUID is placed on the shorted end of a quarter-wave resonator, we can vary the shorted end boundary condition from approximately shorted to approximately open by varying the SQUID inductance from small to large as shown in Fig. 2.7. This tunes the resonator frequency between that of a quarter-wave resonator $\omega_{\lambda/4} = \frac{(2n+1)\pi c}{2l\sqrt{\epsilon_{\text{eff}}}}$ to a half-wave resonator of the same length $\omega_{\lambda/2} = \frac{n\pi c}{l\sqrt{\epsilon_{\text{eff}}}}$, for a maximum possible range of $\omega_{\lambda/4} - \omega_{\lambda/2} = \frac{\pi c}{2l\sqrt{\epsilon_{\text{eff}}}}$. In practice, the tuning range is effectively smaller than this because

12. this expression is true to first order approximation

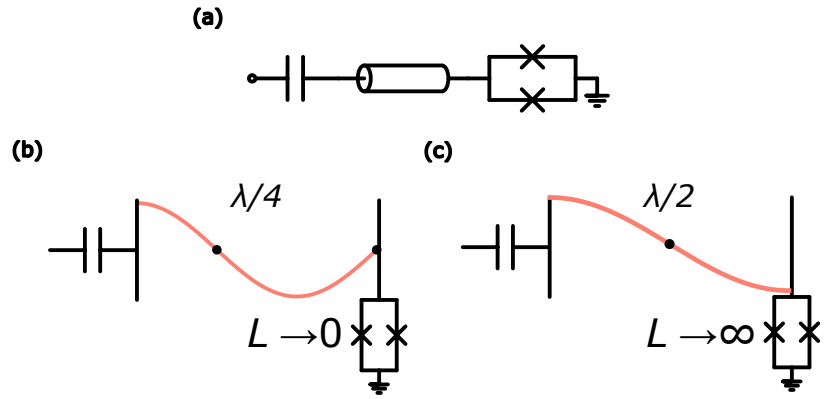

Figure 2.7: **Tunable CPW Resonator.** **(a)** Tunable resonator circuit. **(b)** When the SQUID inductance is small, the boundary condition is a short and the resonator has a $\lambda/4$ resonance. **(c)** When the SQUID inductance is large the boundary condition is an open and the resonator has a $\lambda/2$ resonance which is at a lower frequency than the corresponding $\lambda/4$ resonance in (b)

the resonator lifetime tends to go down at single photon energies with larger detunings [54].

As a weakly nonlinear resonator, we can model the Hamiltonian using Eq. 2.15, however due to the extra linear inductance from the waveguide it does not take the same form as a transmon as in Eq. 2.16. Ref. [55] helpfully derives a nonlinear correction to the tunable resonator energy levels as a function of the resonator tuning parameters. Here we summarize some useful relations from that paper and express them as the resonator anharmonicity α_r as a function of the resonator frequency $f_r = \omega_r/2\pi$. We can describe the tuning in terms of βl at resonance, which for a quarter-wave resonator is $\beta l = \frac{(2n_i+1)\pi}{2}$ and for the half-wave resonator is $\beta l = n_i\pi$, with n_i an integer representing the resonator mode. The resonator's effective capacitance C_r (ignoring junction capacitance) and inductance L_r are

$$C_r(\beta l) = \frac{C_{\text{cav}}}{2}\left(1 + \frac{\sin(2\beta l)}{2\beta l}\right) \tag{2.18}$$

$$L_r(\beta l) = \frac{L_{\text{cav}}C_{\text{cav}}}{(\beta l)^2 C_r}, \tag{2.19}$$

where $C_{\text{cav}} = l\mathscr{C}$ and $L_{\text{cav}} = l\mathscr{L}$ are the cavity capacitance and inductance, and $\mathscr{C} =$

173 pF/m and $\mathscr{L} = 402$ nH/m are the capacitance/inductance per length for a 2:1 center:gap CPW on sapphire [18]. Assuming a fixed length $l = 20.5$ mm (used for the communication experiment in this thesis), we can convert βl to the resonance frequency ω_r using

$$\omega_r = \frac{\beta l}{\sqrt{C_{\text{cav}} L_{\text{cav}}}}. \tag{2.20}$$

The energy deviation δE_{n_l} of the n_lth resonator level to first order from the linear resonator is [55]

$$\delta E_{n_l} = \frac{-\left(6n_l^2 + 6n_l + 3\right)}{4} B_k E_C \tag{2.21}$$

$$B_k = \frac{(1/4)\cos^2(\beta l)}{1 + 2\beta l/\sin(2\beta l)}, \tag{2.22}$$

where $E_C = \frac{e^2}{2C_r}$. The anharmonicity α_r is then given by the deviation of the first and second levels from the ground and first level, noting that we need to convert energy to frequency via $\omega = E/\hbar$, as

$$\hbar\alpha_r = (\delta E_2 - \delta E_1) - (\delta E_1 - \delta E_0). \tag{2.23}$$

Plotting α_r in Fig. 2.8 we see that at higher modes (shaded green areas) the anharmonicity is smaller throughout a full tuning range. This is good motivation for operating at a higher mode other than the fundamental. Something to keep in mind is that longer resonators have a smaller tunable range within each mode and take up more space on the chip which increases the probability of fabrication issues. This smaller tunable range is not necessarily bad, as it can be useful in certain scenarios such as coupling the resonator to a transmission line (See chapter 5 for more info) where we would like to compensate for the frequency detuning that occurs when loaded by an external circuit.

Another method for reducing the anharmonicity is to replace the single SQUID with an array of SQUIDs. For an array of M Josephson junctions with the same effective Josephson energy, the anharmonicity is decreased from α to $\frac{\alpha}{M^2}$[56]. We decided not to make devices

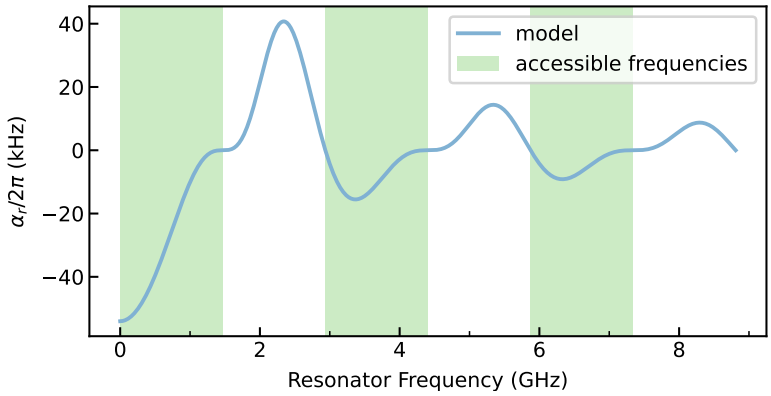

Figure 2.8: **Tunable resonator anharmonicity** Model for tunable resonator anharmonicity $\alpha_r/2\pi$ using Eq. 2.23 for a resonator of fixed length 20.5 mm for a 2:1 center:gap CPW on sapphire (see text). The tunable frequency range for the three lowest resonator modes are highlighted in green.

with junction arrays because more junctions in a device is associated with lower fabrication yield.

2.4 Resonators coupled to other systems

2.4.1 Qubit/resonator interaction

For the devices in this thesis, a superconducting qubit interacting with a resonator can be described by the Jaynes-Cummings Hamiltonian [15]

$$H_{JC} = \omega_r \left(a^\dagger a + \frac{1}{2} \right) + \frac{\omega_q}{2} \sigma_z + g \left(\sigma_+ a + \sigma_- a^\dagger \right), \tag{2.24}$$

where g is the qubit/resonator coupling strength, $\sigma_\pm = (\sigma_x \mp \sigma_y)/2$, and $\sigma_x, \sigma_y, \sigma_z$ are the x, y, z Pauli operators acting on the qubit. The Jaynes-Cummings Hamiltonian comes from applying the rotating-wave approximation[13] to a dipole interaction between a qubit and resonator.

If the qubit and resonator have a large frequency detuning with weak coupling ($\Delta \gg g$)

13. This essentially assumes energy conservation at relatively weak coupling

the system can be described by the dispersive Hamiltonian[14] [16]

$$H_{\text{disp}} = (\omega_r + \chi\sigma_z)\left(a^\dagger a + \frac{1}{2}\right) + \frac{\tilde{\omega_q}}{2}\sigma_z, \tag{2.25}$$

where $\tilde{\omega_q} = \omega_q + \chi$ is the Lamb shifted qubit frequency,

$$\chi = \frac{-g^2}{\Delta}\left(\frac{1}{1 + \Delta/\alpha}\right) \tag{2.26}$$

is the dispersive shift with a correction due to the transmon anharmonicity α, and Δ is the qubit-resonator detuning. If a qubit initially in its ground state $|g\rangle$ is excited to $|e\rangle$, a resonator dispersively coupled to it will change its frequency by 2χ. This useful property is used for reading out qubit states (see section 3.1.1)

2.4.2 Input-output theory for a resonator coupled to a waveguide

We model the emission and capture of a quantum signal from a resonator into a waveguide by following the formalism introduced in [58]. The resonator takes the place of the system Hamiltonian $\hat{H}_s$, interacting with an input field $\hat{b}_{\text{in}}$ and emitting into an output field $\hat{b}_{\text{out}}$. Input-output theory [59] tells us that $\hat{b}_{\text{in}}$ and $\hat{b}_{\text{out}}$ are related to each other with the relation

$$\hat{b}_{\text{out}(t)} = \hat{b}_{\text{in}(t)} + \sqrt{\gamma}\hat{c}(t), \tag{2.27}$$

where γ is the decay rate of excitations from the resonator to the waveguide[15] and $\hat{c}$ is the resonator's lowering operator. The input and output wave packets are modeled as two virtual cavities coupled to the resonator. The couplings between the virtual cavities and the resonator are set as time-dependent functions that ensure the resonator evolves like it is absorbing from and emitting into specific wave packet shapes in the waveguide.

14. See Appendix A in [57] for a good derivation of this expression

15. γ may be time dependent, as when we modulate the coupling of our resonator to the waveguide

Given an arbitrary time dependent pulse shape $u(t)$ in the waveguide, $u(t)$ can be emitted from or absorbed into a cavity with a time-dependent complex coupling $i[g^*(t)\hat{a}\hat{b}_{\text{in}}^\dagger - g(t)\hat{a}^\dagger\hat{b}_{\text{in}}]$ where $\hat{a}$ is the lowering operator of either the input or output mode. For emission $g(t) = g_u(t)$ with [60],

$$g_u(t) = \frac{u^*(t)}{\sqrt{1 - \int_0^t dt' \, |u(t')|^2}} \tag{2.28}$$

and for absorption $g(t) = g_v(t)$ with a (possibly the same as $u(t)$) pulse shape $v(t)$,

$$g_v(t) = \frac{-v^*(t)}{\sqrt{\int_0^t dt' \, |v(t')|^2}}. \tag{2.29}$$

Because the system has been transformed into a collection of interacting cavities, the SLH framework [61] can be used to derive the Hamiltonian H and Lindblad operators L_i that are plugged into the Lindblad master equation

$$\frac{d\rho}{dt} = -i\left[\hat{H}, \rho\right] + \sum_{i=0}\left(\hat{L}_i\rho\hat{L}_i^\dagger - \frac{1}{2}\left\{\hat{L}_i^\dagger\hat{L}_i, \rho\right\}\right). \tag{2.30}$$

The master equation describes how the total system's density matrix ρ evolves in time. In practice, we numerically solve this equation using QuTiP[62] to extract the time dependent occupation of the various modes.

The Hamiltonian is given by

$$\hat{H}(t) = \hat{H}_s(t) + \frac{i}{2}\left(\sqrt{\gamma}g_u^*(t)\hat{a}_u^\dagger\hat{c} + \sqrt{\gamma^*}g_v(t)\hat{c}^\dagger\hat{a}_v + g_u^*(t)g_v(t)\hat{a}_u^\dagger\hat{a}_v - \text{h.c.}\right), \tag{2.31}$$

where h.c. means hermitian conjugate. The Lindblad operator is

$$\hat{L}_0(t) = \sqrt{\gamma}\hat{c} + g_u(t)\hat{a}_u + g_v(t)\hat{a}_v. \tag{2.32}$$

For clarity, note that although there are three terms in this expression, this is a single

Lindblad operator.

SLH theory also provides a systematic way to find the Hamiltonian and Lindblad operators of more complex networks[16].

16. [61] is a useful resource for this task, especially section 5.2 and the appendix.

CHAPTER 3

LOW NOISE MEASUREMENT AND JOSEPHSON PARAMETRIC AMPLIFIERS

This chapter will start in section 3.1 with a brief introduction to experimental setups for superconducting circuits, as well as motivation for why a low noise amplifier might be useful. Then section 3.2 will go over some design criteria for what aspects of an amplifier we would like to have. Section 3.3 will give provide analytic models for gaining intuition for how JPAs work. Finally, 3.4 will discuss one numeric model for simulating flux-pumped JPAs.

3.1 Measuring superconducting qubits

3.1.1 Dispersive measurement

While we could design the sample so that the readout signal directly interacts with the qubit, this type of measurement system would couple the qubit too strongly to the external environment at the qubit's frequency and lead to a short lifetime T_1 for the qubit[1]. Instead, the qubit is weakly coupled to a resonator whose resonant frequency changes depending on the state of the qubit, as represented in Fig 3.1a. The resonator filters signals from the measurement line at the qubit frequency, and so isolates the qubit from decohering noise. Because the qubit frequency is far detuned from the resonator frequency in the dispersive regime of the Jaynes-Cummings Hamiltonian that describes the system (section 2.4.1), this qubit measurement technique is typically called dispersive measurement. See Daniel Sank's thesis [63] for a good historical overview and quantitative analysis of dispersive measurement. To distinguish between the two possible resonant frequencies associated with the qubit g and e states, it is sufficient to send a signal at a single frequency and measure the signal's phase

1. A qubit's decoherence can be modeled with the Bloch-Redfield model, where weakly coupled noise sources cause relaxation processes characterized by a longitudinal relaxation time T_1 and a transverse relaxation time T_2 [15]

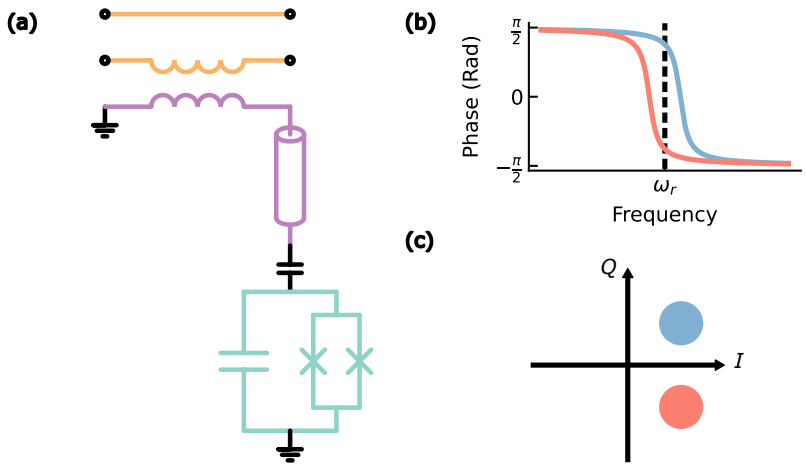

Figure 3.1: **Dispersive measurement of superconducting qubits.** **(a)** We measure our transmon qubits (turquoise) dispersively by coupling them to transmission line resonators (purple) which are coupled to a measurement line (orange). **(b)** A signal transmitted through the measurement line at the resonator frequency ω_r will acquire a different phase depending on if the qubit state is in its excited (red) or ground (blue) state. **(c)** Cartoon showing IQ phase space for the measurement signal with ground and excited states. Each circle represents the Gaussian width for the probability distribution of multiple measurements.

after it interacts with the resonator, as shown in Fig 3.1b.

3.1.2 Signal generation and control

We generate the microwave pulses for our experiments by modulating the envelope of a constant microwave tone from a signal generator using IQ mixers[2]. Single frequency microwave signal generators (also called local oscillators or LO for short) can output signals with well defined frequencies with tuning resolution $\sim$ 1 Hz, tuning ranges over tens of GHz, and variable signal power over tens of dB. These electronics are excellent resources for doing phase sensitive experiments with quantum devices. After passing the signal through low pass filters (See Fig. 3.2a) to remove undesired higher harmonics, an IQ mixer controlled by a Digital-to-Analog Converter (DAC) then modulates the signal's frequency, power and pulse shape. Finally, the signal is connected to the dilution refrigerator (DR) with 50 ohm

2. An alternative method for generating pulses is by using Arbitrary Waveform Generators (AWGs). However, AWGs that can synthesize signals GHz frequencies with sub ns shaping control have only recently [64] become available at a cost that makes sense to use for academic experiments with large numbers of control ports.

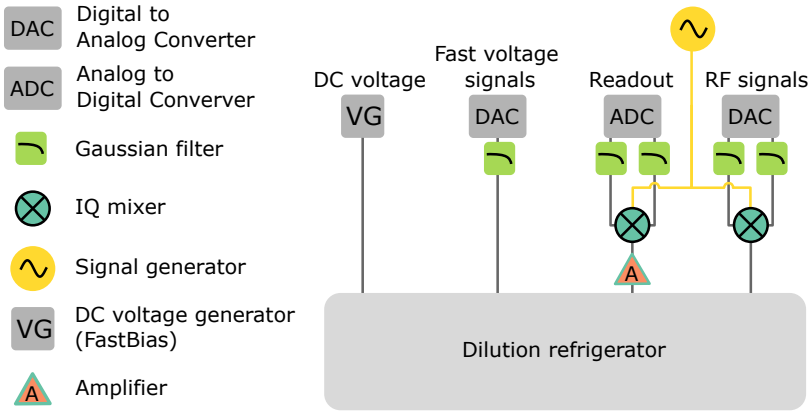

Figure 3.2: **Room temperature electronics.** Example room temperature electronics setup for a superconducting circuit experiment.

cables[3] using SMA connectors that maintain stable phase response when slightly bent as may happen in a lab environment.

With good calibration of these electronics, the pulse timing can be set to ns precision and the frequency can be modulated around ±300 MHz around the LO frequency. For more information on the development and calibration of the electronics in our lab see Youpeng Zhong's thesis [18].

There can easily be tens of individual devices associated with a single experiment that generate signals and acquire data. All devices are connected to a single computer and controlled using software that organizes them so we can synchronously control them. The software we use is called labrad, originally developed by Markus Ansman [65] in the Martinis Group at UC Santa Barbara. On top of labrad, we wrote a library of Python functions for running our experiments [18]. Upgrading this library from Python 2 to Python 3 was an additional significant part of this thesis with contributions from other members in the lab.

3.1.3 Dilution refrigerator setup

Fig. 3.3 shows a measurement line for an example superconducting circuit setup. Three key elements of this setup are that the sample is placed in a cold environment, attenuators reduce

3. Sucotest cables

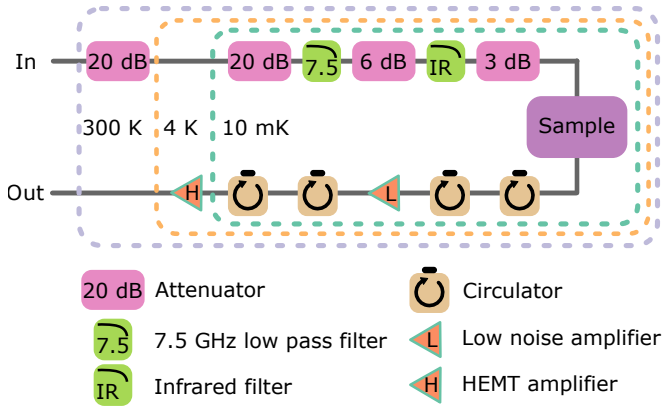

Figure 3.3: **Measurement Line.** Measurement line for an example superconducting circuit setup. Attenuators reduce noise in the signal coming in from the input line while a series of amplifiers amplify the signal going out of the output line.

input signals coming in from room temperature, and amplifiers amplify signals coming out of the sample.

The cold environment is a dilution refrigerator (DR) with base temperature $T_b \approx\sim 10\,\mathrm{mK}$. If we assume a resonator at frequency $\omega_r/2\pi \approx 5\,\mathrm{GHz}$[4] is well thermalized at this temperature, the ground state will be populated with a high probability according to the Boltzmann distribution $\exp(-\hbar\omega_r/k_B T_b) \sim 10^{-11}$. Here $\hbar$ is the reduced Planck constant and k_B is the Boltzmann constant.

Measurement lines carry signals generated at room temperature to the sample. Even if the signal generators produce a small output signal, large thermal fluctuations will affect the sample if not properly attenuated [66]. The thermal noise power $S_V(\omega, T)$ follows the Plank distribution which is proportional to $(\exp(\hbar\omega/k_B T) - 1)^{-1}$. In the high temperature limit (Johnson noise, [67]) this scales linearly and so between the DR's 300 K stage to the $\sim 4\,\mathrm{K}$ stage we can add 20 dB attenuation to proportionally reduce the noise. From 4 K to 10 mK, the noise scales nonlinearly and so requires more attenuation, around 30-40 dB more [63]. These attenuators should be well thermalized to their environment to be effective[5].

4. Superconducting circuits are generally designed with frequencies between $2 - 10\,\mathrm{GHz}$ mainly due to wide availability of microwave electronics in this range

5. There are research efforts to generate signals at colder DR stages to reduce the number of required

Additional elements include low pass filters and infrared filters [69] that reduce high frequency noise from entering the sample from the input line. Purcell filters (See Appendix C) further filter noise at the readout resonator frequency from affecting the qubit).

After interacting with the sample, the measurement lines then carry the signal to be measured outside the DR. The readout resonator will be populated with only a few photons on average which would be overwhelmed by thermal noise if directly sent to the room temperature detectors. So we amplify the signal to improve this signal-to-noise ratio (SNR). Amplification occurs using multiple amplifiers in series located at different temperature stages of the DR. As derived in appendix A.1, if the first amplifier in series has sufficient gain relative to the noise added by the next amplifier, the noise contribution from later stages can be neglected [6]. This useful property provides the motivation for developing better low noise cryogenic amplifiers for use in measuring quantum systems. Later sections will provide more details in how to design and fabricate one type of low noise amplifier, the Josephson Parametric Amplifier (JPA). The second amplifier in the chain is located at the 4 K stage and is a High-Electron-Mobility-Transistor (HEMT) amplifier. To isolate the sample from the noise generated by the HEMT or other sources on the output line, we place multiple circulators on the output of the mixing chamber stage. It should be noted that this noise isolation comes at the cost of some slight attenuation (< 0.4 dB insertion loss for Quinstar QCY series circulators according to the manufacturer) which may reduce the readout fidelity of the sample. We decided not to add additional filters to the output line due to this potential loss of readout fidelity.

3.1.4 Room temperature measurement

Several amplifiers at room temperature further amplify the signal (See Fig. 3.2). An IQ mixer downconverts the signal from GHz frequencies to MHz frequencies, which is subsequently

lines from room temperature and thus the required thermal load on the DR [68]

6. A similar result can be derived without quantum theory [70]

digitized by an Analog-to-Digital Converter (ADC). This IQ mixer has two signal inputs: the signal that went through the cryogenic system and a reference signal split from the LO. This demodulation and digitization of the signal is an implementation of a Heterodyne detection scheme [15].

3.2 Josephson Parametric Amplifier design criteria

Josephson Parametric Amplifiers (JPAs) have found widespread use in the superconducting circuit community because they can amplify microwave signals with low added noise. For a device that is essentially just a capacitor in parallel with a SQUID, JPAs can have surprisingly complex behavior. They are nonlinear resonators, and depending on the mode of operation this nonlinearity can be either beneficial or a detriment to good operation. However the goals in a JPA design are relatively straightforward: lower noise, higher gain, wider bandwidths, and lower saturation power. Each of these goals will be briefly discussed and then sections 3.3 and 3.4 will go over various analytic and numeric models respectively for understanding JPAs in more depth.

3.2.1 Noise

When performing a measurement one would like to add as little noise as possible in order to improve the fidelity of the measurement. To measure a coherent signal we usually amplify the signal with linear amplifiers, i.e. the input power is proportional to the output power. We will also usually be operating the amplifiers in non-degenerate mode, meaning that both signal quadratures are amplified equally, preserving the phase of the input signal. For large gain amplifiers, quantum mechanics places a lower bound on the noise (referred to the input) of a linear non-degenerate amplifier of half the zero-point fluctuations [71]. Referred to the input of the amplifier here means that we take the output signal and divide by the gain. Amplifiers that achieve this lower bound are called quantum-limited amplifiers. While it is

possible to have noiseless amplification of a single quadrature if the device is operated as a degenerate amplifier, this mode of operation will not be the focus of this design effort.

3.2.2 Gain

As derived in Appendix A.1, for amplifiers in series in order to ignore the noise contribution of later amplifiers we need to satisfy $N_1 \gg N_2/G_1$. Here N_1 and N_2 is the noise power (referred to the input) added by the first and second amplifier respectively and G_1 is the power gain for the first amplifier. The noise temperature T_i is a measure of the added noise N_i that is independent of the signal bandwidth B such that $T_i = N_i/k_B B$ where k_B is the Boltzmann constant. For a quantum limited amplifier at 5 GHz, the minimum possible temperature is $hf/k_B = 240\,\text{mK}$. Half of this temperature is due to quantum fluctuations of an input signal to the first amplifier and half is due to minimum required noise added by a non-degenerate amplifier as noted in Sec. 3.2.1. The second amplifier is our amplification chain is a high-electron-mobility transistor (HEMT) amplifier with a noise temperature of $\sim 2\,\text{K}$. If we target a gain of 20 dB for the first amplifier which is quantum-limited then $N_1 \approx 240\,\text{mK} \gg 20\,\text{mK} \approx N_2/G_1$.

Note that this gain target depends on both the noise added by the first amplifier and noise added by later elements in the amplification line. If either noise is different than these assumptions, then the minimum gain required to maximize readout fidelity will also vary.

3.2.3 Bandwidth

When an amplifier's gain is Gaussian shaped in frequency we can define the bandwidth from the points on the curve 3 dB from the peak on either side. For many JPAs made from resonators, as we vary the JPA pump power to increase the gain, the 3 dB bandwidth goes down. For the simplified case of a Duffing nonlinear resonator which can be solved analytically, the product of the amplitude gain and the 3 dB bandwidth equal a constant (See [72] and Sec. 3.3.3). This gain-bandwidth product can be increased by lowering the

coupling quality factor of the resonator, as the bandwidth scales as $1/Q$ [73, 74]. However, the JPA saturation power scales as I_c^2/Q and the JPA junction inductance $L_j \propto 1/I_c$ and so increasing the bandwidth by varying the junction parameters also reduces saturation power [73]. Strategies for increasing the bandwidth of JPAs while still reaching a high gain and saturation power are discussed in section 4.2.1.

The 3 dB bandwidth is the typical definition for an amplifier's bandwidth found in the literature. For amplifiers with more complex amplification curves it can be more useful in practice to define the bandwidth as the frequency range over which the gain is above some set value. We will be using this second definition for the following sections using 20 dB as a reference (See Sec. 3.2.2).

A wide bandwidth at high gain simplifies the tuneup process for a qubit measurement because we can set default parameters for the amplifier and it is likely that the readout resonator for the system will be at a good frequency. Wide bandwidths also allows measurement of multiple qubits simultaneously which lets us measure correlations in the different qubit states and calculate entanglement between them. The maximum number of qubits that can be measured is both a function of the high-gain bandwidth and the saturation power as discussed in Sec. 3.2.4.

3.2.4 Saturation power

Saturation power can be thought of as a limit to how much power we can send into an amplifier due to reduced gain at higher signal powers. One commonly used definition is when the gain deviates from its low power value by 1 dB. For JPAs this occurs primarily because the linear approximation for the Josephson junction's inductance is no longer valid at high signal powers [75]. For multi-qubit measurements each measurement requires additional signal power and so the saturation power sets an upper limit to the number of qubits that can be simultaneously measured.

Another cause of the saturation power limit is when the amplifier depletes a significant

portion of the energy in the pump. Most amplifier models assume negligible pump depletion, this is called the stiff-pump approximation. For JPAs, pump depletion is not a significant issue at the gains needed for quantum measurement however it may cause problems for other types of superconducting amplifiers [76].

3.3 JPA theory and analytic models

There are many groups that have worked on JPAs over the recent decades [77, 78, 79, 52, 80, 81]. Some good reviews and theses on superconducting quantum limited amplifiers include [76, 15, 72, 82, 75, 83, 34]

This section will go over analytic models of JPAs, which are useful for gaining intuition about how parametric amplifiers work. There are limitations to quantitative predictions from analytic models, as they tend to ignore higher-order terms that are important for predicting amplifier performance [84]. Because of these deviations we will rely on numeric models for designing our JPA (See Sec. 3.4) .

3.3.1 Parametric amplifier intuition

A JPA is an example of a parametrically driven system. In other words some parameter of the device is modulated periodically in time to get amplification. A classic example is a playground swing, where if the rider stands or crouches the center of mass will vary in time and transfer energy from the rider to the swing[7] [85]. Another example is a skateboarder on a half-pipe ramp [76]. Note that in both these cases the oscillator is nonlinear, and that it is a modulated system parameter (the rider moving up and down) that is causing the amplified motion rather than an external force pushing on the rider.

For both of these cases the rider modulates their height at twice the frequency of their horizontal motion. Similarly, the pump for a flux-pumped JPA also requires modulating

7. The more typical technique of the rider pumping their legs forwards/backwards is also a parametric drive, but the equations are slightly more complicated than the standing method

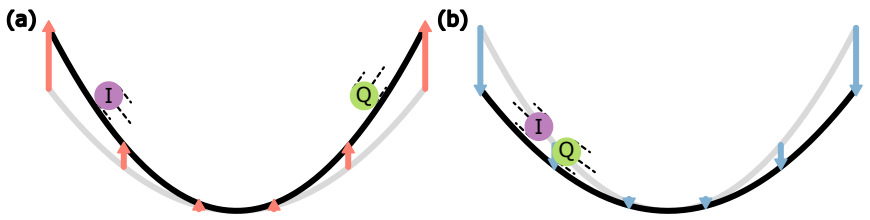

Figure 3.4: **Classical model of three-wave mixing parametric amplification and deamplification.** **(a)** A cosine potential well is modulated with small amplitude compared to the potential height at twice the frequency of a particle oscillating in the potential ($\omega_p = 2\omega_0$). If the particle goes up a slope when the potential rises (particle I, purple), it gains energy. A second particle $\pi/2$ out of phase with the first particle (particle Q, green) will be going down the other slope at the same time, and will lose energy as the potential rises. **(b)** After some time, particle I is going down the slope while the potential goes down, still gaining energy while particle Q loses energy going up that slope.

the flux at twice the signal frequency (Sec. 3.3.2). The following example may give some intuition for why the doubled frequency for the pump is needed.

Fig. 3.4 is an illustration inspired by a similar figure in [82] of classical particles oscillating in a parabolic potential V whose slope is modulated in time with a cosine function . The potential varies in time as $V(x,t) = x^2(1 + \epsilon\cos(\omega_p t))$ where x is the particle's position, $\omega_p = 2\omega_0$ is the pump frequency and $\epsilon \ll 1$. I and Q are two particles that are $\frac{\pi}{2}$ out of phase. Because ω_p is twice the resonance frequency of the potential I is synchronized with the rise and fall of the potential. In Fig. 3.4a, this means that V always does positive work on I because the change in potential and the particle's velocity's vertical component are in the same direction. Similarly, in Fig. 3.4b, V does negative work on Q because the change in potential and the particle's velocity are in opposite directions. We say that I was amplified while Q was deamplified. This is known as phase-sensitive amplification in a parametric amplifier. Choosing a modulation frequency which is slightly different than twice the resonant frequency will result in phase-insensitive (non-degenerate) amplification where both particles are amplified.

3.3.2 Pump modes

A JPA can be designed to operate in one of two modes: three-wave mixing or four-wave mixing, also known as flux pumping or current pumping respectively. In three-wave mixing, a pump mode photon at frequency ω_p is converted to a signal ω_s and idler ω_i photon at approximately half the frequency of the pump so that $\omega_p = \omega_s + \omega_i$. The signal and idler frequencies are close in frequency with $\omega_s \approx \omega_i$. Three-wave mixing amplification is associated with JPAs whose SQUID is driven with an incident magnetic flux modulated near $2\omega_s$ because the JPA resonance frequency is locally odd in flux for non-zero flux bias offset [82]. In four-wave mixing mode, two pump photons are converted to a signal and idler photon with $2\omega_p = \omega_s + \omega_i$. Four-wave mixing amplification is associated with the pump mode near ω_s sent through the signal line to drive the JPA single junction or SQUID with a varying current, because the JPA resonance frequency is locally even with the current amplitude.

Flux pumped JPAs require an additional microwave line to operate compared to current pumped JPAs. While this additional line adds wiring complexity to the flux pumped amplifier, the setup simplifies the measurement of the signal, because the pump mode is separated from the signal both physically and in frequency. For current-pumped amplifiers the pump mode needs to be filtered from the signal, which can be difficult because of their proximity in frequency.

3.3.3 Duffing Oscillator

The simplest nonlinear oscillator model is the duffing oscillator, with an equation of motion given by [72]

$$\ddot{x} + 2\gamma\dot{x} + \omega_0^2 x + \beta x^3 = F\cos(\omega t), \tag{3.1}$$

with a dissipation term γ, resonant frequency ω_0, nonlinearity β, and driving force F. Assuming low dissipation and driving near ω_0 (four-wave mixing, see Sec. 3.3.2), we can get an

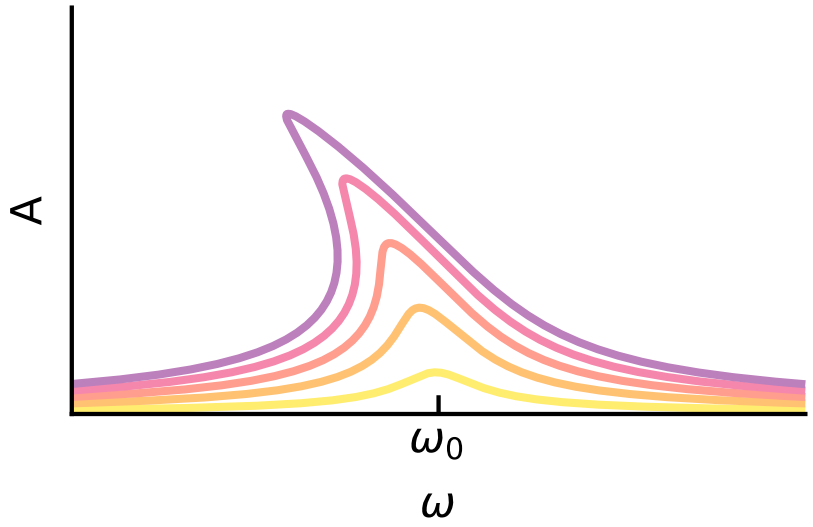

Figure 3.5: **Duffing equation model.** Plot of Eq. 3.2. Darker colors have a larger drive F (yellow to purple)

expression for the response amplitude [72]

$$F^2 = \left([2\omega_0(\omega_0 - \omega) + \frac{3}{4}\beta A^2]^2 + (2\gamma\omega_0)^2 \right) A^2. \tag{3.2}$$

By plotting the implicitly defined A from Eq. 3.2 in Fig. 3.5 (inspired by a similar plot in [83]) we can see several key features of driven nonlinear systems. First, the resonance frequency of the resonator changes as a function of the drive amplitude. In this case a negative β leads to decreasing resonance frequencies at higher drives. Second, above a certain critical drive amplitude, the response amplitude can take on multiple stable values. This is the system's bistable regime. Parametric amplifiers operate at drive amplitudes below and near the bistable regime.

3.3.4 Monochromatic flux pumped JPA

The approximate Hamiltonian $\hat{H}_f$ for a lumped element JPA pumped by a monochromatic flux pump has many variables that have their own expanded definitions, see [84] for more

details. Lumped element here means that the model will include a SQUID in parallel with a lumped-element capacitor. As noted in section 3.3.2, a flux pumped JPA is described by three-wave mixing amplification so that $\omega_p \approx 2\tilde{\omega}_0$

$$\hat{H}_f = \Delta_f \hat{a}^\dagger \hat{a} + \frac{\lambda_f}{2}(\hat{a}^{\dagger 2} + \hat{a}^2) + \hat{H}_{fc}. \tag{3.3}$$

$\hat{H}_f$ is derived in the quartic potential approximation and the rotating wave approximation, both valid for $|\Lambda| \ll \omega_0$ (Eq. 3.6 and 3.8 respectively). Eq. 3.3 here has been organized into 3 parts from left to right: a term with Δ_f related to the oscillator frequency, a term with λ_f related to the oscillator squeezing, and finally $\hat{H}_{fc}$ which has non-quadratic corrections up to quartic order.

Δ_f is the detuning between half the pump frequency ω_p and a renormalized oscillator frequency $\tilde{\omega_0}$. The bare frequency of the resonator ω_0 is calculated using the Josephson energy E_J and the charging energy E_C. E_C is calculated using the single electron charge e and the JPA capacitance C. $\tilde{\omega}_0$ modifies ω_0 by including a nonlinear correction with the Kerr nonlinearity Λ.

$$\Delta_f = \tilde{\omega_0} - \omega_p/2 \tag{3.4}$$

$$\tilde{\omega}_0 = \omega_0 - 2\Lambda \tag{3.5}$$

$$\omega_0 = \sqrt{8E_J E_C} \tag{3.6}$$

$$E_C = \frac{e^2}{2C} \tag{3.7}$$

$$\Lambda = \frac{-E_J \Phi_{\text{ZPF}}^4}{4} = \frac{-E_C}{2}. \tag{3.8}$$

Note that Λ is negative and has a simple relationship with E_C. Λ can also be expressed in terms of E_J and the unitless zero-point flux fluctuations Φ_{ZPF}.

The following two terms of $\hat{H}_f$ are functions of the flux through the SQUID, expressed

by their Fourier coefficients $E_J^{(n)}$. The external flux Φ_{ext} in the SQUID loop is made up of a unitless static (DC) flux F and a modulation amplitude δf (AC), both normalized by the reduced flux quantum φ_0. In the limit of small pump amplitude ($\delta_f \ll 1$), these Fourier coefficients can be approximated as given in Eqs. 3.10-3.12.

$$\frac{\Phi_{\text{ext}}}{2\varphi_0} = F + \delta f \cos \omega_p t \tag{3.9}$$

$$E_J^{(0)} \approx E_J \cos F \tag{3.10}$$

$$E_J^{(1)} \approx -E_J \delta f \sin F \tag{3.11}$$

$$E_J^{(2)} \approx -\frac{1}{4} E_J \delta f^2 \cos F \tag{3.12}$$

$$\varphi_0 = \frac{\hbar}{2e}. \tag{3.13}$$

λ_f is the effective parametric pump strength and is the coefficient to a Hamiltonian form associated with squeezing and amplification. It scales with δ_f and so pumping harder increases the amplification.

$$\lambda_f = \frac{E_J^{(1)} \Phi_{\text{ZPF}}^2}{2} \tag{3.14}$$

$$\Phi_{\text{ZPF}} = 2\sqrt{\frac{E_C}{\omega_0}}. \tag{3.15}$$

However, the non-quadratic corrections in $\hat{H}_{fc}$ limit both squeezing and amplification in amplifiers [84]. One method of improving JPA performance is by minimizing these nonlinearities through either engineering the flux-tunable Josephson element [86] or making SQUID arrays [56, 87].

$$\hat{H}_{fc} = \Lambda_f \hat{a}^{\dagger 2}\hat{a}^2 - \frac{E_J^{(1)}\Phi_{\text{ZPF}}^4}{12}(\hat{a}^\dagger \hat{a}^3 + \hat{a}^{\dagger 3}\hat{a}) - \frac{E_J^{(2)}\Phi_{\text{ZPF}}^4}{48}(\hat{a}^4 + \hat{a}^{\dagger 4}) \tag{3.16}$$

$$\Lambda_f = \frac{-E_J^{(0)}\Phi_{\text{ZPF}}^4}{4} = \Lambda J_0(\delta f)\cos F \tag{3.17}$$

3.4 Numeric model

To numerically simulate the JPA, we will create a linear circuit model of the device. The capacitor will be modeled as a lumped element capacitor. To linearize the SQUID we will use the pumpistor model (see below) for the SQUID in a nondispersive three-wave mixing mode. In this model the SQUID is replaced with linear inductors and a negative resistance. Where a typical (positive) resistor will reduce a signal that reflects onto it, a resistor with a negative resistance will amplify the signal.

This model was formalized into a python package (mostly written by postdocs in the lab Audrey Bienfait and Étienne Dumur). After constructing the desired circuit, the model outputs the amplifier gain and bandwidth over 20 dB as a function of the pump frequency, pump power, and dc flux.

3.4.1 The pumpistor

For a single Josephson junction, Eq. 2.7 shows that the inductance of the junction $L_J(I)$ depends nonlinearly on I. When we apply larger currents to the junction, L_J increases. This makes it difficult to analyze how an AC signal will reflect off of the junction, because the inductance is nominally different at the current maxima than when the current is zero on the oscillating wave. The usual way to deal with an oscillating input signal to a nonlinear system is to assume that the input signal is small so that we can ignore higher order terms in the expansion of the parameter of interest.

A linear approximation of Eq. 2.7 results in the Josephson inductance $L_{j0} = \frac{\Phi_0}{2\pi I_c}$. For

a DC biased SQUID we linearize Eq. 2.11 with respect to the phase difference across the junction δ and get $L_s(\Phi_{\text{ext}}) = \frac{\Phi_0}{4\pi I_c \cos\left(\pi \frac{\Phi_{\text{ext}}}{\Phi_0}\right)}$. Note that we are interested in linearizing the system with respect to oscillating parameters, the inductance may still change nonlinearly with respect to other parameters. For example, although L_s depends nonlinearly on the parameter Φ_{ext}, it does not depend nonlinearly on the input signal. While this will let us model useful parameters such as the gain and bandwidth, it does not model input saturation power for the amplifier.

The pumpistor model [88, 89] is an extension of this linearization idea to a flux-pumped SQUID. For the work in this thesis, we will focus on the three-wave non-degenerate case, but a different pumpistor model can be derived for the three-wave degenerate case or even the four-wave mixing case. This section gives an overview of the derivation in Ref. [89], see the text for more details.

We now have two oscillating parameters, the input signal ω_s and the flux pump $\omega_p \approx 2\omega_s$, and so need to linearize Eq. 2.11 with respect to both δ and the flux through the loop Φ_{ext}. $\Phi_{\text{ext}} = \Phi_{dc} + \delta\Phi$ is composed of both a static DC flux Φ_{dc} and an AC flux $\Phi_{ac}\cos(\omega_p t + \theta_p)$ and can be written in terms of normalized flux amplitudes $F = \pi\frac{\Phi_{dc}}{\Phi_0}$ and $\Delta f = \pi\frac{\Phi_{ac}}{\Phi_0}$. We also need to keep track of the idler mode $\omega_i = \omega_p - \omega_s$ that is present in the system.

The current I_{sq} through the SQUID becomes

$$I_{sq} = 2I_c \cos\left(\pi\frac{\Phi_{\text{ext}}}{\Phi_0}\right)\sin(\delta) \tag{3.18}$$

$$\approx 2I_c\left[\cos(F) - \sin(F)\,\Delta f\cos\left(\omega_p t + \theta_p\right)\right]\left(\sum_{n=s,p,i}\delta_n\right), \tag{3.19}$$

where θ_p is the phase of the pump. Ref. [89] refers to the term containing the cos as the "flux" term and the term containing sum of phases the "phase" term. In the approximation for Eq. 3.19, we assume that the flux pumping of the SQUID is the only effect coupling between the ω_s, ω_p, and ω_i modes. If there is additional stray coupling between the modes in the system, the approximation here might not be valid. This point is important for designing

the geometry of the on-chip flux line and the SQUID ground to avoid stray coupling as a non-negligible contribution to the stray mode will add sine oscillations to the phase term in Eq. 3.19, significantly modifying the mixing between frequencies and potentially reducing the achievable gain in an amplifier using the SQUID.

Following the notation in Ref. [89], we define the current and voltage across the SQUID with I_1, V_1 at frequency ω_s and I_2, V_2 at frequency ω_i. By integrating the Josephson voltage relation Eq. 2.10 and substituting into Eq. 3.19, we find relations between the SQUID currents and voltages at the two frequencies of interest

$$\begin{pmatrix} I_1 \\ I_2^* \end{pmatrix} = \frac{1}{iL_J} \begin{pmatrix} \frac{\epsilon_0}{\omega_s} & \frac{-\epsilon_1^*}{\omega_i} \\ \frac{\epsilon_1}{\omega_s} & \frac{-\epsilon_0}{\omega_i} \end{pmatrix} \begin{pmatrix} V_1 \\ V_2^* \end{pmatrix}, \tag{3.20}$$

where $\epsilon_0 = 1 - \frac{1}{4}\Delta f^2$ and $\epsilon_1 = \frac{\Delta f}{2}\tan(F)e^{-i\theta_p}$.

The goal is to find the impedance of the SQUID at signal frequency $Z_{SQ} = \frac{V_1}{I_1}$. At this point in the calculation we do not have enough constraints to uniquely determine this quantity. The remaining constraints are resolved by placing the SQUID as a load in a circuit whose impedance as seen from the SQUID is a function of frequency. The result is

$$Z_{SQ} = \frac{1}{L_{n,0}} + \frac{1}{L_{n,2}}, \tag{3.21}$$

$$L_{n,0} = L_J/\epsilon_0, \tag{3.22}$$

$$L_{n,2} = -\frac{L_J}{|\epsilon_1|^2}\left(\epsilon_0 - j\omega_i L_J Y_i^*\right), \tag{3.23}$$

where Y_i is the external admittance seen by the SQUID at the idler frequency ω_i. Z_{SQ} can be visually represented as a circuit with three elements as seen in Fig. 3.6. For small pump powers, $L_{n,0}$ is the Josephson inductance. $\mathrm{Im}[L_{n,2}]$ is an inductor whose inductance depends on the pump power. Finally, $\mathrm{Re}[L_{n,2}]$ is a resistor with negative resistance whose gain depends on the pump power and is the "pumpistor" that was introduced above.

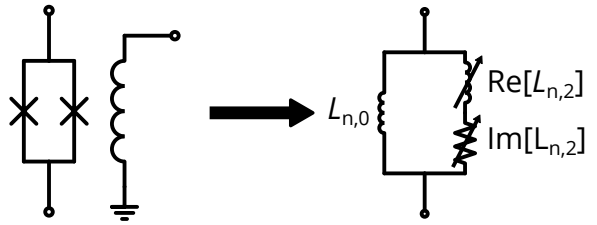

Figure 3.6: **Pumpistor linear circuit model.** A parametrically pumped SQUID with $\omega_p \approx 2\omega_s$ can be modeled as a combination of linear circuit elements including inductors $L_{n,0}$, Re$[L_{n,2}]$ and a negative resistor Im$[L_{n,2}]$, which can model gain. Definitions for these linearized circuit components are defined in Eqs. 3.22 and 3.23

3.4.2 Environmental admittance

As mentioned in the previous section, the JPA's gain depends on the external admittance seen from the JPA. All environment impedances, including the impedance transformer, are implemented in the numerical model as ABCD matrices [27]. ABCD matrices, defined for two-port networks, contain the same information as impedance, admittance, and scattering matrices . They have the useful property that the ABCD matrix of two cascaded networks is the matrix multiplication of the individual networks. An ABCD matrix is a 2×2 matrix with the form

$$ABCD = \begin{pmatrix} A & B \\ C & D \end{pmatrix}. \tag{3.24}$$

Two ABCD matrices that will be useful here include the matrix for a series impedance Z and for a lossless transmission line of length l with characteristic impedance Z_0, characteristic admittance $Y_0 = 1/Z_0$ and propagation constant β

$$ABCD_Z = \begin{pmatrix} 1 & Z \\ 0 & 1 \end{pmatrix} \tag{3.25}$$

$$ABCD_{\text{tline}} = \begin{pmatrix} \cos\beta l & iZ_0 \sin\beta l \\ iY_0 \sin\beta l & \cos\beta l \end{pmatrix}. \tag{3.26}$$

For a few examples, we can model wirebond inductance L_w using $Z = i\omega L_w$, circulator resistance R_c with $Z = R_c$, and impedance transforming transmission line segments using the corresponding matrices.

We find the external ABCD matrix by multiplying the ABCD matrices of all the external impedances together and then terminating with a $50\,\Omega$ resistor[8]. The environmental admittance seen by the SQUID at the idler frequency Y_i can then be calculated using the expression for S_{11} in terms of the ABCD matrix parameters in a transmission line with characteristic impedance Z_0 is given by [27] (Table 4.2)

$$S_{11} = \frac{A + B/Z_0 - CZ_0 - D}{A + B/Z_0 + CZ_0 + D} \tag{3.27}$$

$$Z_i = \frac{Z_0(1 + S_{11})}{1 - S_{11}} = \frac{AZ_0 + B}{CZ_0 + D} \tag{3.28}$$

$$Y_i = 1/Z_i = \frac{CZ_0 + D}{AZ_0 + B}, \tag{3.29}$$

where Eq. 3.28 is the relationship between a load impedance and reflection coefficient in a transmission line with characteristic impedance Z_0.

8. A $50\,\Omega$ resistor to ground will look the same as an infinite line with characteristic impedance $Z_0 = 50\,\Omega$

CHAPTER 4

FLUX-PUMPED IMPEDANCE-ENGINEERED BROADBAND JOSEPHSON PARAMETRIC AMPLIFIER

As more universities pursue research in quantum science and engineering, it would be useful for researchers to have access to low cost, high performance quantum limited amplifiers. JPAs that work at microwave frequencies and can reach quantum limited performance with high gain and are relatively straightforward to fabricate. However, single cavity JPAs have a finite gain-bandwidth product that limits the achievable bandwidth at high gain. Section 4.1 with discuss the design and characterization of a JPA without impedance engineering, which has this bandwidth limitation. Then, section 4.2 will go over design and characterization of a JPA with an impedance transformer, showing an improved bandwidth. Fabrication information for both designs are found in Appendix B.1.

4.1 JPA without impedance engineering

4.1.1 Simulating parameters

A JPA has a number of parameters associated with a given device: the operating frequency f, the lumped element capacitance C, the SQUID critical current I_c, the DC loop flux Φ_{DC} during operation and the AC pump flux amplitude Φ_{AC} during operation. While deciding on which values these parameters will take we keep in mind the considerations described in section 3.2: noise, gain, bandwidth, and saturation power. There is no single way to optimize the design of an amplifier, depending on the application these considerations may have different ranking in importance and will require different parameters to achieve a different design. For the purposes of measuring qubits, we will be aiming for a gain of around 20 dB for as large a bandwidth as possible while trying to reduce nonlinearity due to increased SQUID pump power.

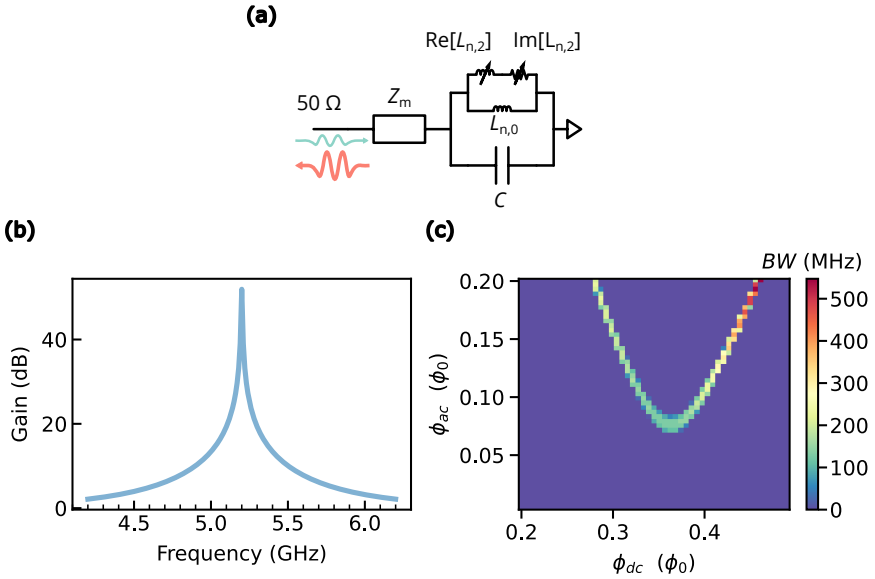

Figure 4.1: **Simulating JPA gain (a)**Circuit model for a JPA coupled to an arbitrary environment. **(b)**The JPA with no impedance matching can show a bandwidth over 100 MHz for gain > 20 dB. **(c)** Plotting the bandwidth for the JPA shows a characteristic parabolic curve when plotted as a function of DC bias ϕ_{dc} and amplifier pump power ϕ_{ac}

Fig. 4.1a shows the circuit for a JPA used for simulation. Z_m is an impedance that can be replaced with additional circuit elements such as wirebonds, circulators, cables, or an impedance matcher. For the simulations shown here we do not add these additional environmental impedances for simplicity, apart from the impedance matcher in section 4.2.3. For some given circuit parameters we can find the gain of the circuit for different input signal frequencies. An example curve for a simple JPA with just a capacitor and pumpistor ($Z_m = 0$)is shown in Fig. 4.1b. We can plot the bandwidth above 20 dB as a function of the dc flux through the SQUID and the ac pump flux amplitude shown in Fig. 4.1c. The parabolic shape seen here is typical for these plots. For ϕ_{ac} and ϕ_{dc} off the parabola, there is still amplification however it is below 20 dB.

Up to now we have only varied flux and signal parameters for a single device. To compare between devices with different critical currents and capacitances we can choose a single number to characterize the performance of a device. One way to do this is to optimize the operating point for a given device and then compare between devices at these operating

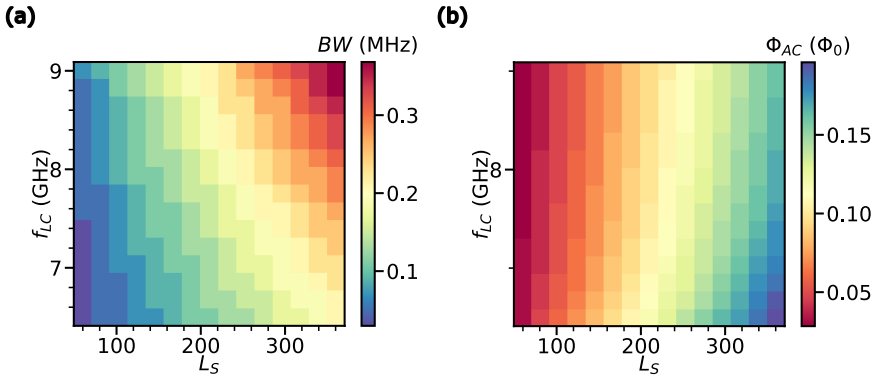

Figure 4.2: **JPA performance and junction inductance.** **(a)**For a JPA designed at a given bare resonance frequency, the bandwidth tends to increase with higher SQUID inductance L_s **(b)** The required pump power decreases with higher L_s. Choosing L_s is a trade off between these parameters.

points. We would like to operate our device at the smallest Φ_{AC} that has good bandwidths, and so we can choose the bottom of the parabola for this reference point. A smaller Φ_{AC} is desirable because higher pump powers mean the JPA is operating with higher nonlinearity and as a consequence will have lower saturation powers.

Fig. 4.2 shows how the features of this operating point varies with the JPA bare resonance frequency and SQUID bare inductance L_{s0}. Here the bare resonance frequency and SQUID bare inductance mean what the JPA frequency and SQUID inductance L_s would be at zero applied DC flux. For a given resonance frequency, increasing L_{s0} increases the bandwidth above 20 dB. However increasing L_{s0} also increases the pump amplitude at the operating point. After choosing an operating frequency, we choose L_{s0} that balances these two effects. For the device presented here we decided to limit Φ_{AC} to a reasonably low value of $0.1\Phi_0$.

Another relevant parameter we would have liked to simulate with a numeric model is saturation power, which would then let us choose some minimum acceptable value. However, this would require a non-trivial modification of the numerical approximation in section 3.4 to include nonlinear mixing as a function of the phase difference δ. Eq. 3.19 assumes linearity for that term, and so saturation power due to the input signal can not be estimated.

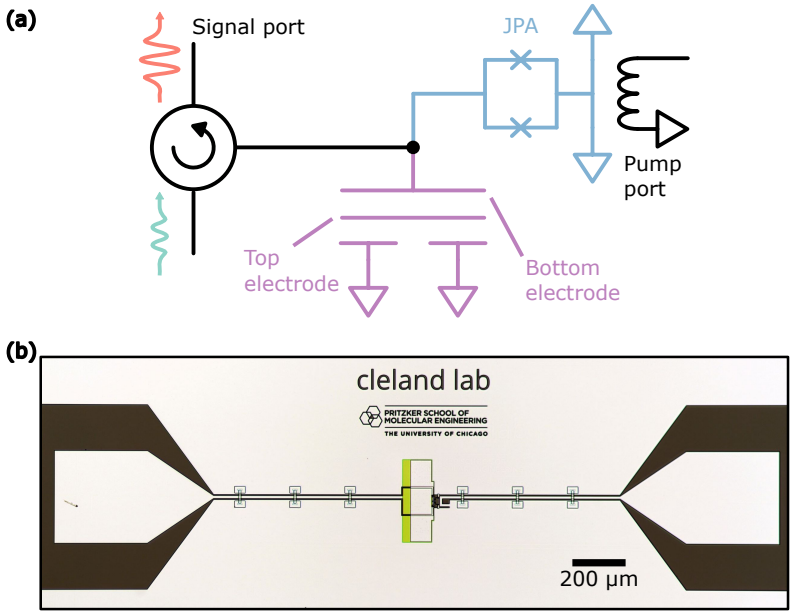

Figure 4.3: **JPA circuit and device.** The JPA operates in reflection, using a circulator to send the reflected and amplified signal to the output line. The signal line is directly connected to the SQUID. The JPA capacitor is composed of a capacitance from the signal line to the top plate and two parallel capacitances to ground.

4.1.2 Device design

Here we will describe the device's physical design. As typically happens with such devices, most of these designs evolved over multiple iterations to correct various issues that arose. The final design will be described here and a more complete fabrication procedure including many of these issues and solutions is described in detail in Appendix B.1.

Similar to Ref. [90], our device has a parallel plate capacitor, a SQUID loop with on-chip flux line, and a galvanic connection to the input as shown in Fig. 4.3a. As mentioned in section 2.2.3, parallel plate capacitors are more space efficient and better at confining electric fields than an equivalent in-plane capacitance. Instead of including a potentially lossy via as in Ref. [90] to connect the top plane of the capacitor to ground we instead add additional two capacitors to ground (this idea was suggested by R. Vijay). For our device's simplified case where the three plate capacitances are equal to C_p the total JPA capacitance $C_T = \left(1/2C_p + 1/C_p\right)^{-1} = \frac{2C_p}{3}$. Note that this results in a floating top capacitor pad.

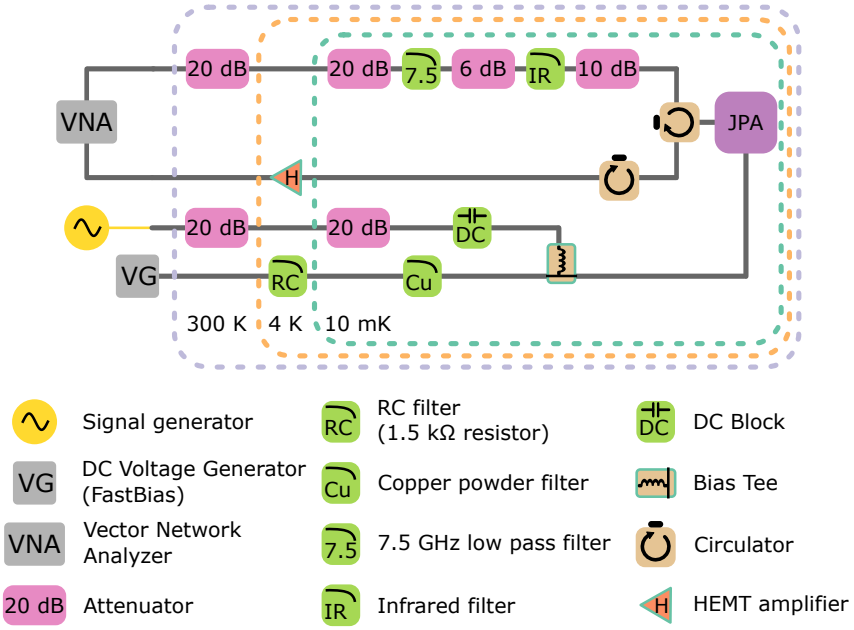

Figure 4.4: **JPA wiring diagram** A wiring diagram for measuring the output from a JPA operating in reflection.

As noted in section 3.4, when coupling the flux line to the SQUID for flux pumping our models assume that we couple to the SQUID's circular mode rather than the other parallel mode. To fix this issue we designed the SQUID connection to reduce the stray mode coupling. Simulating the design with SONNET we find mutual coupling around 20 times the stray coupling at 10 GHz.

A galvanic connection to the input reduces the coupling quality factor of the JPA, increasing the bandwidth.

4.1.3 Wiring

A wiring diagram of the amplifier test is shown in Fig. 4.4. A VNA generates signals and measures the amplified signal, while a separate signal generator provides the pump. The JPA is flux tuned with a DC voltage generator at room temperature, which is converted to a current source by a 1.5 kΩ resistor at 4 K. A bias tee combines the pump and DC current which is sent to the JPA's on-chip flux line.

4.1.4 Operation

After cooling down the device, we connect a VNA to the DR and vary the DC bias on the JPA with the pump off. If the device is working we should see the frequency vary with the bias as in Fig. 4.5a. If the DR was cooled down with no magnetic fields inside, the maxima at zero applied DC bias. If there's some magnetic field left inside, when the superconductor goes below the superconducting temperature it traps the magnetic field and shifts the symmetry point.

Next, we do a quick rough scan of the JPA gain as a function of the DC Bias and pump power. First, we take a scan of the background with a low number of points, a few hundred points over around 600 MHz at 500 Hz bandwidth for example. We set a pump frequency and turn the pump on, and then vary the DC bias and pump power while collecting the same range at a larger bandwidth, such as 5 kHz. After extracting the gain bandwidth over some reference value of interest, such as 20 dB, we get a plot similar to 4.1b, as shown in the experimental data in Fig. 4.5b. We can then do a finer scan around the dip minima to find a set of parameters that are reasonable for the given experiment.

4.1.5 Noise temperature

A number of calibration references can be used for measuring the added noise by an amplifier. The Y-factor measurement [27, 91] compares the output signal of an amplification chain when noise generated by two resistors thermalized to two different known temperatures is passed into the input of an amplifier. This method requires the use of a microwave switch to change the input line going into the amplifier.

Alternatively, a qubit that is dispersively coupled to a readout resonator can be used to measure the number of photons in the resonator generated by an incoming signal[92]. By connecting the qubit at the input of the amplifier and then measuring the signal amplitude at the output of the amplification chain, it is possible to calculate the total gain of the chain. Dividing the output noise of the chain by this gain will give the effective noise of the chain

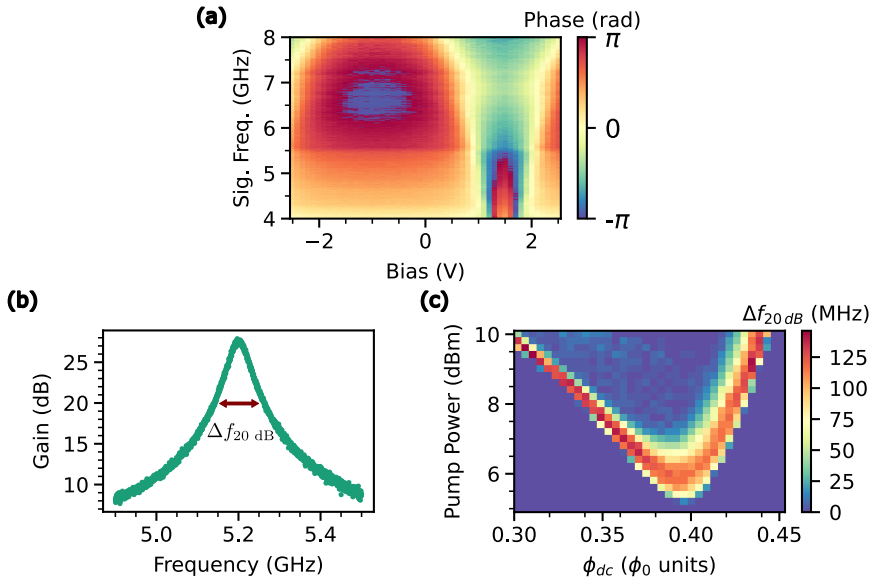

Figure 4.5: **Simple JPA measurement (a)**Reflection measurement of JPA without pumping. **(b)**Simple JPA gain curve showing a gain bandwidth $> 20\,\text{dB} \approx 120\,\text{MHz}$.**(c)** Plotting the bandwidth vs. bias and pump power gives a parabolic shape qualitatively similar to simulation.The device measured here has a design capacitance $C = 1.41\,\text{pF}$ and $I_0 = 1.8\,\mu\text{A}$.

referenced to the input of the first amplifier. As noted in Appendix A.1, for typical amplifier setups this noise tends to be dominated by the first amplifier.

In this thesis, we use the HEMT amplifier in our amplification chain as a reference for measuring the JPA noise. This is a useful technique because we do not need extra devices or input lines apart from those needed to operate the JPA. However, it should be emphasized that this is a rough estimate because the attenuation between the JPA and the HEMT amplifier is not known precisely and has a significant impact on the final result. We also do not have a precise value for the gain of the HEMT amplifier.

The JPA noise temperature can be estimated as (See Appendix A.2 for derivation)

$$T_{\text{JPA}} \approx T_A \left(\frac{1}{G_{\text{JPA}}} - \frac{1}{r} - \frac{1}{AG_{\text{JPA}}} + \frac{1}{Ar} \right) + T_H \left(\frac{1}{Ar} - \frac{1}{AG_{\text{JPA}}} \right), \tag{4.1}$$

where G_{JPA} is the JPA power gain, T_H is the noise temperature of the HEMT amplifier, A and T_A is the attenuation and physical temperature of an attenuator between the JPA and the HEMT amplifiers, $r = \frac{\text{SNR}_{\text{on}}}{\text{SNR}_{\text{off}}}$ where SNR_{on} and SNR_{off} are the signal to noise ratio

measured at room temperature with the JPA on/off respectively.

4.1.6 Estimating attenuation

Next we calculate the estimated attenuation along the line. The line elements between the JPA and the HEMT that may contribute attenuation include two circulators, coaxial cables, and connectors between elements. The circulators[1] have a specified insertion loss better than 0.4 dB each. The output line above the mixing chamber is made up of NbTi-NbTi lines. These lines have an attenuation of approximately 0.015 dB/m at cryogenic temperatures [93]. Below the mixing chamber, we have a 6" EZ flex non-magnetic cable and a 12" Crystek microwave cable. The Crystek microwave datasheet [94] says that the attenuation at 4 GHz is 0.46 dB/ft and 0.7 dB/ft at 8 GHz. As we are operating at around 5.3 GHz this comes out to an attenuation of 0.54 dB. The Ez flex datasheet [95] gives an attenuation of 45.8 dB/100 Ft which comes out to 0.23 dB for 6". Finally, there are around 10 connections between elements between the JPA and the HEMT, and we can conservatively add 0.1 dB attenuation for each connection

Adding together all the elements we have an estimated 2.6 dB of attenuation. This is a rough estimation and could be off by quite a lot in either direction.

4.2 Impedance engineered JPA

4.2.1 Quantum limited amplifiers with large bandwidths

Traveling Wave Parametric Amplifiers (TWPAs) overcome the gain-bandwidth limit by generating amplification using constructive interference in a nonlinear device without a cavity[96]. Quantum-limited TWPAs can be made using thousands of Josephson junctions along a transmission line [92]. While some effort has been made to reduce the complexity of these devices [97], the large number of junctions makes targeting specific device parameters

1. Quinstar QCY series

more difficult than JPAs. Additionally, fabrication yield for working devices tends to go down with increasing numbers of junctions.

Another method of increasing the bandwidth of JPAs is to add an impedance transformer at the input. One type of transformer matches the impedance of the input line to that of the JPA [73, 87]. Impedance matching the input increases the amplifier bandwidth while maintaining a high saturation power. Furthermore, impedance matching transformers improve the gain bandwidth even if the center frequency of the JPA is tuned, increasing their operational range. These transformers can be difficult to make because they require varying the impedance of a transmission line over a wide range, which can be tricky to accomplish with a CPW line. In Ref. [73] the spacing of crossovers on the line was varied, gradually transforming the line from a CPW line to a microstrip line [27] which has a lower impedance. This method can be difficult to fabricate due to the challenges of making closely spaced crossovers.

4.2.2 Imaginary impedance slope engineering

A simpler impedance transformer was demonstrated for a JPA operating in current pumping mode[98], using an off chip transformer with only a $\lambda/4$ resonator and a $\lambda/2$ resonator in series. Although this technique only improves the bandwidth when pumping the JPA at a single frequency, fabricating an on chip version of [98] is potentially more straightforward than the impedance matching transformer in Ref. [73]. The rest of this chapter will discuss our efforts at designing and fabricating a version of this transformer that is integrated on chip with a simple JPA design [90]. Additionally, we will design the amplifier to operate in flux-pumped mode, which can simplify measurements compared to current-pumping by separating the pump from the signal both physically and in frequency (See Sec. 3.3.2).

The transformer is a $\lambda/2$ transmission line resonator placed at the input of the JPA. If we model the resonator as a series LC lumped element resonator, the input impedance as

seen by the JPA is given by [98]

$$Z_{\text{in}}(\Delta\omega) = R + i\alpha\Delta\omega, \tag{4.2}$$

where R is the environmental impedance and $\alpha = 2Z_{\text{aux}}/\Omega_{\text{aux}}$ is the slope of the transformer (auxiliary) resonator's imaginary component as a function of the signal frequency $\Delta\omega$ away from the JPA resonance. Z_{aux} and Ω_{aux} are the auxiliary resonator's impedance and resonant frequency respectively. This linear slope is used to cancel the linear dependence of the JPA's reflection amplitude on the imaginary component of the environmental impedance for small $\Delta\omega$. For small $\Delta\omega$, the real component of the environment impedance is approximately constant, and so engineering just the imaginary component has a significant effect on improving the gain/bandwidth product.

For typical JPAs, the bandwidth falls off as the square-root of the power gain. For the current-pumped case, Ref. [98] shows that after choosing an optimal impedance for Z_{aux}, the bandwidth of the JPA and auxiliary resonator combination instead falls off with the $\frac{1}{4}$th power of the power gain. Specifically, the leading order dependence is canceled by choosing $Z_{\text{aux}} = \eta\frac{R^2}{Z_p}$ where η is a prefactor close to 1 and Z_p is the JPA impedance. While they did not extend this analysis to the flux-pumped case, similar arguments should reach similar conclusions for that mode of operation, as the linearized model for a flux-pumped SQUID also depends on the environmental impedance (section 3.4). Ref. [98] also adds a $\lambda/4$ resonator before the $\lambda/2$ resonator to reduce the environmental impedance from R to $Z^2_{\lambda/4}/R$. This improves the JPA bandwidth by better impedance matching the JPA to the environment.

A theoretical framework which was recently published after the work in this chapter was done analyzes the impedance engineered design from Ref. [98] using a more general model that includes coupled-mode theory and filter synthesis [99]. While this framework will not be reviewed here, it is notable for its future potential to design innovative parametrically coupled circuits.

In the following sections and in Ref. [100], we numerically simulate such a flux-pumped amplifier to find optimal parameters for wide-bandwidth gain using the impedance transformer. We then fabricate a device demonstrating wide bandwidth and low noise.

4.2.3 Simulation and design

In Ref. [98], the impedance transformer is optimally chosen depending on the JPA parameters. We found that many impedance transformer designs were difficult to fabricate given certain JPA parameters, and so first chose an impedance transformer with similar parameters to [98], and then varied JPA parameters to maximize bandwidth. The $\lambda/4$ resonator is centered at 5.3 GHz with a characteristic impedance of 45 Ω. The $\lambda/2$ resonator is also centered at 5.3 GHz with a characteristic impedance of 80 Ω.

After using ABCD matrices to calculate the environmental admittance seen by the JPA SQUID as a function of frequency (See section 3.4.2) we can simulate the gain numerically. Fig. 4.6a and b shows how the amplification bandwidth and optimal pump power vary as a function of device parameters. For similar DC SQUID inductance values, JPA with the impedance transformer has wider bandwidths than without the transformer.

We choose parameters that optimize the bandwidth while staying below $0.1\Phi_0$ pump power Φ_{AC}. In Fig. 4.6c, the simulated gain for the black point in a is plotted, showing the improved bandwidth compared to the JPA without the transformer. Fig. 4.6d and e show how the simulated gain varies as a function of Φ_{AC} and Φ_{DC}], with the frequency of peaks moving around. These multiple peaks are also seen in Ref. [98] when detuning away from the optimal parameters.

The fabricated device with lumped element circuit representation and a zoom in on the flux coupled SQUID is shown in Fig. 4.7. The device has a $\lambda/4$ transformer with impedance $Z_{\lambda/4} = 45\,\Omega$ in series with a $\lambda/2$ transformer with impedance $Z_{\lambda/2} = 80\,\Omega$. The via-free parallel plate capacitor has total capacitance $C = 2.03$ pF.

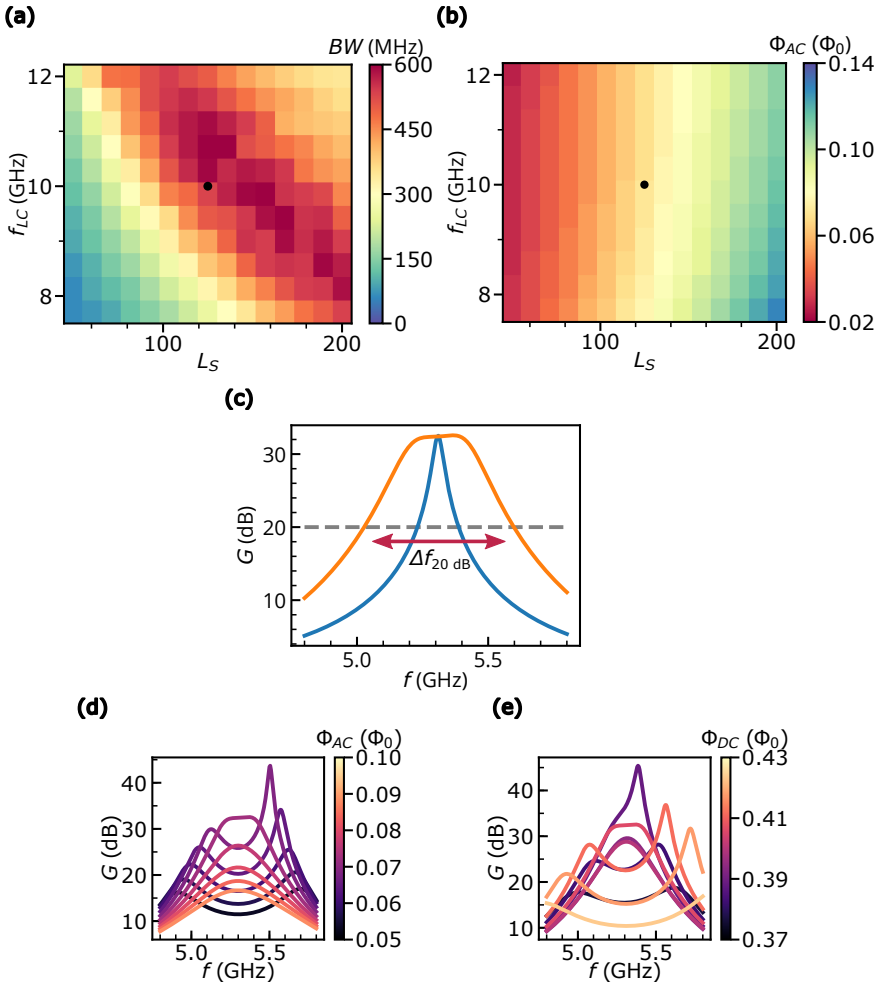

Figure 4.6: **Impedance engineered JPA simulation(a)** Bandwidth $\Delta f_{20\mathrm{dB}}$ and **(d)** Φ_{AC} calculated for the optimized operating point as a function of the bare SQUID inductance L_s and bare LC resonance frequency $f_{LC} = 1/(2\pi\sqrt{L_S C})$. Black dots show design parameters for the fabricated device, where $L_s = 125\,\mathrm{pH}$ and $f_{LC} = 10\,\mathrm{GHz}$. We simulate the JPA using the linearized circuit shown in Fig. 4.1 with impedance-matching element Z_m, JPA capacitance $C = 2.03\,\mathrm{pF}$, SQUID static inductance $L_{\mathrm{n},0}$, SQUID variable inductance $\mathrm{Re}[L_{\mathrm{n},2}]$ and variable resistance (imaginary inductance) $\mathrm{Im}[L_{\mathrm{n},2}]$. The variable circuit elements are functions of the pump amplitude Φ_{AC} and the DC flux Φ_{DC}, plotted in units of the flux quantum $\Phi_0 = h/2e$ in panels b,d, and e. **(c)** Simulated power gain curve $G(f)$ as a function of signal frequency f for a JPA circuit with (orange) and without (blue) the impedance-matching element Z_m. Red arrows indicate the bandwidth $\Delta f_{20\mathrm{dB}}$ for which the power gain is greater than 20 dB.**(d)** Simulated gain curves with $L_s = 125\,\mathrm{pH}$ and $f_{LC} = 10\,\mathrm{GHz}$, for different Φ_{AC} and **(e)** Φ_{DC}, near the operating point where $\Phi_{\mathrm{DC}} = 0.41\,\Phi_0$, and $\Phi_{\mathrm{AC}} = 0.073\,\Phi_0$.

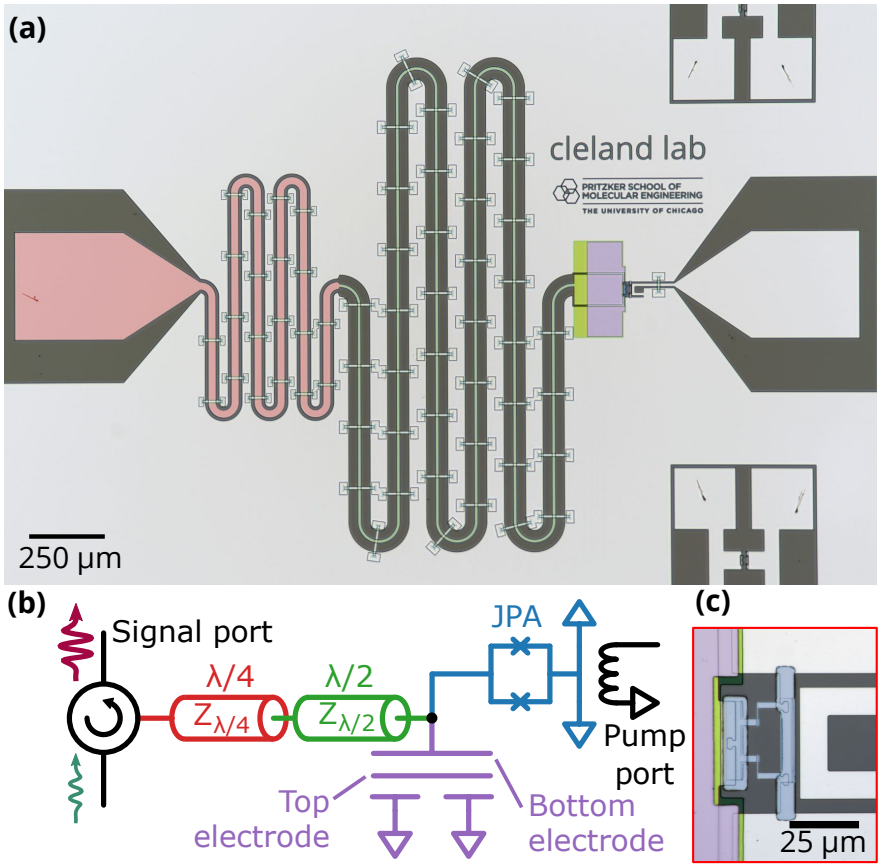

Figure 4.7: **Impedance engineered JPA micrograph and circuit(a)** (a) Micrograph of the fabricated device with a series $\lambda/4$ transformer with impedance $Z_{\lambda/4} = 45\,\Omega$ (red), a $\lambda/2$ transformer with impedance $Z_{\lambda/2} = 80\,\Omega$ (green), and a via-free parallel plate capacitor (purple). **(b)** Circuit representation of the device. **(c)** Higher-magnification micrograph of the JPA SQUID (blue) and its associated flux line.

4.2.4 Operation

After cooling down the JPA, we can see that the reflected signal without pumping as seen in Fig. 4.8a has extra resonances compared to the JPA without the impedance transformer. This resonances are well explained by a linear circuit model of the device without pumping (i.e. with the SQUID replaced by a linear inductor). Varying the pump power at room temperature in Fig. 4.8b, we see the gain for the amplifier varies as expected around the operating point ($\Phi_{\mathrm{DC}} = 0.47\,\Phi_0$) which minimizes noise while maximizing the bandwidth above 20 dB. Although the amplifier does appear to work well, this operating point is at a much higher Φ_{DC} than intended, which means we expect the amplifier to behave more nonlinearly than we would like and is in a regime where a linearized simulation should not apply. The deviation here is possibly due to not simulating the capacitive loading effect of crossovers on the impedance transformer, which would shift the operating parameters away from designed values. In Fig. 4.8d we measure the noise of the amplifier following the method in section 4.1.5. We find a noise temperature that is consistent with near-quantum limited operation, however our characterization technique is too rough to confirm we are at the quantum limit.

At the operating point we find a bandwidth over 20 dB of 300 MHz, roughly consistent with the improvements expected from simulation. A -1 dB saturation power of -116 dBm is similar to other lumped element amplifiers[90], which is good considering we did not explicitly optimize for that value.

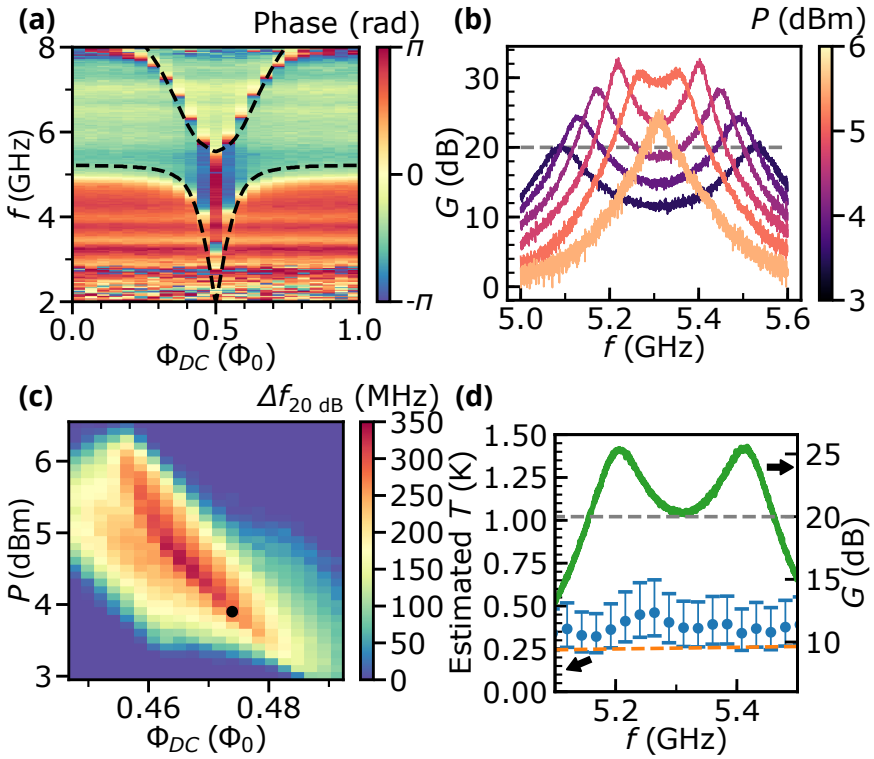

Figure 4.8: **Measuring impedance-engineered JPA in a DR(a)** Phase of small signal reflected from amplifier as a function of frequency f and DC flux Φ_{DC}. Dashed lines are indicate resonances in a linear circuit model of the device without flux pumping. **(b)** Power gain $G(f)$ as a function of frequency for various signal generator powers P at $\Phi_{\mathrm{DC}} = 0.47\,\Phi_0$. **(c)** Bandwidth $\Delta f_{20\mathrm{dB}}$ as a function of pump power P and DC flux Φ_{DC}. **(d)** Measured gain $G(f)$ (green) and estimated noise temperature (blue) versus frequency f at labeled point in panel c, displaying 300 MHz bandwidth. The noise quantum limit (orange) is given by $T_N = hf/k_b$. Noise temperature error bars are dominated by uncertainty in effective HEMT noise temperature.

CHAPTER 5

MULTI-PHOTON COMMUNICATION TESTBED

Quantum communication involves sending a quantum state from one location to another remote location with as high fidelity as possible [11]. One simple example for why this may be useful is the no-cloning theorem, which states that an arbitrary quantum state cannot be duplicated, otherwise it would break some fundamental assumptions of quantum mechanics. This property of quantum states can be used for example in quantum key cryptography where information can be securely shared between two locations [13].

Another use case is building a quantum network between remote quantum computers, enabling the sharing of quantum resources to perform more complex computations [14]. This use case illustrates the fundamental requirements of a quantum communication channel. First the quantum state must be created at the first node. Then the state is released into a waveguide transporting it to the second node. Finally the state is captured at the second node.

In order to maintain the fidelity of the quantum state over the long distances we would prefer to use photons at optical frequencies as their high energies $hf \sim 10^{-19}$ J relative to the thermal energy at room temperature $k_B T \sim 10^{-21}$ J so that $hf \gg k_B T$, mean that they decohere less than photons at microwave frequencies. Fiber optic cables have low loss, with attenuation around 0.16 dB per km at 1550 nm [101]. However, even this low loss rate becomes significant for long range communication. In addition to waveguide loss, it is currently difficult at optical frequencies to deterministically release photons with high fidelity into a waveguide and similarly difficult to capture them with high fidelity [102]. This is not a fundamental limitation to high fidelity state transfer, as it is possible to both herald photons to detect successful transfer and also build a network of quantum repeaters and memories to first establish entanglement between intermediate nodes and then teleport states between them [103, 104]. However these inefficiencies significantly reduce the rate of information transfer: a recent experiment in quantum key distribution had a success probability of 10^{-10}

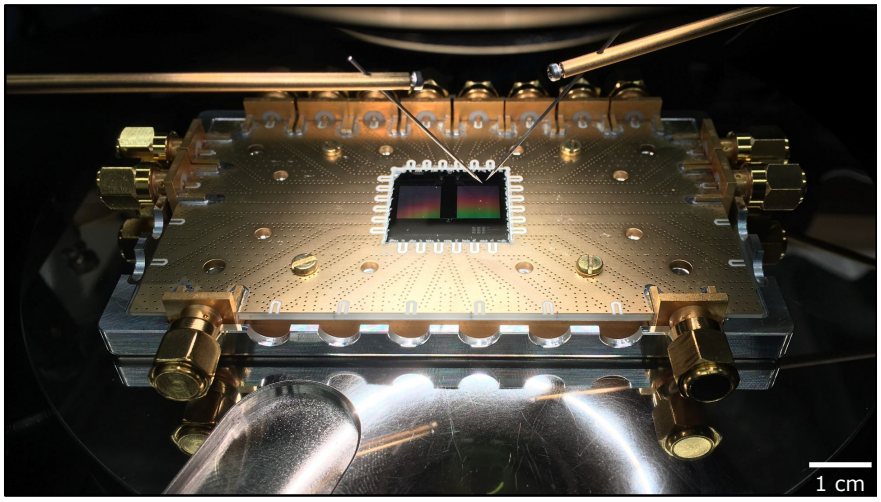

Figure 5.1: **Communication experiment chip** A picture of the communication experiment chip that will be introduced in this chapter. The chip is wire bonded to a PCB holder placed on the lower half of an Al box package. Below the Al box is a DC probe station we use for measuring Josephson junction resistances, two of these probes are shown above the sample.

per key. Furthermore, practical quantum memories for communication networks are still an active area of research [105]. Other preliminary testbeds for these optical networks are being developed [12, 106, 107, 108]. So although optical photons are likely to be the technology of the future, it would be useful for theorists and experimentalists to test out various protocols for quantum communication today with flexible high fidelity testbeds.

The microwave regime has photon energies $hf \sim 10^{-24}$ J, a value much lower than room temperature. There are also many thermal microwave photons at room temperature and significantly more loss because there are currently no known superconductors at room temperature. While it is possible to cool waveguides to mK temperatures, it's not practical to do so for long distances. So long distance quantum communication with superconducting circuits (which operate at microwave frequencies) will likely not be achievable. However, superconducting circuits do have the advantage that they have a large collection of components with controllable parameters that we can build today. And so they are ideal for creating testbeds for communication protocols that may later be adapted at optical frequencies.

A related application of communication between superconducting nodes is modular quantum

computing. A fabricated superconducting quantum processor will have some finite yield rate which decreases with the number of qubits present on the chip. One strategy for scaling up quantum processors is to divide the qubits needed for a processor among multiple chips so that they may be tested individually, discarding the bad chips and connecting the good chips through external cabling. High fidelity communication between chips would be necessary for such a scheme, with a surface code error correction threshold less than $\sim 10\%$ errors [109]. Because the connections between such chips are much shorter than those used for long-range communication, they have the opportunity to communicate using standing modes in the waveguide [110, 111, 46]. The waveguide is usually lossier than the chips,so recent work has focused on both reducing the loss of waveguide modes by engineering the waveguide connections [112], as well as avoiding the communication channel loss by adiabatically transferring the quantum states[45]. While the work here will not focus on this application, it is possible that deterministic transfer of wavepackets via pulse shaping may eventually achieve higher fidelities and faster information transfer than using standing modes because the quantum states spend less time in the waveguide.

With the view of a superconducting communication testbed in mind, we can consider which specific characteristics of a communication network we would like to reproduce at microwave frequencies. One important feature is the ability to shape the release and capture of the signal envelope. To gain some intuition for why this is important, imagine a resonator whose coupling to a waveguide is suddenly turned on. The resonator state will exponentially decay, leading to a pulse shape that has a sharp leading edge and gradually decreases in amplitude as in Fig. 5.2. This asymmetric pulse shape is difficult for the receiving resonator to capture, leading to a loss in transfer fidelity. Quantitatively, for a qubit with this type of sudden release and capture, the theoretical maximum absorption efficiency of a single photon wavepacket is 54% [113]. Alternatively, if the coupling to the waveguide is varied continuously to release a time-symmetric pulse then the theoretical maximum absorption efficiency increases to 100% [114]. This maximum absorption efficiency is an idealized case

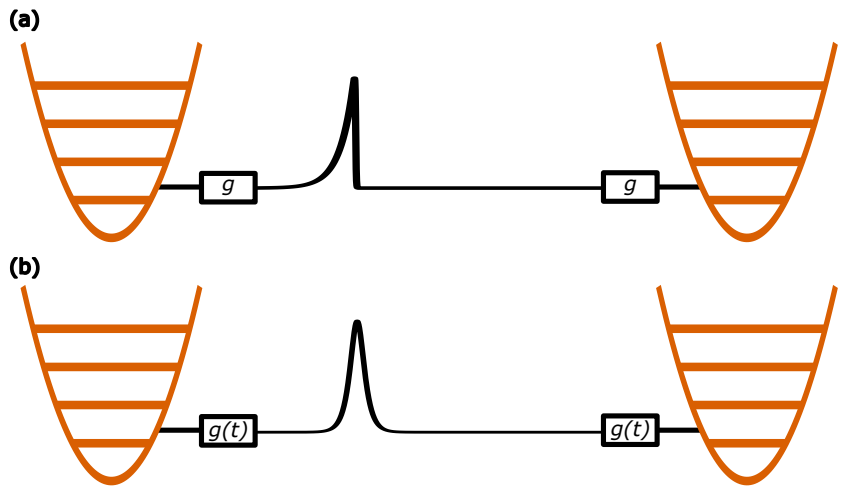

Figure 5.2: **Pulse shaping (a)** Exponential wavepacket shape from constant coupling to waveguide that is suddenly turned on, 54% maximum absorption efficiency [113]. **(b)** Symmetric wavepacket shape from shaped coupling with time-controlled coupling to waveguide, 100% maximum absorption efficiency [114].

and does not include loss in the waveguide or shaping inefficiencies. While both Ref. [113] and Ref. [114] discuss the capture of a single photon in a qubit, the argument in Ref. [114] for time-symmetric pulses generalizes to multi-photon wavepackets between resonators with time-dependent coupling to a waveguide.

We would also like to complete the the entire signal transfer from the first node A to the second B before reflections come back to the first node. This enables a theoretical analysis of the transfer as a one way transfer between A and B rather than a complex joint evolution process or a swap into a small number of waveguide modes.

A number of superconducting quantum communication results between two nodes have come out recently with these features. Refs. [115, 116] and [44] all transmitted single qubit states between the two nodes and Ref. [117] transmitted cavity states. Pulse shaping was implemented in different ways. Ref. [115] applied a microwave tone to induce transitions to a transmon's third level giving controllable coupling to a waveguide.Ref [116] drove a two-photon transition between the transmon and a buffer resonator using the protocol in Ref. [118]. Ref. [117] parametrically drove coupling between two cavities. Finally Ref. [44]

inductively coupled a transmon to a waveguide with a tunable coupler.

Refs. [115, 116] and [117] prevent reflections from returning to the original node by incorporating a circulator inside the waveguide. In these experiments, the transfer rates are much lower than the transit rates, simplifying the experimental requirements because neither strong coupling rates nor a long waveguide are required. This does however mean that the entire wavepacket does not fit in the transmission line as the cartoon in Fig. 5.2b depicts. A circulator has the additional advantage of allowing the reflected signal from the capturing cavity to be independently characterized using the circulator's third port. Ref. [44] did not include a circulator, instead making the waveguide long enough and the emission fast enough to complete the full transfer process before the reflected signal returned to the releasing qubit. Circulators have two main disadvantages: they add loss to the transfer process and prevent bidirectional communication between two nodes. The work in this thesis does not include a circulator for these reasons, although in the end the fidelity for our experiment was not significantly improved compared to these experiments for reasons discussed in later sections.

5.1 Experimental design

The goal of this experiment is to transfer a multi-photon resonator state from one resonator to another using the tunable coupling architecture first introduced in [47, 39] and used for qubit state transfer in [44]. A circuit schematic of the experiment is shown in Fig. 5.3. Each node has a frequency tunable transmon qubit capacitively coupled to its respective resonator. The transmon qubit (section 2.3.5) is used for both resonator state preparation and readout. The $\lambda/4$ resonators are frequency tunable by incorporating a SQUID at their shorted end (section 2.3.6). This frequency tunability in the resonators is used to compensate for the frequency change during wavepacket release, and to make sure both resonators are at equal frequencies. Finally, the resonators are inductively coupled to a 2 m CPW waveguide through a tunable coupler (section 2.3.4). Tunable coupling is essential for emitting time-symmetric wavepackets.

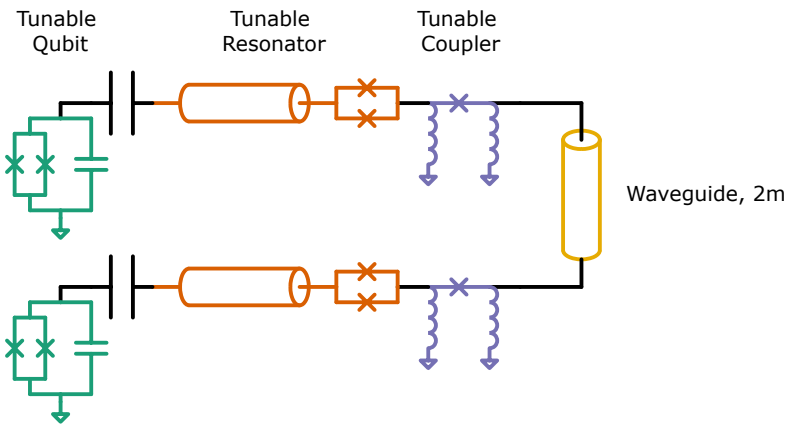

Figure 5.3: **Communication experiment circuit diagram** Circuit diagram of communication experiment with the qubit (green), tunable resonator (red), coupler (purple), and wavguide (yellow).

The transmission line is longer in this system compared to [44], so that we have more time for pulse release and capture. The next section will discuss how fast exactly we need to release the pulse, and subsequent sections will continue with other parameters we need to keep in mind when performing this experiment.

5.1.1 Resonator coupling to transmission line

If the resonator coupling to the waveguide g is much smaller than the waveguide's free spectral range ω_{FSR} ($g \ll \omega_{\mathrm{FSR}}$), we are in the weak coupling regime and the resonator can interact with the individual transmission line modes. Because the waveguide is shorted on both ends this is a half wave resonator with $f_{\mathrm{FSR}\lambda/2} = \frac{\pi c}{2\pi l\sqrt{\epsilon_{\mathrm{eff}}}} \approx 30.1\,\mathrm{MHz}$. By first swapping energy into one of these transmission line modes and then into the second resonator on the other side of the transmission line we can pass energy from one node to the other. This is the method used for example in [111]. If the length of the waveguide gets too long, ω_{FSR} becomes smaller, which requires longer and longer times to swap into a single waveguide mode. Eventually the swap time becomes so long that the information contained in the wavepacket will decohere so swapping into waveguide modes is not a feasible method for long range communication.

Alternatively, for long transmission lines it becomes more practical to enter the itinerant regime for communication between nodes. Itinerant here means that we can describe the communication process with a well defined wavepacket in time rather than with a sum of a small number of waveguide modes. Another way of saying this is that we are in the itinerant regime when a signal can be fully emitted into a transmission line without the emitter interacting with the reflected signal, which limits the maximum transfer time of our process. A CPW line on sapphire with $\epsilon_r = 11.4$ and $\epsilon_{\text{eff}} = (1+\epsilon_r)/2$ has a wave velocity of $v = \frac{c}{\sqrt{\epsilon_{\text{eff}}}} \approx 1.2 \times 10^8 \text{m/s}$. If we emit a signal into a CPW with length $l = 2\,\text{m}$, it will take about 16.6 ns to reach the other side and 33.2 ns to come back to the emission source.

For a rough estimation of the needed coupling strengths to reach the itinerant regime, we emit $1/e$ of the resonator population during a length of time equal to the emission time τ_{r0}. For m times the emission time the emitted population is $P_{\text{emit}}(t = m\tau_{r0}) = (1/e)^m$. And so if we solve for $\tau_{r0} = 33.2\,\text{ns}/m$ using the maximum transit time of 33.2 ns, we can calculate in Table 5.1 how much of the signal we emit from the resonator for various coupling strengths using our tunable coupler. From this simple calculation if we have an emission time faster than 11 ns we will be able to emit more than 95% of the signal with better performance for shorter emission times.

m	emission time	Coupling Strength	signal emitted in 33 ns
3	11 ns	15 MHz	95.0 %
5	6.6 ns	24 MHz	99.3 %
10	3.3 ns	48 MHz	99.995 %

Table 5.1: **Emission time calculations**

For more information about how the tunable coupler works see section 2.3.3. One major difficulty in producing a working device is getting a junction inductance for the coupler within the range that would let the resonators reach the itinerant regime in the waveguide.

Josephson junction inductances can fluctuate ±20% or more between fabrication runs even with nominally identical design parameters and deposition system, and so the yield rate for good devices is low.

We additionally have a SQUID at the end of the resonator so that we can tune its frequency. The frequency tuning is useful for a variety of reasons. First, it allows us to compensate for any fabrication variations that may cause slightly different frequencies in the two storage resonators. Second, it allows us to characterize the loss in different waveguide modes at weak coupling. Finally, the itinerant pulse release protocol described in Ref. [18] varies the qubit[1] frequency to compensate for the circuit loading caused by coupling to the transmission line, and so having the tunable frequency for the resonator lets us emit a signal at a single frequency (in theory). Emitting at a single frequency is not strictly necessary, because if the emission and capture protocols are precisely time-symmetric versions of each other, there is an argument to be made that the capture would still be high fidelity. However, keeping the resonator at a fixed frequency reduces the required number of parameters needed to tune up in theory. In practice, we still end up with a large number of parameters to be optimized.

To estimate the emission from the tunable resonator into the transmission line more quantitatively, we can make a linear circuit model of the system coupled to a $50\,\Omega$ resistor as shown in Fig. 5.4a. The $Z_0 = 50\,\Omega$ resistor is added to represent an infinite transmission line, as an infinite transmission line with characteristic impedance Z_0 looks the same to a lumped element circuit coupled to a resistor with resistance Z_0[27]. We can transform the system into a lumped element RLC resonator, and then solve for the total system quality factor which can then be expressed as an emission time into the transmission line.

First we determine the total equivalent impedance Z_{eq} of the circuit as a function of frequency, which can also be expressed as an equivalent admittance $Y_{\text{eq}} = 1/Z_{\text{eq}}$. If we

1. Note that in Ref. [18] the qubit is coupled to the waveguide while here the resonator is coupled to the waveguide and so the resonator frequency shifts due to loading.

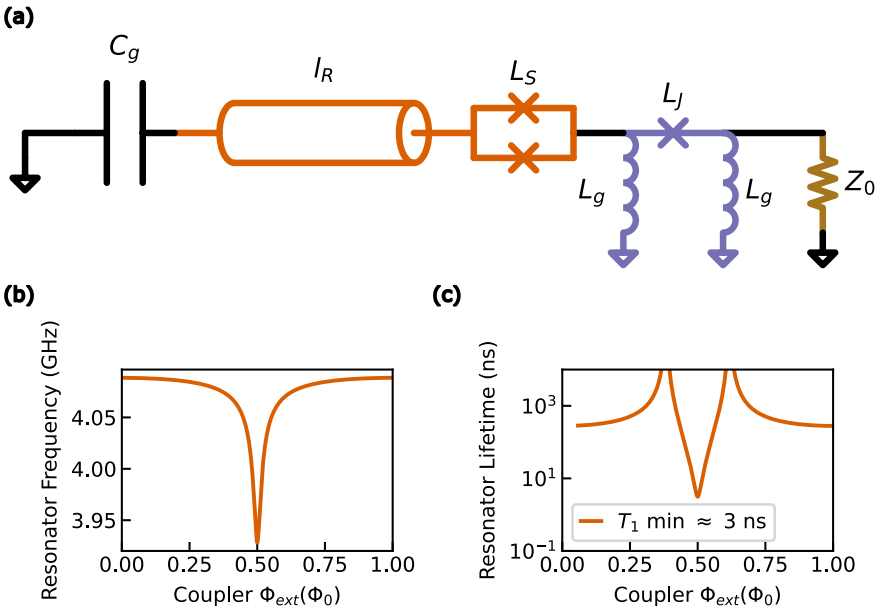

Figure 5.4: **Resonator emission circuit model.** **a** Linear circuit model of a tunable resonator coupled to a resistor. A small capacitance to ground $C_g = 10^{-14}$ F sets the boundary condition for a transmission line resonator (orange) of length l_R bounded at the other end by a SQUID with total inductance L_S. The resonator couples to a $Z_0 = 50\,\Omega$ resistor through a tunable coupler circuit (green, See Sec. 2.3.3) with inductance to ground L_g and single junction inductance L_J. **(b)** Resonant frequency for circuit model in (a) as a function of the external flux through the RF SQUID (tunable coupler), see text for inductance to flux expression to **(c)** Lifetime for circuit model in (a) as a function of the external flux through the RF SQUID.

assume a parallel (series) RLC model for the system, then the resonance can be found numerically by finding when the imaginary part of Y_{eq} (Z_{eq}) is equal to zero. For the case of a parallel RLC, we then extract the effective capacitance C_p of the resonator at a frequency ω_p using the expression $C_p = \frac{1}{2}\text{Im}\, Y'(\omega_p)$ [119]. For a series RLC we would instead get the effective inductance L_p with $L_p = \frac{1}{2}\text{Im}\, Z'(\omega_p)$. The quality factor Q_0 is given by $Q_0 = \omega_p Z_0 C_p$ for the parallel case and $Q_0 = \frac{\omega_p L_p}{R}$ for the series case [27].

Because all the components are arranged one after another in a line we can represent all the components as ABCD matrices [27] and multiply together the values to get the total impedance for all frequencies within the range of interest (in our case roughly between 1 and 10 GHz). This is made easier by using python to do the matrix multiplication, and numerically solve for both the resonance frequency and derivative.

Fig. 5.4b shows the extracted frequency using the linear model (SQUIDs are modeled as linear inductors as well) with reasonable design parameters ($l_R = 20.5\,\text{mm}$, $L_S = 0.3\,\text{nH}$, $L_{j0} = 0.6\,\text{nH}$, $L_g = 0.2\,\text{nH}$) and assuming a parallel RLC model. We can solve for $L_j = L_{j0}/\cos(\delta)$ as a function of the phase δ across the junction and then use Eq. 2.12 to convert δ to the external flux Φ_{ext}. The main feature to note here is that the coupler at different coupling strengths will significantly change the resonator frequency, which is not ideal if we want to emit at a constant frequency.Ref. [44] notes a similar coupling dependent frequency shift which was corrected for in the experiment using the qubit frequency tuning. The frequency tuning for the resonator due to the coupler has a similar origin as the "normal" tuning of the resonator described in section 2.3.6, by varying the boundary condition of a waveguide resonator.

For a given target resonator frequency, the relative tuning range of the resonator goes down for higher harmonic modes. If we use the first harmonic of the resonator instead of the fundamental mode, we can reduce the coupler-related frequency change while keeping a large tuning range with the SQUID. In addition, the resonator anharmonicity also goes down for the first harmonic as shown in Fig. 2.8, which is better for making larger photon

states in the resonator.

Fig. 5.4c shows how the resonator lifetime varies with the external coupler flux. We can see that there is a coupler external flux where the resonator lifetime is higher than μs where the coupling is "off"[2] and another coupler flux where the lifetime is a few ns where the coupling is "on". So we can turn the resonator coupling on and off with the coupler.

5.1.2 Wavepacket release and capture

Using input-output formalism with quantum pulses (Sec. 2.4.2 and [58]) we can show that it is possible to release and capture a single excitation with near unit transfer efficiency using a hyperbolic secant pulse shape, $u(t) \propto \mathrm{sech}(\kappa_c t/2)$, where κ_c is the characteristic bandwidth of the wavepacket (Fig. 5.5b and c). The cavity energy relaxation to the waveguide $\kappa(t)$ that maximizes emission into this wavepacket is given by [42]

$$\kappa(t) = \kappa_m \frac{e^{\kappa_c(t-t_0)}}{1+e^{\kappa_c(t-t_0)}}, \tag{5.1}$$

where κ_m the maximum coupling strength and t_0 varies the target output wavepacket in time. $\kappa(t)$ monotonically increases and then stays constant at its maximum value. We can vary κ_m and t_0 to maximize population into the wavepacket[3]. In Fig. 5.5, $1/\kappa_c = 2\,\mathrm{ns}$, $\kappa_m = 0.60\,\mathrm{GHz}$, $t_0 = 2.62\,\mathrm{ns}$, and have transfer efficiencies ≈ 0.99. The discrepancy from unity efficiency is likely a numerical issue as the expression is analytically derived. Keeping all parameters constant in this numerical simulation except for the number of photons in the incoming pulse we can capture the pulse with a similar efficiency. Similarly, it is possible in simulation to capture both single and multi-photon excitations from the sample wavepacket shape without changing experimental parameters after optimizing the single excitation catch.

2. although the circuit model has no internal loss, reaching infinite lifetime requires infinite precision in the coupler flux in simulation

3. If we vary t_0 away from release window, the resonator would still decay as expected, but there would not be any excitations contained in the time envelope for the wavepacket shape we defined

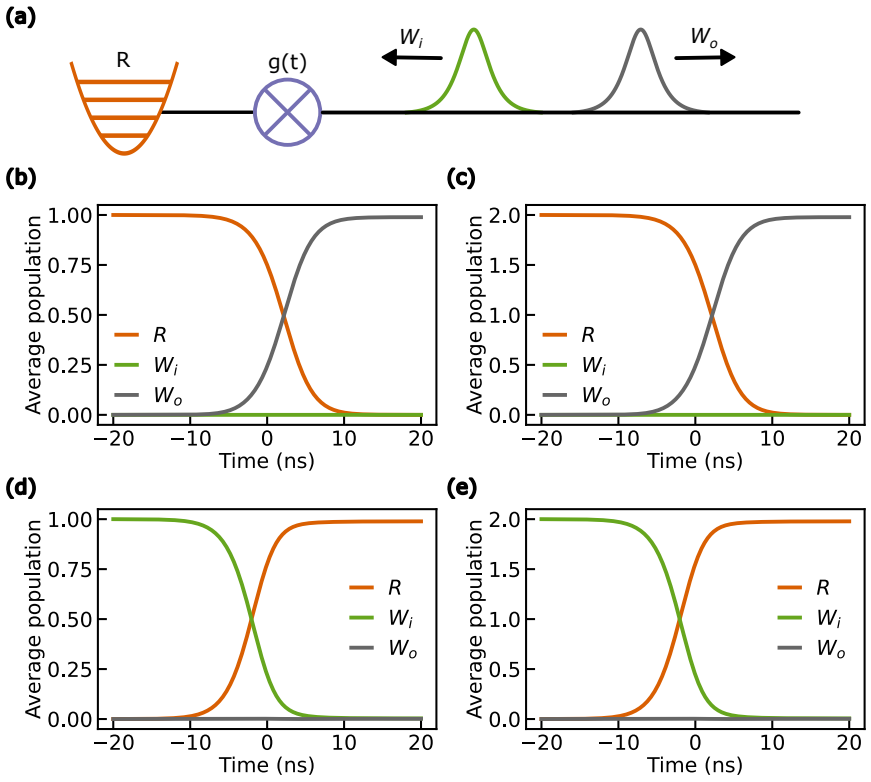

Figure 5.5: **Input-output catch and release simulations.** **(a)** Cartoon representing resonator R coupled to waveguide through tunable coupling $g(t)$ with an incoming hyperbolic secant wavepacket W_i and outgoing wavepacket W_o. **(b,c)** Releasing 1 and 2 photons respectively from R into W_o with high efficiency (99% population transfer) using the same release parameters. **(d,e)** Capturing 1 and 2 photons respectively into R from W_i with high efficiency (99% population transfer) using the same capture parameters.

The fact that pulse shaping may be independent of the photon number might be counter-intuitive when considering that coupling strength scales with $\sqrt{n}$, where n is the total number of photons prepared in the resonator. One might then expect to need different pulse shapes for different prepared photon numbers in the resonator. It may be useful to consider that the pulse shape here is a distribution of the total energy of the resonator, while the $\sqrt{n}$ refers to the coupling for a single photon at the top of the resonator level structure to decay. So while individual photons will decay faster into the waveguide for higher n, the percentage of the total energy in the resonator will be emitted out at the same rate.

5.1.3 Resonator Control

A qubit lets us generate quantum states in a resonator. While this state control can be done dispersively [120, 121] here we will follow a method that tunes the qubit to be on resonance with the resonator [122, 123, 124]. When the qubit and resonator are far detuned from each other ($\omega_r - \omega_q \gg g_{qr}$), they do not exchange energy with each other, although they may affect the phases of each other's states through the dispersive interaction. If the qubit is excited to $|e\rangle$ and the resonator is in its ground state, when the two systems are brought into resonance the excitation will transfer to the resonator in time $\tau_0 = \pi/2g$ as shown in Fig. 5.6a. For a resonator prepared in a higher excited state n this transfer time will become faster as $\tau_n = \tau_0/\sqrt{n}$. So one method of preparing multi-photon resonator states is by repeatedly exciting and swapping the qubit excitation into the resonator (Fig. 5.6b).

Fig. 5.6c-d further show how we can make the state $|0\rangle+|N\rangle$ in the resonator by just using qubit excitations and swaps [125]. A $|0\rangle + |1\rangle$ resonator state is made by first preparing a $|g\rangle+|e\rangle$ qubit state with a $\pi/2$ pulse. We can then swap the excited state into the resonator. For higher N we can first excite the transmon to $|g\rangle + |f\rangle$, swap the highest excitation into the resonator, and repeatedly excite and swap between $|e\rangle$ and $|f\rangle$ until we finish with the qubit in its ground state. Fig. 5.6d shows this sequence for $N = 2$. See section 5.3.6 and later sections for states prepared using these sequences.

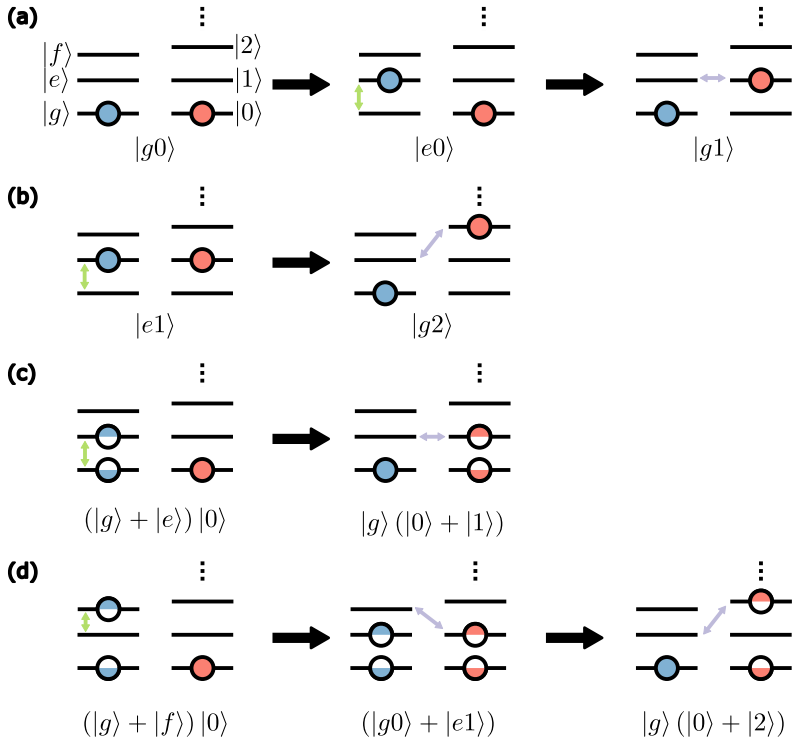

Figure 5.6: **Resonator Fock and superposition state preparation(a)** Steps to prepare a single photon state by swapping excitations from a transmon qubit. The qubit is depicted on the left (blue) and resonator on the right (red). Both systems are initially prepared in their respective ground states. The qubit is excited to $|e\rangle$, and then that excitation is swapped into the resonator in time τ_{swap} with both systems on resonance. **(b)** A two-photon state in the resonator can be prepared by starting with the single photon state in (a), exciting the qubit, then swapping the excitation to the resonator in time $\tau_{\text{swap}}/\sqrt{2}$. **(c)** A resonator $|0\rangle + |1\rangle$ state can be prepared by first preparing $|g\rangle + |e\rangle$ in the qubit, then swapping the excited state to the resonator. **(d)** A resonator $|0\rangle + |2\rangle$ can be prepared by starting from the qubit $|g\rangle + |e\rangle$ state (first step in (c)) then exciting the qubit to $g\rangle + |f\rangle$. Two swaps into the resonator (both $\tau_{\text{swap}}/\sqrt{2}$) will then create a $|0\rangle + |2\rangle$ resonator state.

5.1.4 Component tests

For an experiment with a large number of parts such as this, it is generally a good idea to first test each component part on its own to confirm we understand that they behave as we expect. While in our lab at UChicago we had experience making, controlling, and measuring superconducting qubits, we had not made tunable resonators. Similarly, while previous experiments have made CPW waveguides up to 78 cm [44], we had not made any up to 2 m. These are both components to test before assembling the full experiment.

We tested an array of tunable resonators in a similar experiment as in the airbridge test from section 2.2.5 as shown in Fig. 5.7. Several tunable resonators were inductively coupled to a measurement line, and we fit the $\tilde{S}_{21}$ as a function of the applied flux to the DC SQUIDs. Tracking the resonant frequency of a single resonator as a function of flux as shown in Fig. 5.7d, we confirmed that the resonators tune downwards as a function of the applied flux. We also noted that the quality factor went down (Fig. 5.7e) as in [54]. Due to the resonators' nonlinearity, these measurements were done at low power, populating the resonator with on average < 10 photons.

For the second test primarily intended to gauge the feasibility of fabricating 2 m transmission lines for the communication experiment, we added a SQUID to the end of a the waveguide resonator as shown in Fig. 5.8a and b. This is a similar setup to other recent parametric cavity experiments such as [126]. A wide scan confirmed that the multimode resonator had the expected separation between resonances. The frequency tuned as a function of frequency. We can also track Q_i for a single mode as a function of tuning frequency, and find a minimum at intermediate detunings and maximum at the highest and lowest frequencies. This is qualitatively consistent with a lossy junction and the fraction of energy contained in the junction (participation ratio) as a function of detuning.

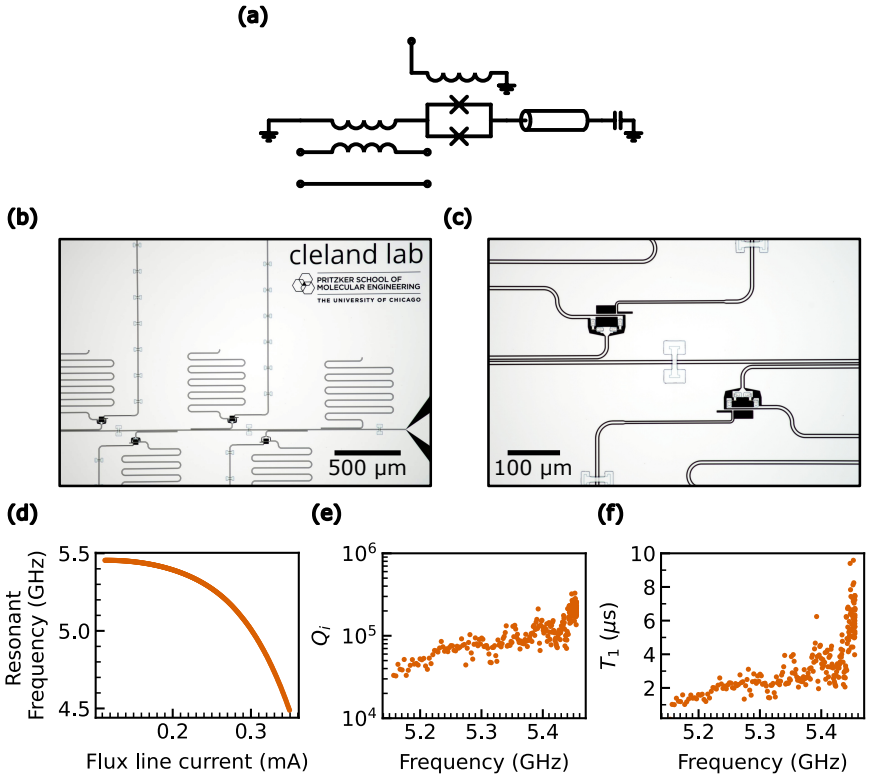

Figure 5.7: **Tunable resonator test.** **(a)** Circuit model for tunable resonator test. The resonator is inductively coupled to a measurement line and the resonator has a SQUID which is flux coupled on chip.**(b)** Microscope picture of tunable resonator test. There are multiple test tunable resonators at different frequencies and a CPW without a SQUID for reference. **(c)** Zoomed in picture showing inductive coupling and SQUIDs for tunable resonators. **(d)** The resonator with a maximum resonance around 5.5 GHz is tuned by applying a current to the flux line and the resonance frequency measured at low power (< 10 photons in resonator). Tunable range is shown to be at least 1 GHz. Total tuning range is in principle larger than this, however fits become noisier at lower frequencies due to loss as seen in (e). **(e)** The internal quality factor near the resonator maximum is fit as a function of resonator frequency. The resonator's quality factor goes down by an order of magnitude with ≈ 300 MHz detuning from its maximum. **(f)** $T_1 = Q_i/\omega_r$ where ω_r is the resonator's angular frequency.

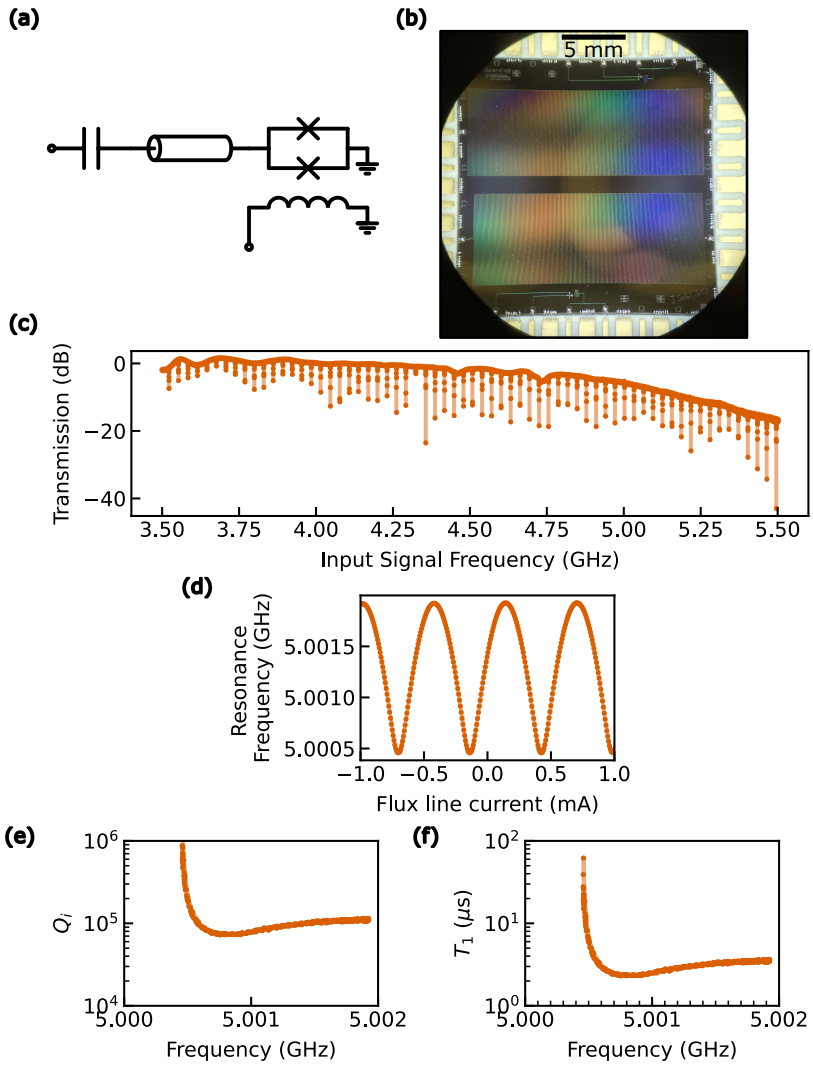

Figure 5.8: **2 meter tunable multi-mode resonator.** **(a)** Circuit model for multi-mode resonator. **(b)** Microscope picture of sample. Two separate 2 m long CPW lines are seen. The top line was directly connected to a measurement line on either side of the CPW, however was measured to be shorted. The bottom line has the circuit model shown in (a). **(c)** Measuring the cavity through the weakly coupled capacitor in reflection at low photon number (< 10) shows a large number of resonances separated by the expected 31 MHz spacing, confirming as a proof of principle that it is possible to fabricate a 2 m CPW without shorts. After the signal reflects off the cavity, we use a circulator to measure the transmission. **(d)** Measuring a mode around 5 GHz tuning as a function of current in the flux line. The tuning range is only ≈ 15 MHz due to the long resonator length. **(e)** The quality factor was fit for the mode in (c) throughout the tuning range, showing the previously seen decrease with tuning. This behavior can be qualitatively explained assuming the SQUID is the lossiest element in the resonator and the energy distribution (participation ratio) varying with resonator tuning. The sharp rise at the minimum detuning can be explained by the SQUID's high impedance reducing the energy participation below even the value at maximum frequency. **(f)** $T_1 = Q_i/\omega_r$ where ω_r is the resonator's angular frequency.

5.1.5 Chip Layout

All components are fabricated on a single 2 x 2 cm sapphire substrate as shown in Fig. 5.9b. The qubits are capacitively coupled to $\lambda/4$ readout resonators that inductively couple to a measurement line through a Purcell filter (See Appendix C).

The unusually large chip size is needed to fit the entire transmission line on chip. Unfortunately, at this chip size the box modes of both the chip and package are near experimentally relevant frequencies with the frequencies f_{nml} given by [31]

$$f_{nml} = \frac{c}{2\pi\mu_r\epsilon_r}\sqrt{\left(\frac{n\pi}{a}\right)^2 + \left(\frac{m\pi}{b}\right)^2 + \left(\frac{l\pi}{d}\right)^2}, \tag{5.2}$$

where n, m, and l are the mode numbers for the transverse electric (TE) and transverse magnetic (TM) modes in a rectangular cavity, with two out of the three non-zero. μ_r and ϵ_r are the relative permeability and permittivity, c is the speed of light and a, b, and d are the cavity dimensions (x,y,z for example).

For both the chip and package, the z dimension is small enough to be ignored. For a 20 mm sapphire chip with $\epsilon_r = 11.4$, the lowest frequency mode is $f_{110chip} = 3.14$ GHz while using $\epsilon_r = 1$ and 27 mm side for the package mode gives $f_{110package} = 7.85$ GHz. From this quick calculation the chip modes will definitely be within our typical superconducting circuit operating frequencies of 4-8 GHz while the package mode might be avoided if we design our frequencies low enough.

5.1.6 Wiring

A wiring diagram of the experiment is shown in Fig. 5.10. The wiring here is fairly typical of our setups, although IR filters are used to reduce thermal noise for many device lines (both microwave and dc lines). The output of the experiment is connected to a TWPA obtained from Lincoln Laboratories with a noise temperature measured in our lab of around 500 mK. Two circulators are placed before the TWPA to prevent the qubit from seeing the TWPA

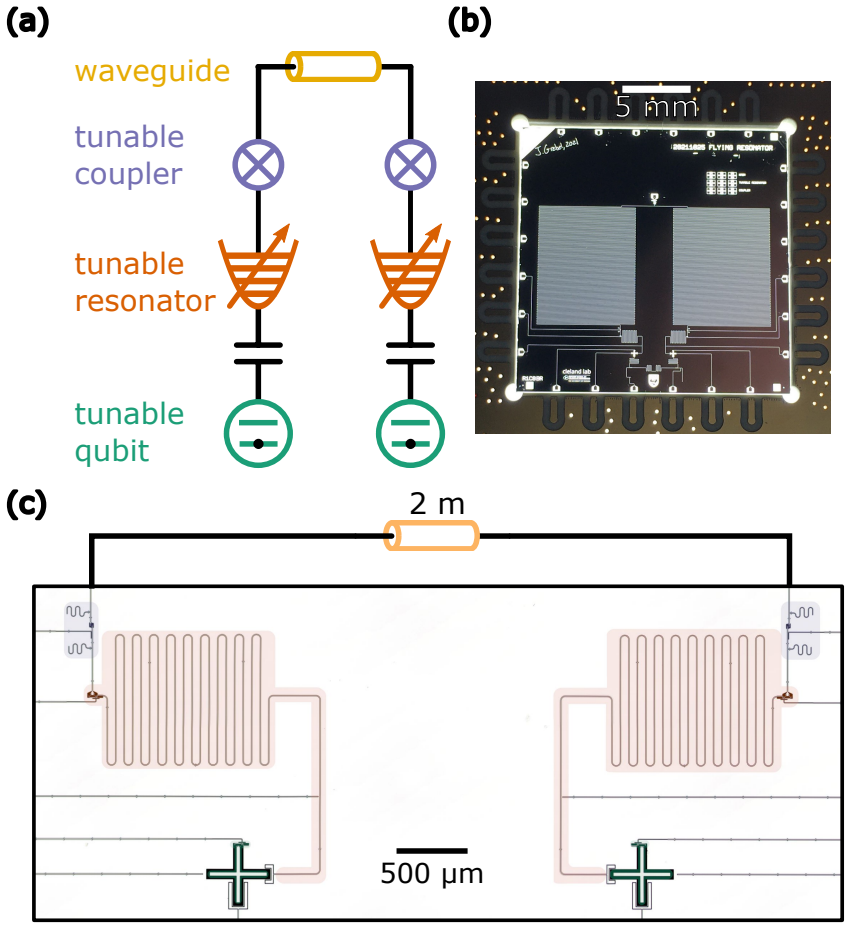

Figure 5.9: **Communication experiment layout(a)** Block diagram for experiment. **(b)** Backside illuminated chip showing all components as well as PCB board for signal routing **(c)** Micrograph of device with false coloring corresponding to components shown in (a).

pump and backwards amplified noise [127].

5.2 Device characterization

Once the dilution refrigerator reaches the base temperature of around 10 mK, we can start tuning up the various parts of our system. In order this will include the two qubits, the tunable resonators, and finally the couplers. A single qubit tuneup tutorial is presented in Appendix D.

5.2.1 Qubit/Resonator coupling

Two-tone spectroscopy [128] (See Appendix D) as a function of qubit bias will reveal any avoided level crossings due to the qubit interacting with coupled systems such as the tunable resonator. In Fig. 5.11a and b there is an avoid level crossing near the resonator design frequency, with coupling strength roughly 7 MHz . A simple way to confirm that this is the tunable resonator is to excite the qubit, and then vary both the qubit bias and resonator bias at a long delay time such that the qubit will lose population when both are on resonance. (Fig. 5.11d). For initial experiment tune-up, it is useful to first place the resonator near its maximum frequency to maximize the expected resonator lifetime [54].

5.2.2 Coupler characterization

We can now swap an excitation into the resonator to find the parameter regimes where the coupler is on and off as shown in Fig. 5.12. In the strong coupling regime with the waveguide, the resonator decays exponentially before reflections return (after about 30 ns). We can reach a regime where the resonator can release its state with characteristic time 4 ns, which is fast enough for us to do our experiment. We can also turn the coupling off (Fig. 5.12b) by waiting for a long delay time and finding the point at which we do not see transmission line modes. We can continuously vary the coupling strength between these two

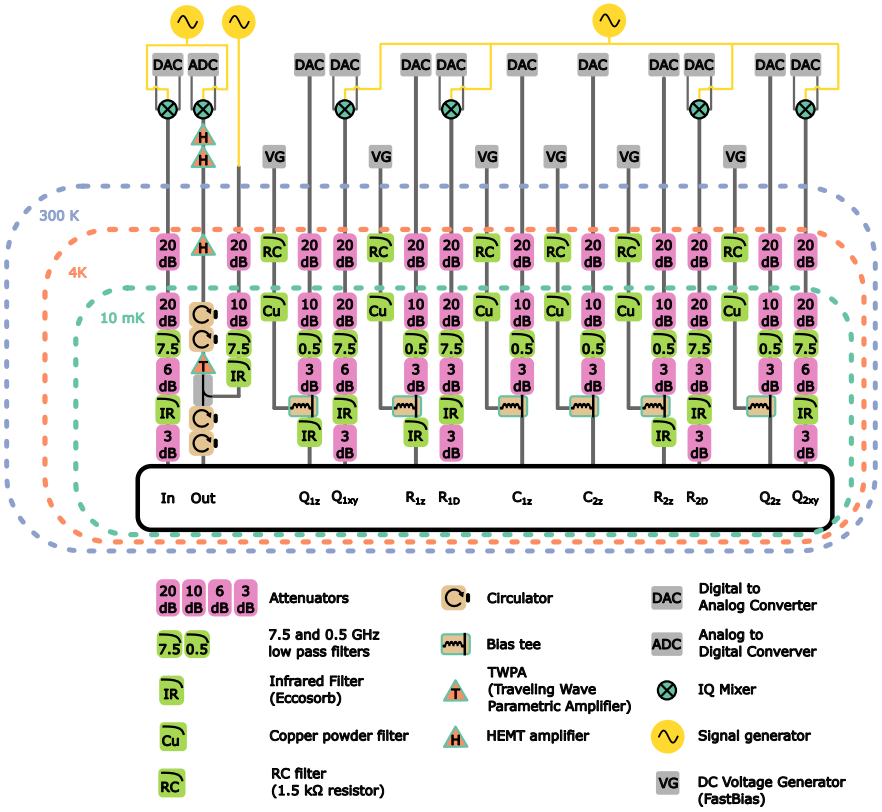

Figure 5.10: **Communication experiment wiring diagram.** Wiring diagram showing room temperature electronics, attenuations, and amplifiers. Input and output lines are used for qubit state readout. Qubits (Q) and resonators (R)have a microwave (XY, D) line and current bias (Z) line, with the Z line combined with a low noise continuous bias current component and fast bias components through a bias tee. Couplers only have a current bias line. Microwave signals are generated at room temperature using continuous signal generators that are then modulated by IQ mixers controlled by DACs. Microwave drive lines (In, xy, and D) are attenuated to reduce thermal noise. Low noise voltage generators at room temperature are used as a current source by going through a 1.5 kΩ resistor. For more information about DR wiring see section 3.1.3.

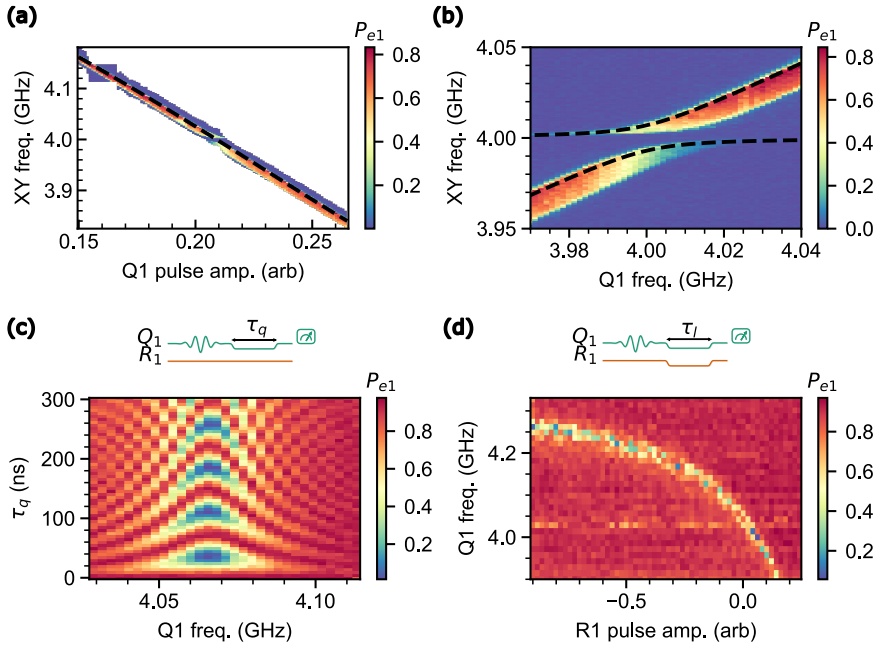

Figure 5.11: **Tunable resonator initial scans(a)** Qubit two-tone spectroscopy (See Appendix D), with data collected by tracking the peak maxima in frequency as the qubit pulse amplitude is varied. Fitting this plot to a polynomial function we can convert dc pulse amplitude to qubit frequency. **(b)** Zooming into the avoided level crossing, we see that the two-tone spectroscopy peak is broadened, likely due to pulse distortion in the qubit flux bias. We can fit the avoided level crossing by eye to be approximately $g/2\pi \approx 7\,\mathrm{MHz}$. **(c)** After correcting for pulse distortion [129], the qubit/resonator swaps show the characteristic chevron shape. **(d)** After exciting the qubit apply flux bias to both qubit and resonator for a long time $\tau_l = 500\,\mathrm{ns}$. When the qubit is on resonance with the resonator there is lower qubit population.

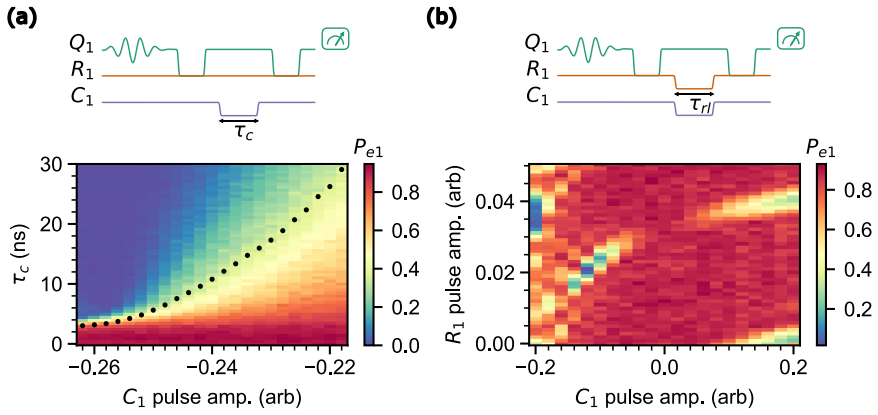

Figure 5.12: **Coupler control.** **(a)** Swapping an excitation into the resonator, and then varying the coupler flux we can bring the resonator into the strong coupling regime. Black dots are exponential fits to the decay, showing we can release a state in under 4 ns. **(b)** Method for turning coupling off. At weak coupling the resonator lifetime primary decay mechanism is not the coupling to the waveguide, so we can't just maximize the lifetime to turn the coupling off. Instead, after swapping into the resonator we set the delay time $\tau_{rl} = 200$ ns to a long time and then vary the resonator flux bias to see transmission line modes. When the coupling is turned off, these modes disappear (here at 0 C_1 pulse amplitude).

extremes.

5.2.3 Resonator characterization

We can do a T_1 measurement of the resonator by swapping an excitation into the resonator, waiting for a delay time τ_r and then swapping back to the qubit as shown in Fig. 5.13a and b. By varying the resonator bias during this delay we can track how the resonator lifetime varies with frequency. While resonator R_1 does show the decrease in lifetime expected with detuning, there appears to be a lossy mode near 4.2 GHz. Resonator R_2 also has a similar lossy feature around 4.2 GHz, however its lifetime is flat for lower detunings indicating something apart from the DC SQUID is its primary loss mechanism.

5.2.4 Flux Crosstalk

Flux crosstalk is the undesirable flux that goes into all other components apart from the target device. This may cause issues if we want to independently tune up components one

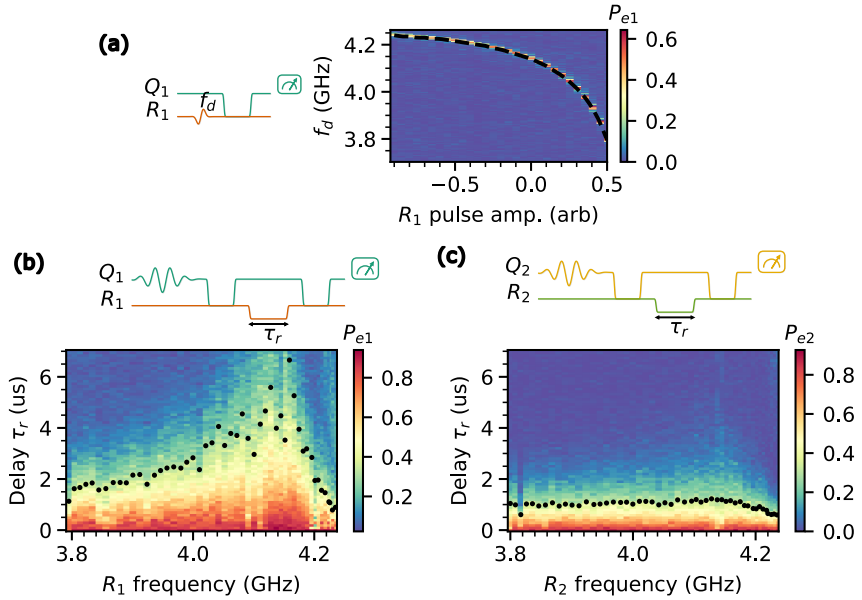

Figure 5.13: **Tunable resonator lifetime.** **(a)** The resonator frequency is calibrated by applying a displacement pulse at frequency f_d on the resonator at different flux biases and then swapping the excitation into the qubit at the 1 photon swap period $\tau_0 = 38\,\text{ns}$. The frequencies at which the resonator is excited can then be detected by the qubit population after the sequence and interpolated (dotted line). **(b)** T_1 measurement of R_1 as a function of its frequency. Black dots are fits to exponential decay. While the resonator T_1 does go down with frequency there is a sharp decrease in lifetime above 4.2 GHz, possibly a box or chip mode interacting with the resonator. **(c)** T_1 measurement of R_2. T_1 is flat with frequency below 4.2 GHz (with a similar drop as in (a) above 4.2 GHz and similar shape at long delay τ_r). This may indicate that the resonator's DC SQUID is not the dominant loss channel.

at a time. For flux crosstalk between two components A and B, we can correct for crosstalk from the B flux line on A by applying a correction pulse on the A flux line. The remaining issue is to figure out how large of a correction pulse we need to apply. In general, for n different components, we need to measure and correct for $n \times n$ correction terms [130, 17]. Ref. [130] has a device composed of only qubits and couplers, and measures this crosstalk by using an ancilla qubit to detect small changes in frequency due to other components. [17] measures this crosstalk in a simpler system with only a single qubit and coupler by varying the bias on both components and looking for periodic features in the transmission amplitude of the readout resonator for the qubit. Neither of these strategies will let us fully measure the crosstalk in our system, and so we will use different methods to discover the crosstalk acting on different parts of the system.

We have 6 SQUIDs on the chip that may be affected by flux crosstalk: two qubits, two resonators, and two couplers. This will lead to a 6x6 flux crosstalk matrix. All these components have their own flux lines as well, so in theory we should be able to fully correct the flux crosstalk. The philosophy behind the following strategies is to find a parameter (frequency, coupling strength) which we assume to be invariant (to first order) when a bias is applied to other components, but we actually see a much larger change due to crosstalk. This assumption is not fully valid, as all parameters in the system affect each other even in the absence of crosstalk. But correcting the crosstalk in this manner should let us reduce the dependence of components on each other.

First we correct flux crosstalk on each qubit. Correcting this crosstalk may be useful if we want to do simultaneous swaps with both qubits and resonators. Alternatively, we could only tune up the specific operation that we need, but this measurement is straightforward enough to correct the general case. The qubit readout visibility is sensitive to the qubit frequency. By measuring the qubit readout visibility as a function of the qubit bias and some other bias we can apply a correction such that the visibility does not depend on that other parameter (Fig. 5.14a). Although the qubit is capacitively coupled to the tunable

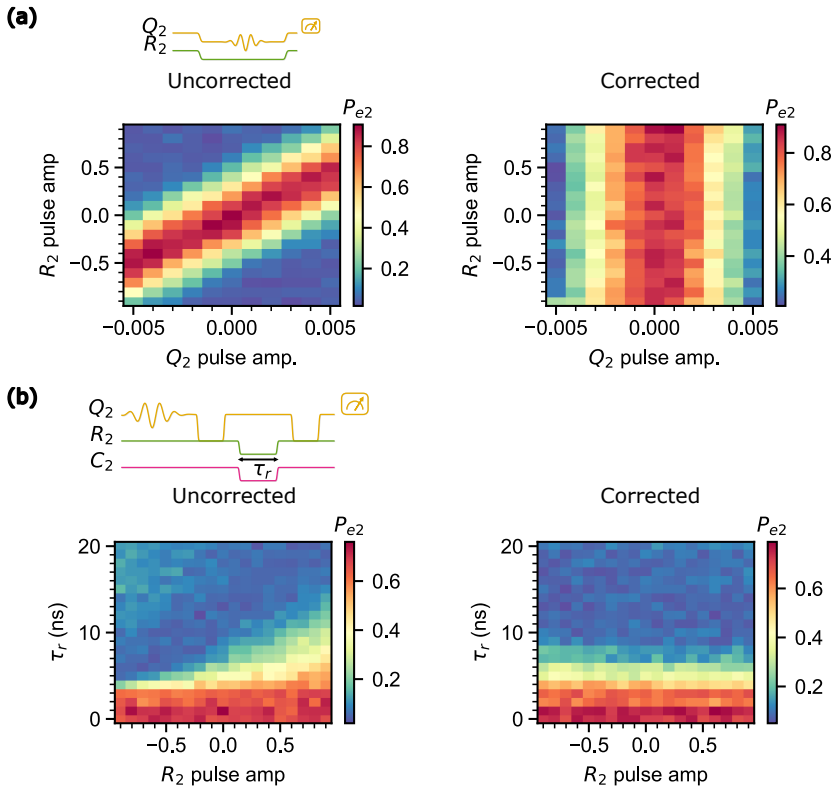

Figure 5.14: **Flux crosstalk correction.** **(a)** Qubit flux crosstalk correction. We applying a π pulse to the qubit while varying the qubit flux bias and some other bias, here a resonator bias. The qubit visibility should not depend on the non-qubit bias. **(b)** Coupler flux crosstalk correction. We swap an excitation from the qubit into the resonator. In the itinerant regime, the decay rate should not depend on parameters apart from the coupler flux.

resonator, the qubit frequency will only be weakly changed as we vary the tunable resonator frequency when the detuning between the two is large (a few hundred MHz).

Second, we can correct flux crosstalk on the coupler. Correcting this crosstalk is important for when we compensate the frequency detuning due to strong coupling to the waveguide, and want to make sure that the coupling vs. time is not affected. When the tunable resonator is strongly coupled to an external waveguide the energy in the resonator will exponentially decay, until reflections in the waveguide return to the resonator. This decay rate g should not depend on the biases applied to other components, except for the bias on the tunable resonator itself to change the resonator frequency. For detunings of a few hundred MHz from a maximum frequency of several GHz, the resonator decay rate g should only vary on

the order of a few percent. We can then assume that larger changes in the coupling rate when varying the resonator frequency are due to flux crosstalk. This correction is shown in Fig. 5.14b.

We do not correct flux crosstalk on the tunable resonator. It should in theory be possible to measure this crosstalk from most of the components by doing a Ramsey-like measurement where we swap energy into the resonator to precisely measure its frequency change due to other components. Note this technique would not work for the coupler connected to the resonator as coupler bias strongly affects the resonator frequency even in the absence of crosstalk.

5.2.5 Waveguide Characterization

We would like to confirm that the waveguide is free from defects or sources of loss. To investigate defects in the transmission line we can check that the modes in the transmission line are equally spaced by the expected Free Spectral Range (FSR). If there was some capacitive or inductive structure in the waveguide it would cause the standing modes of the waveguide to deviate from uniform FSR, because each mode has a different participation with the structures depending on the mode shape. This mode spacing can be measured using a technique similar to two-tone spectroscopy as shown in Fig. 5.15a. While the resonator is weakly coupled to the waveguide we apply a weak displacement pulse to the resonator, followed by a swap in energy to the qubit and then measuring the excitation. In this plot we see avoided level crossings between the resonator and waveguide modes, and can check if their spacing is uniform. Using this technique, we discovered that an electrical probe we placed in the waveguide to check if there were shorts was causing a significant impedance mismatch in the line which caused reflections. Modeling the probe as a 500 μm transmission line terminated by a 0.1 pF capacitor, we find that this structure would have a reflection magnitude $|\Gamma| = 0.12$ (amplitude not power). To correct this issue we cut the electrical probe (using a wirebond tool with a used/damaged tip, Fig. 5.15c) on chip to a $\approx 250\,\mu$m stub with

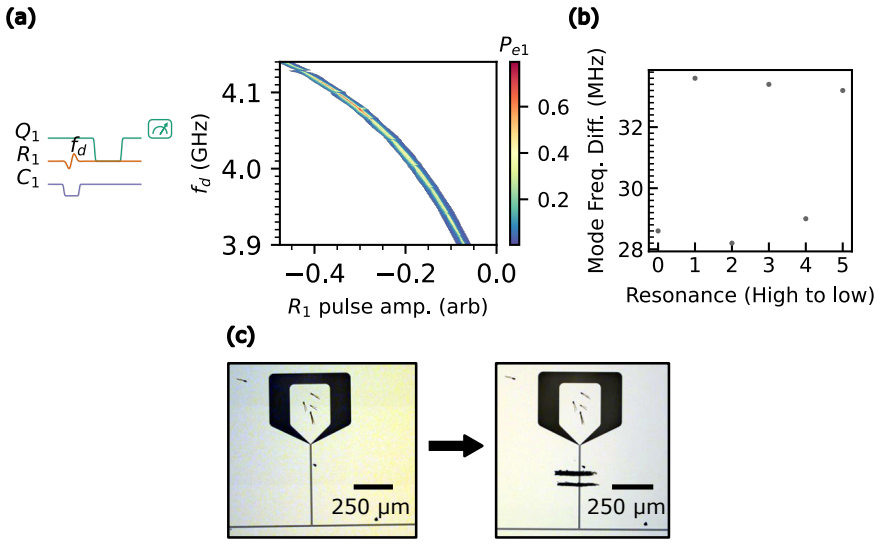

Figure 5.15: **Waveguide probe capacitive loading.** **(a)**In a DR cooldown before the final experiment, we probed the frequency of the waveguide modes by displacing the resonator while weakly coupled to the waveguide.**(b)** The frequency difference between the modes was not constant, but alternated by mode (modes here from figure (a)). **(c)** Cutting the probe with an old wire bonder tip reduces the capacitive loading in the waveguide.

large capacitance to ground which substantially reduces the undesired reflections to below $|\Gamma| < 0.03$ from simulation. After cutting this probe, we do not see substantial frequency variations in the waveguide mode spacing with the weakly coupled resonator displacement technique.

We can also swap an excitation into a waveguide standing mode to characterize its loss as shown in Fig. 5.16b. Measuring the lifetime of individual waveguide standing modes in the weak coupling regime is a useful technique because as we increase the coupling we interact with more waveguide modes at once. The strong coupling regime can then be thought of as a resonator interacting with a large number of waveguide standing modes, whose loss properties can inferred from the weak coupling regime. Considering the lower than expected transfer efficiency in this experiment, the standing mode loss measurement strongly suggests that waveguide loss is not the fundamental limitation in the experiment.

A summary of the experimental parameters is given in Tables 5.2 and 5.3.

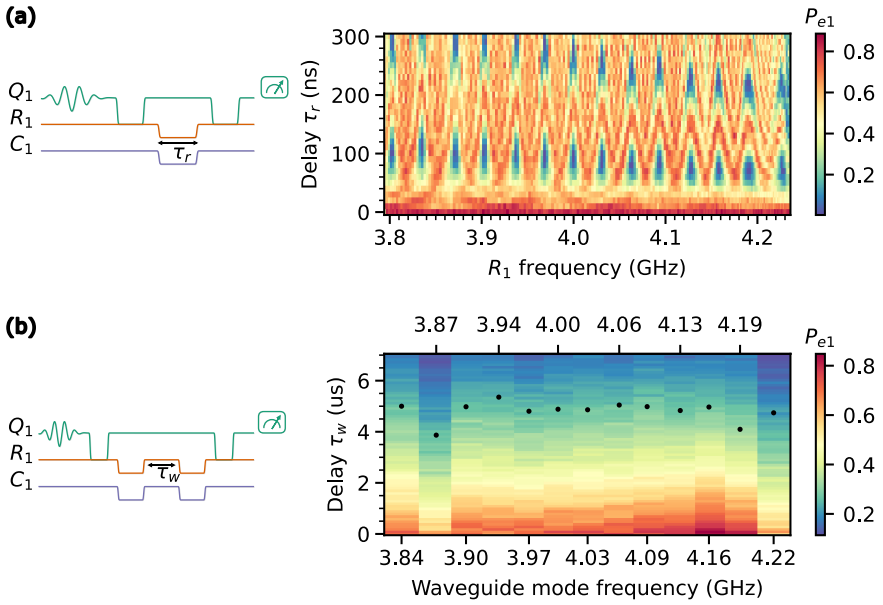

Figure 5.16: **Waveguide mode characterization(a)** Waveguide modes seen by R_1. A single photon excitation from Q_1 is swapped into R_1, then the resonator frequency is tuned with weak coupling turned on to the waveguide for variable time τ_r. The excitation is then swapped back to Q_1. **(b)** Waveguide mode T_1 measurement. A 1 photon excitation from Q_1 is swapped first into R_1 and then into a waveguide mode. After waiting variable time τ_w, the excitation is swapped back to R_1 and then to Q_1.

Qubit parameters	Qubit 1	Qubit 2
Qubit bare frequency, $\omega_{qb}/2\pi$	6.250 GHz	6.242 GHz
Qubit capacitance, C_q (design value)	90 fF	90 fF
Qubit anharmonicity α_q	-192 MHz	-192 MHz
Qubit lifetime, T_{1q}	20 μs	22 μs
Qubit Ramsey dephasing time, $T_{2q,\text{Ramsey}}$	2.62 μs	0.56 μs
Qubit spin-echo dephasing time, T_{2E} (μs)	4.20 μs	3.95 μs
$\|e\rangle$ state readout fidelity, F_e	0.95	0.96
$\|g\rangle$ state readout fidelity, F_g	0.98	0.97
Thermal excited state population	0.010	0.026
Readout resonator frequency, $\omega_{ro}/2\pi$	5.358 GHz	5.312 GHz
Readout resonator decay rate (design value), $\kappa_r/2\pi$	4.58 MHz	4.58 MHz
Readout dispersive shift, $\chi/2\pi$	1.4 MHz	1.3 MHz

Purcell filter parameters	value
Input quality factor (design value), Q_{fi}	~ 2000
Output quality factor (design value), Q_{fo}	15.5
Purcell filter frequency (design value), $\omega_p/2\pi$	5.29 GHz

Table 5.2: **Communication experiment, qubit and readout parameters.**

Tunable resonator parameters	Resonator 1	Resonator 2
Qubit/resonator coupling, $g_{qr}/2\pi$	6.805 MHz	6.830 MHz
Resonator lifetime, T_{1r}	4.57 μs	0.86 μs
Resonator Ramsey dephasing time, $T_{2r,\mathrm{Ramsey}}$	0.95 μs	0.90 μs
Resonator bare frequency $\omega_r/2\pi$	4.269 GHz	4.269 GHz
Resonator DC SQUID inductance (design value), L_{rs}	0.25 nH	0.25 nH

Tunable coupler parameters	Coupler 1	Coupler 2
Coupler junction inductance (design value) L_{cj}	0.6 nH	0.6 nH
Coupler grounding inductance, L_g (design value)	0.2 nH	0.2 nH
Coupler stray inductance, L_g (assumed design value)	0.1 nH	0.1 nH

Table 5.3: **Communication experiment, resonator and coupler parameters.**

5.2.6 Wavepacket Characterization

Before optimizing the release and capture of the wavepackets, we can roughly estimate the wavepacket shape by applying a flattop pulse (Gaussian convolved with rectangular pulse) with varying rise times w and then monitor the resonator population as a function of time while strongly coupled to the waveguide, as shown in Fig. 5.17a. This is not in general an optimized coupling shape, however it can give us a sense of the range of wavepacket shapes we can generate. If the coupling to the waveguide is ramped up quickly, then the release will be dominated by an exponential decay and lead to an asymmetric curve as was illustrated in the cartoon in Fig. 5.2a. For slow Gaussian ramp up the asymmetry will be in the opposite direction. We can characterize this asymmetry by modeling the wavepacket as a skewed hyperbolic secant $f(t, \theta, w)$ with skew θ and width w.

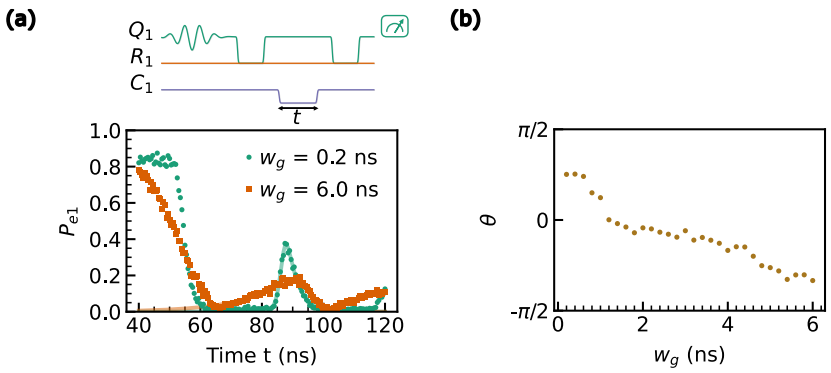

Figure 5.17: **Wavepacket asymmetry (a)** Releasing a wavepacket with a flattop pulse of varying Gaussian rise widths w_g. The wavepacket bounces off the other end of the waveguide and we measure the resonator population with the coupler fully on. The wavepackets are then fit to a skewed hyperbolic secant with skew θ shown in (b), excluding the data points from release and second reflection.**(b)** Varying w_g and fitting the wavepackets we see a decreasing trend between w_g and θ.

$$f(t) = \cos\theta \frac{e^{\frac{\theta(t-t_0)}{w}}}{2\cosh\left(\frac{\pi(t-t_0)}{2w}\right)}. \tag{5.3}$$

The exponential adds a skew to a hyperbolic secant function, and the cosine normalizes the integral of the function to one. This function is not derived from the experimental circuit, it simply happens to fit the data reasonably well and lets us extract the skew of the wavepacket from a fit[4]. Ideally, the skew should be zero for a time-symmetric wavepacket. Fitting the wavepackets with this function as shown in Fig. 5.17b, we see we can generate a range of asymmetries for the wavepacket. This is only a rough estimate for the wavepacket shape as the time to turn off the coupling is finite and so distorts the measured pulse shape. For optimizing pulse shapes later we will instead directly optimize by maximizing the population transfer between resonators.

4. Aside from specifying the wavepacket shape directly we could have alternatively derived how the release would look given an applied pulse distorted by Gaussian filters and the tunable coupler as in [18]. Due to the large number of free parameters in such a derivation, it does not necessarily provide more information than the method used here.

5.3 State transfer

5.3.1 Single excitation transfer, Swaps

The simplest method to transfer energy through the waveguide is to swap an excitation from the first qubit to its coupled resonator, swap into a single waveguide mode, swap into the second resonator and finally swap to the second qubit. This lets us confirm that the waveguide does not have any shorts. After exciting qubit1 and swapping through the resonators and waveguide, we measure around 0.78 population in the second qubit. Much of the loss in this transfer can be explained by decay in the various components. For the full 290 ns swap transfer process, if we roughly estimate the time the excitation spends in each component we would expect to see around 0.86 population remaining. We also have 0.96 $|e\rangle$ state readout fidelity for qubit 2, reducing the expected population to 0.83. The rest of the discrepancy may be due to incomplete energy transfer between components which might be solved by better pulse calibration.

5.3.2 Single excitation transfer, wavepacket

Transferring a single excitation using a wavepacket instead of swapping with single modes requires shaping the release and capture of the excitation between both resonators. Optimizing the release and capture process for a single excitation is critical for achieving good fidelity for general resonator state transfer as noted in Sec. 5.1.2. One method for optimization is to reproduce the hyperbolic secant pulse shapes and timing as given in simulation as in [42]. Gaussian filters in our wiring will smooth arbitrarily generated pulses on the order of 3 ns, so full control of the pulse shape may not be achievable in our experiment. A simpler method for optimization is to apply rectangular pulses convolved with gaussians (flattop shape) and vary the pulse length and rise time to optimize the transfer efficiency as in [44]. We follow a slightly different strategy here and use a Bayesian optimization package to vary the pulse shape for release and capture [131], maximizing the total transferred amplitude from an

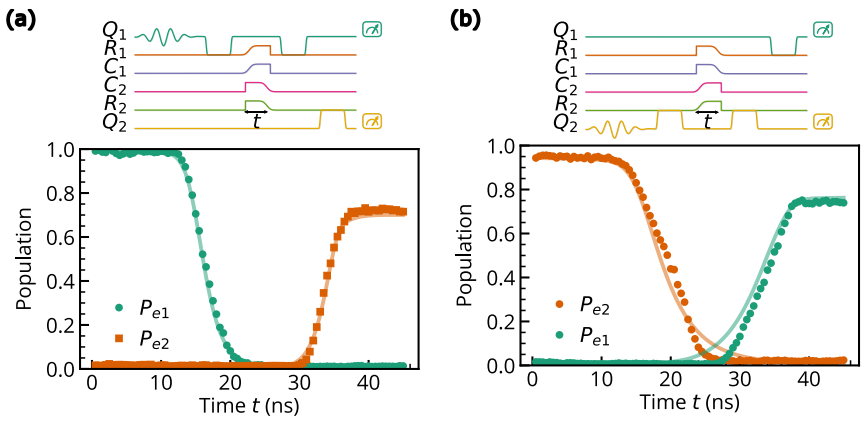

Figure 5.18: **Single excitation transfer.** **(a)** Transfer excitation from node 1 to node 2 with shaped release and catch, varying the transfer time t. Fit to data using input-output simulation with skewed hyperbolic secant wavepacket shape. We fit a skew $\theta = 0.57$, indicating the pulse is not symmetric (symmetric pulse has $\theta = 0$)**(b)** Transfer excitation from node 2 to node 1. Fit $\theta = 0.37$, although this wavepacket shape does not fit well to the data.

initial single excitation in the releasing resonator. This optimization for wavepacket release and capture is done independently for both transfer directions. The optimized transfers are shown in Fig. 5.18.

In order to fit the release and capture in Fig. 5.18 with input-output theory with wavepackets as discussed in section 2.4.2, the model requires specifying both the normalized wavepacket shapes $u(t)$ and $v(t)$ as well as the resonator emission rate γ as a function of time. For the wavepacket shape we can choose to use the skewed hyperbolic secant function from Eq. 5.3. While this function does not have a physical origin it is useful for characterizing the pulse symmetry. To derive the form of the coupling function from this wavepacket shape we can use input-output theory. In the absence of internal loss and decoherence, a resonator coupled to a waveguide will evolve following [59]

$$\dot{a} = -i\Delta\omega a - \frac{\gamma}{2}a - \sqrt{\gamma(t)}b_{\text{in}}(t), \tag{5.4}$$

$$\sqrt{\gamma(t)}(t) = b_{\text{out}}(t) - b_{\text{in}}(t), \tag{5.5}$$

where a is the resonator operator, $\Delta\omega$ is the detuning from the resonator frequency, b_{in} is the input field and b_{out} is the output field. Taking the average of these quantities[5] we numerically fit the release and capture average population. Note that in the case of no input field ($b_{\text{in}} = 0$) the average resonator occupation probability $\langle P_r \rangle = \langle a \rangle^2$ can be solved and shown to have the simple form $\langle P_r \rangle = \int \langle b_{\text{out}} \rangle^2 + \langle P_0 \rangle$, where $\langle P_0 \rangle$ is the initial average resonator population. We then use $\gamma(t)$ extracted from these fits with the more complete quantum input-output theory model (section 2.4.2) for the fits shown in Fig. 5.18.

The extracted skew θ for the node 1 release is $\theta = 0.57$, indicating the released wavepacket is not time-symmetric. This implies that our pulse shaping resulting from the optimization process is not ideal and may limit our transfer efficiency. Similarly $\theta = 0.37$ for the node 2 release, however the skewed hyperbolic secant does not fit as well to the data.

5.3.3 Discussion of limited population transfer

The highest population transfer for a single excitation we achieve is 0.74. This is lower than the unity transfer efficiency expected from the simulations discussed in Sec. 5.1.2. There are several assumptions in the model that may prevent us from achieving the high transfer shown in simulation. First, we may have loss in various components. Second, we may not be able to control the coupling strength quickly enough to release and capture the wavepacket in the required experiment time. Third, the quantum model assumes that the resonator frequency remains constant, something we may not be able to fully achieve in experiment. Finally, the model does not include nonlinear effects in the coupler or resonator which may be significant at higher photon numbers. We can discuss these in order.

The loss in the system is fully characterized by measuring the lifetimes of all the components as shown in Tables 5.2 and 5.3. While the resonators do have higher loss than anticipated, decay in the components does not fully explain the population loss in the single excitation transfer experiment.

5. effectively treating them as classical variables

The control of the coupling strength is limited by pulse generation, filtering, and the limitations of the coupler itself. The DAC controlling the coupler has a clock cycle of 1 GHz, however in practice we can only generate signals up to a few hundred MHz. The DAC also produces higher harmonics of the clock cycle, which need to be filtered out by Gaussian filters. These filters limit the time resolution of the output pulses to a few ns($\approx$ 3 ns). Considering that the back-of-the-envelope calculation in Sec. 5.1.1 estimates that we need to release a pulse under $\sim$ 10 ns, we do not have much time to shape the pulse. This limited shaping ability is not necessarily a fundamental limitation for our experiment. A similar device from our group without tunable resonators that achieved over 90% single photon transfer efficiency where the generated pulse shape was a simple Gaussian convolved with a rectangle [44]. This high transfer efficiency is surprising considering the pulse distortion due to the filters, as well as the fact that the transfer function of the coupler from flux to coupling strength is nonlinear.

Shaping the coupling strength for wavepacket capture becomes more challenging if dispersion in the waveguide distorts the pulse shape. This dispersion might be caused by lumped element capacitances (see Sec. 5.2.5 for example) or other variations in waveguide impedance variations.

It is also possible that the coupler's circuit parameters are different from the design parameters, leading to a lower maximum coupling strength. As noted in Sec. 5.1.1, the Josephson junction fabrication process can lead to junctions that are different from the designed value. Junctions that are too large lower the maximum coupling strength of the coupler. Junctions that are too small may put the coupler into a hysteretic regime, also lowering the maximum coupling strength ([17],Fig. 3.2). Ref. [18] notes that it is also easy to overlook extra linear inductance in the coupler circuit, which may also put the coupler into the hysteretic regime.

To keep the resonator frequency constant while releasing the wavepacket we need to tune the resonator dynamically while shaping the coupling strength. Controlling the frequency of

the resonator quickly is difficult due to limited pulse control in time already mentioned for the coupler. There is an additional complication in that the transfer function from flux to resonator frequency is different than that of the coupler, and so may not cancel out in time together. Although these frequency control issues may not be critical to high fidelity release and capture because the resonator bandwidth becomes large at strong coupling.

Finally, both the resonator and coupler are to a good approximation linear at low photon number (see Sec. 2.3.6 and [47] respectively) and so their small nonlinearity should not affect transfer efficiency for single photon transfers. However it should be noted that some corrections to the Hamiltonian may be required at higher photon numbers.

5.3.4 Wigner tomography

Up until now we have been reading out the resonator state by swapping the single excitation state into the qubit. For multi-photon states we need to do tomography on the resonator that will let us reconstruct the full state of the resonator.

The Wigner function $W(\alpha)$ is a quasiprobability distribution for a resonator's quantum state which can be calculated from the density matrix ρ [132]

$$W(\alpha) = \frac{2}{\pi}\mathrm{Tr}\left[D(-\alpha)\rho D(\alpha)\mathcal{P}\right], \tag{5.6}$$

where Tr is the trace, $D(-\alpha) = D^{\dagger}(\alpha) = \exp(\alpha^* a - \alpha a^{\dagger})$ is the displacement operator for the resonator, $\mathcal{P}$ is the resonator's photon number parity, and $\alpha = x + ip$ is the complex phase space coordinate. x and p are the resonator's position and momentum variables respectively. Applying the displacement operator on the resonator ground state $|0\rangle$ creates coherent states $|\alpha\rangle$. $|\alpha\rangle$ is an eigenstate of $\hat{a}$ so that $\hat{a}|\alpha\rangle = \alpha$. The average number of photons in a coherent state n_α can then be calculated as $n_\alpha = \langle\alpha|\hat{a}^{\dagger}\hat{a}|\alpha\rangle = |\alpha|^2$. Note that $|0\rangle$ itself is a coherent state with $\alpha = 0$.

$W(\alpha)$ is bounded between $-2/\pi$ and $2/\pi$ and has the property where quasi-classical

states such as the coherent or squeezed coherent states[6] are positive everywhere. For these states the Wigner function can be thought of as a probability distribution of classical field fluctuations. Fock (resonator number states) have values for α such that $W(\alpha) < 0$, and so their Wigner functions cannot be thought of as a straightforward probability distribution. For this reason, negative values in Wigner functions are a sign of a non-classical state.

Experimentally, α is also the coherent displacement of the resonator with $-\alpha = (\frac{1}{2}) \int \Omega_r(t) dt$, where Ω_r is a complex drive amplitude [124]. And so we can rewrite Eq. 5.6 as $W(\alpha) = \frac{2}{\pi} \langle \mathcal{P} \rangle_\alpha$. In words, the Wigner function at coordinate α is equal to the photon parity of the resonator displaced by α. This makes the Wigner function straightforward to calculate as long as we can displace the resonator and have a method for measuring its parity.

Displacing the resonator can be done by capacitively coupling a signal line to the resonator. Measuring the parity using an ancilla qubit can be done with several techniques with the qubit and resonator either dispersively coupled [133, 134, 135] or on resonance [124, 125, 122]. In this work we will use the resonant technique, in which we first measure the full Fock state probability distribution (up to some maximum photon number) as shown in Fig. 5.19 and then calculate the parity from that distribution.

If the resonator is prepared in a well-defined Fock state, then a qubit prepared in the ground state will go through Rabi oscillations with a period of $\tau_0/\sqrt{n}$, where τ_0 is the period for a single excitation. If the resonator is prepared with a superposition of Fock states, the qubit will oscillate following a linear combination of these oscillations proportional to their associated resonator populations.

To reconstruct the density matrix from the Wigner function we use a MATLAB package [136] that uses convex optimization to find the most likely ρ given the measured photon number distributions as a function of displacement [137]. During this reconstruction procedure we constrain ρ to be Hermitian, positive semi-definite, and have a trace equal to 1.

6. A squeezed coherent state is a coherent state that is stretched along one axis and compressed along the other. JPAs operating in phase sensitive operation mode can generate these states [82]

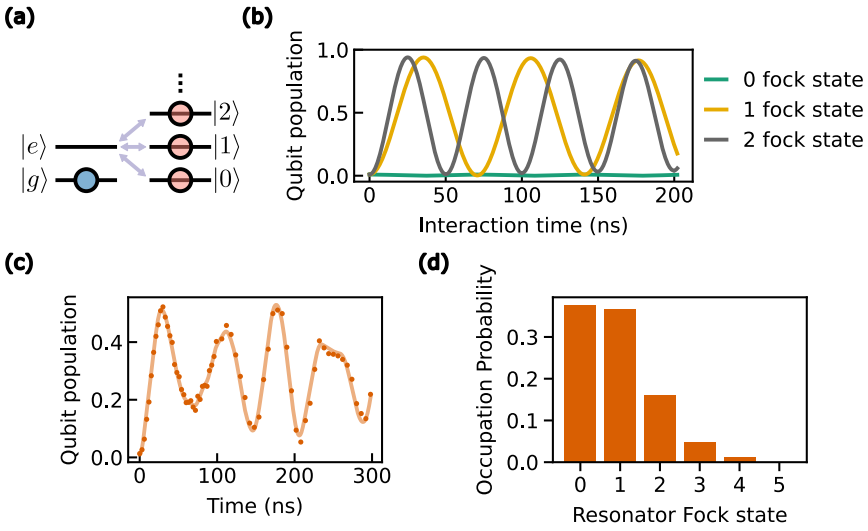

Figure 5.19: **Resonator Fock distribution reconstruction.** **(a)** A resonator with unknown state couples to a qubit prepared in the ground state **(b)** Simulation for qubit/resonator oscillations with the resonator prepared in single Fock states. The qubit oscillates $\tau_0/\sqrt{n}$, where τ_0 is the period for a single excitation **(c)** For an arbitrary resonator state, the qubit population over time is the linear combination of the oscillations that would occur for each prepared Fock state as in (b). Data (points) and fit to model (line) are shown **(c)** Resonator occupation probability distribution from fitting the data in (c). We see that the resonator has a Fock distribution consistent with a coherent state with $\alpha \approx 1$.

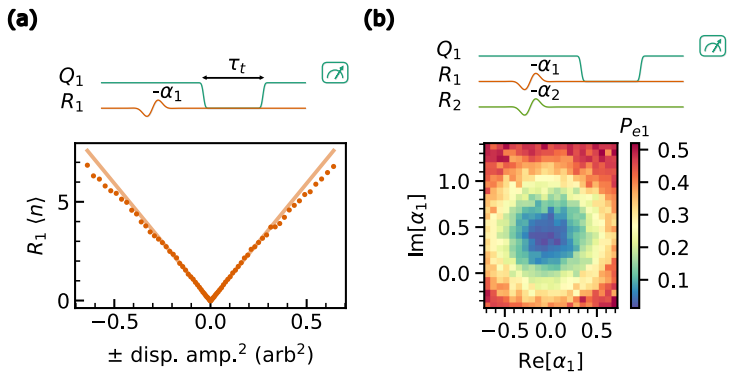

Figure 5.20: **Displacement calibration and microwave crosstalk.** **(a)** Calibration measurement for α. We displace the resonator by different amounts and then interact the resonator with the qubit for a variable amount of time. Fitting the time trace with a qubit/resonator model returns a linear relationship at low photon powers with the square of the displacement amplitude. The linear fit here is up to 0.4 displacement amplitude which roughly corresponds to $n \approx 1.9$. **(b)** Microwave crosstalk node 2 on node 1. We apply a constant displacement pulse $\min \alpha_2$ with R_2's displacement line that would correspond to a photon population in R_2 of $\langle n_2 \rangle \approx 2.7$. At the same time we apply a displacement α_1 on resonator 1, and then swap the resulting population into Q_1 at the 1 photon swap time $\tau_0 = 38\,\mathrm{ns}$. When α_1 cancels the crosstalk from the displacement from node 2 we measure 0 population in Q_1.

5.3.5 Microwave displacement calibration and crosstalk

Using the resonant photon state reconstruction technique from section 5.3.4 we can calibrate the resonator displacement pulses. Fig. 5.20a shows the average photon number after applying a 20 ns displacement pulse and fitting the qubit/resonator interaction. Displacement amplitude $\propto V$ (proportional to V), and since the photon number $n \propto V^2$, $n \propto$ the square of the displacement amplitude. This relationship is true at low photon numbers, however at high photon numbers the linear relationship deviates, possibly due to either resonator nonlinearity or photon number fitting errors. For a coherent state $\langle n_\alpha \rangle = |\alpha|^2$, so the slope of this line gives the calibration factor between α and the displacement amplitude, in the case of Fig. 5.20a, the slope is 3.44.

Microwave crosstalk occurs when we want to only apply a microwave tone to one component but affect other components as well. This may occur because of unintended coupling in either the microwave lines or sample packaging. In our system the two qubits are detuned

from each other by tens of MHz so that microwave crosstalk between the two is minimal. This can be confirmed by separately exciting the two qubits and jointly measuring them to monitor the ground state populations. The tunable resonators are detuned from the qubits by several hundred MHz when applying microwave pulses, and so have negligible microwave crosstalk between the two. However, the tunable resonators are at the same frequency, and so there is non-negligible crosstalk between them. When we apply a microwave pulse to displace resonator 1 with amplitude a_1 and phase θ_1, we also displace resonator 2 with amplitude a_{12} and phase θ_{12}. Similarly there is crosstalk in the other direction. The microwave crosstalk between resonators would experimentally be a problem when we need to simultaneously measure the state of both resonators, as in the NOON state experiment in section 5.3.8.

To measure this crosstalk we can do a similar procedure that we use for calibrating displacement amplitude to resonator α for a single resonator: Wigner tomography with the resonator prepared in the ground state, and scanning the displacement amplitude. However, instead of displacing the resonator using its own displacement line, we use the microwave crosstalk from the other resonator displacement line. We can also measure the phase of this crosstalk relative to the 0 phase for each resonator, by applying displacements from both displacement lines and measuring at which phase the two tones cancel each other as in Fig. 5.20b. This crosstalk is quite large, when applying a displacement pulse -α_2 to populate resonator 2 with 1 photon we also populate resonator 1 with 0.07 photons. Instead of actively canceling this crosstalk during measurement, we correct for it when processing the data.

5.3.6 Superposition transfer

Fig. 5.21 shows prepared and received transfer of superposition states from node 1 to node2 with Wigner plots. Defining the state fidelity between two states ρ and σ as $F(\rho,\sigma) = \mathrm{tr}\sqrt{\rho^{1/2}\sigma\rho^{1/2}}$ [138](tr is the trace), we can prepare a $|0\rangle + |1\rangle$ state in R_1 with 0.996 fidelity compared to the ideal state. After the transfer the state fidelity goes down to 0.94. The

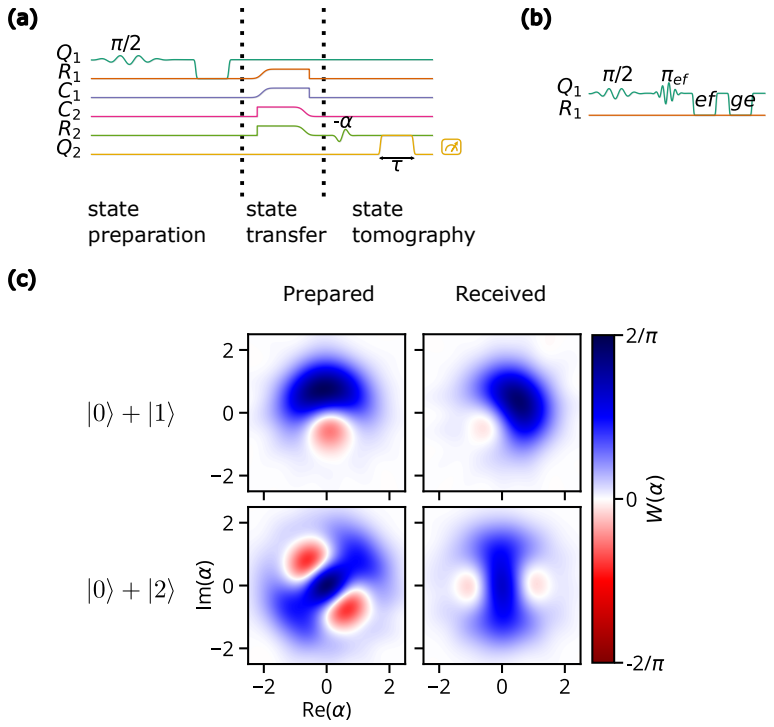

Figure 5.21: **Superposition state transfer and tomography.** **(a)** Pulse sequence for the preparation and transfer of a $|0\rangle + |1\rangle$ state. After a $\pi/2$ pulse prepares a $|g\rangle + |e\rangle$ state in Q_1, the excitation is swapped to R_1, transferred as a wavepacket to R_2 with shaped release and capture pulses, then finally displaced and measured with Wigner tomography (See section 5.3.4). **(b)** State preparation pulse sequence for the $|0\rangle + |2\rangle$ state in R_1. **(c)** Wigner plots for prepared and received $|0\rangle + |1\rangle$ and $|0\rangle\rangle + |2\rangle\rangle$ states. Although there is visible loss during the state transfer, the superposition states maintain some negativity.

fidelity of the $|0\rangle + |1\rangle$ is higher than the $|1\rangle$ state transfer because the $|0\rangle$ state can be transferred from one node to the other with nearly unit fidelity. The $|0\rangle + |2\rangle$ state in R_1 can be prepared 0.952 fidelity compared to the ideal state, and after the transfer the state fidelity goes down to 0.823. After the state transfer both superposition states maintain some (small) negativity.

5.3.7 Resonator state swaps

With our device we can not only send state bidirectionally, but we can do this state transfer simultaneously. Fig. 5.22 shows resonator 1 prepared with a 2 photon state while resonator 2 is prepared with a 1 photon state. Furthermore, we can track the resonator Fock population

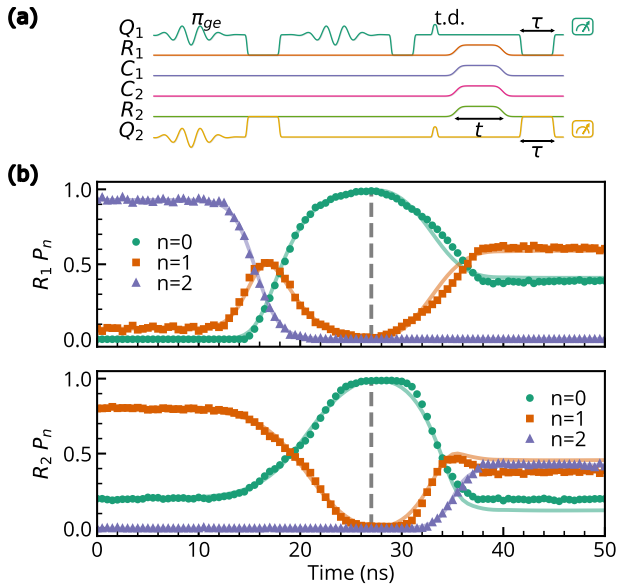

Figure 5.22: **Multi-photon remote state swap** A 2 photon state is prepared in R_1 and a 1 photon state is prepared in R_2. A thermal dump t.d. resets the qubits to their respective ground states before resonantly interacting with the resonators resonantly for variable time τ to reconstruct the resonator photon distributions. The plot shows R_1 photon population (top) and R_2 photon population (bottom) as a function of the delay t for the same jointly measured process. Both resonators simultaneously release their states and simultaneously capture the states traveling in the waveguide. Fit to data with input-output simulation assuming hyperbolic secant wavepacket shape. Dotted lines indicate time in simulation where we stop/start the the release/capture fits respectively. While the release from both resonators is well described by this wavepacket shape, the capture does not match as well to the model, possibly indicating insufficient shaping control.

as a function of time during this process and see that the states of the two resonators have swapped. Input-output simulation fits to the data indicate that we are able to emit into a hyperbolic secant wavepacket with high efficiency, however the capture is not well described by the same simulation.

5.3.8 NOON states

NOON states [139, 140, 125] are superposition states involving two resonators where N excitations are either in one or the other resonator

$$|\Psi\rangle = \frac{1}{\sqrt{2}} \left(|N0\rangle + |0N\rangle \right), \tag{5.7}$$

where the labels represent the number of photons in resonator 1 and 2 respectively. To create an N=1 state in the resonators we transfer the excited population from one qubit into its resonator, then release half of the state to the waveguide and fully capture the received pulse in the other resonator. Fig. 5.23a shows the reconstructed N=1 NOON state with 0.83 state fidelity compared to the ideal state, demonstrating entanglement between the two resonators.

Measuring the joint resonator state involves bipartite Wigner tomography (See supplementary information in [125]). We follow the protocol described in [125]:After preparing the resonator state, each resonator is displaced by a constant amplitude and variable phase θ_1 and θ_2 . A set of M displacement phases[7] $\theta_1, \theta_2 \in \{\theta_a, \theta_b, ...\}$ are chosen such that displacements are equidistant around a circle in phase space of a single resonator. Then we permute every combination of θ_1 and θ_2, resonantly interact the ancilla qubits with their respective resonators for some variable time, and then measure the joint qubit evolution. Similarly to single resonator tomography, the joint qubit time evolution traces can then be fit with a model of the system to reconstruct the joint resonator population distribution.

We then use convex optimization [136] to reconstruct the most likely density matrix associated with the measured data. As before, during this reconstruction procedure we constrain ρ to be Hermitian, positive semi-definite, and have a trace equal to 1. We additionally constrain the reconstructed density matrices to be 0 for N greater than the prepared NOON state [125].

For higher order N, we can use the more general protocol in [125] to prepare the NOON states. First we create a Bell state $(|eg\rangle + |ge\rangle)$ between the two qubits. We can then excite the two qubits to their respective $|f\rangle$ state to make $|fg\rangle + |gf\rangle$. Then we swap the $|f\rangle$ state excitation into each resonator repeating the process for higher N states if desired and completing the process by swapping the $|e\rangle$ state into the resonators. In Fig. 5.23b an N=2 NOON state is created with this protocol with state fidelity 0.78. For the N=2 state we

7. For the N=1 NOON state, M=6 and $|\alpha_1| = 0.35$, $|\alpha_2| = 0.33$

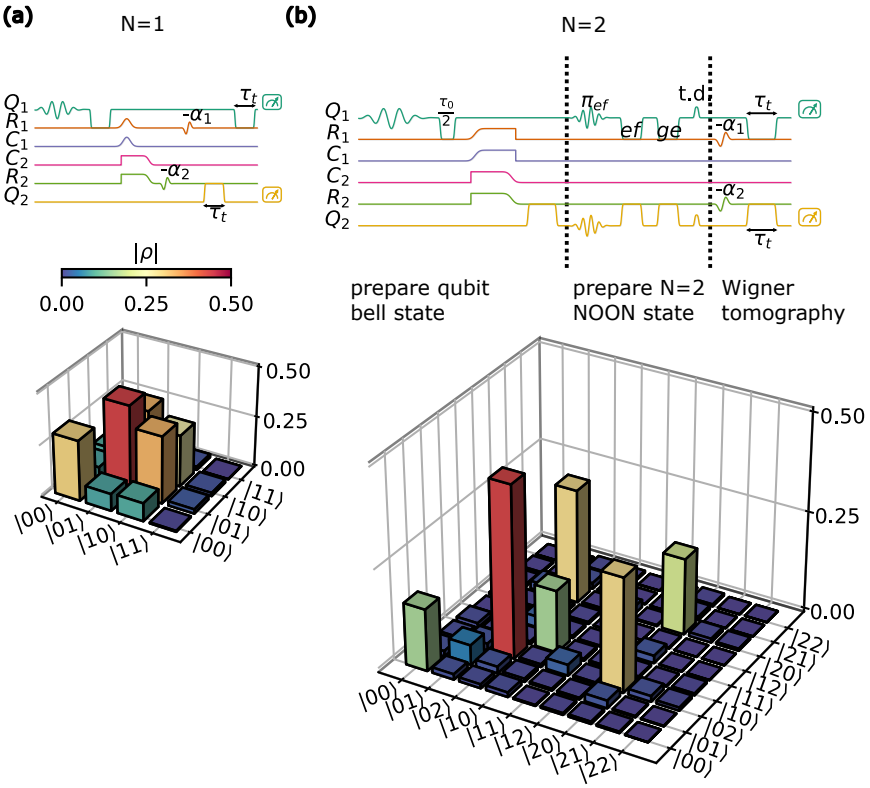

Figure 5.23: **Resonator NOON states.** **(a)** N=1 NOON state. The state is prepared by exciting Q_1, swapping the excitation into R_1, then releasing half of the resonator's population. This population is then caught by R_2. Both resonators are then displaced in sequence by amplitude $-\alpha_1$ and $-\alpha_2$, interact with their respective qubit for the same variable time τ_t, and finally a joint measurement on both qubits. **(b)** N=2 NOON state. In contrast to the protocol in (a), the bell state for (b) is made by interacting R_1 with Q_1 for only half the swap time τ_0. the excitation is then transferred as a wavepacket to R_1 and then swapped to Q_2. To make the resonator NOON state, both qubits are excited to their f level (with ground populations remaining in $|g\rangle$) and then both excitations are swapped to the resonators. A thermal dump t.d. resets the qubits of any residual population before Wigner tomography with simultaneous displacements and qubit/resonator interactions.

permute through M=20 unique phases for each resonator, $|\alpha_1| = 0.7$, and $|\alpha_2| = 0.66$.

We have demonstrated here a variety of protocols using this quantum communication testbed. These protocols demonstrate the flexibility of this platform, as well as the potential for using such a testbed for transmitting complex multi-photon states. While there is room to improve the transfer efficiencies, we show that it is possible to bidirectionally transfer multi-photon states between remote superconducting resonators using shaped wavepackets and to entangle those resonators with multi-photon states. Further work may enable more efficient transfers and a variety of new applications as discussed in chapter 6.

CHAPTER 6

CONCLUSION

6.1 Summary

In this thesis we have introduced two classes of devices that may be useful for the development of quantum technologies. We first demonstrated a near-quantum limited amplifier with broad bandwidth with a power gain above 20 dB over 300 MHz at microwave frequencies. An impedance transformer circuit was integrated with a lumped element JPA on chip, in a design that is simple enough for researchers to fabricate in an academic cleanroom. We showed that this amplifier can operate in a flux-pumped mode of operation using an on-chip flux line, improving on a design with a similar impedance transformer [98] by separating the pump from the signal both physically and in frequency. This may enable more researchers to perform low-noise microwave measurements on a variety of systems.

The second project demonstrated a quantum communication testbed at microwave frequencies that can transfer multi-photon states in both directions of a single communication channel between remote resonators. Using frequency tunable ancilla qubits, we prepared both Fock and superposition states in a resonator and then transferred the states to the other node using shaped wavepackets. We showed that we can simultaneously transfer states in both directions of the waveguide. NOON states were prepared, demonstrating multi-photon entanglement between the remote resonators.

6.2 Outlook

There are a number of research directions to both improve the communication testbed we have demonstrated, as well as to more fully utilize its capabilities. Transfer efficiency was likely limited in our experiment by insufficient pulse control, which may be improved by faster electronics, fewer filters along the control wiring, and a longer waveguide to increase

the time available to shape the pulse. Low resonator lifetimes limited the complexity of the prepared multi-photon resonator states, we can both improve the fabrication of these resonators and increase the qubit/resonator coupling to more quickly prepare various states. We might additionally improve transfer efficiencies by reducing defects in the waveguide that might cause dispersion on the wavepacket, or by fabricating tunable couplers that have parameters farther from their hysteretic operating regime.

Our system architecture is open to a wide variety of possible experiments due to the ability to dynamically vary many of the experimental parameters. Both the qubits and resonators are frequency tunable, and the coupling strength to the waveguide is tunable, and so it may be possible to simulate a wide variety of multi-photon communication protocols that rely on time-varying parameters. For example, while in this thesis we constrain the resonators to emit at a single frequency, it is possible to dynamically vary the resonator frequency during the processes. More complex resonator states may be prepared and transmitted, and error correction schemes with multi-photon states might be tested as in Ref. [111]. We could also treat the waveguide as a multi-mode resonator when weakly coupled to the resonators and test implementations for quantum random access memory as in Ref. [141].

APPENDIX A

AMPLIFIER NOISE

A.1 Noise added by amplifiers in series

The power gain of a linear amplifier refers to the amount the signal is amplified[1]. We can define the input mode as $\hat{a}_{\text{in}}$ with commutation relation $\left[\hat{a}_{\text{in}}, \hat{a}_{\text{in}}^{\dagger}\right] = 1$ and a linear power gain G. Naively, we might define the output mode by multiplying the amplitude gain $\sqrt{G}$ by $\hat{a}_{\text{in}}$, however would not result in the correct commutation relations for the output mode. Ref. [71] found that for amplifiers that amplify both phase quadratures equally[2], in the high gain limit the amplifier must add at least half the zero-point fluctuations. To satisfy the quantum commutation relations we introduce a second mode $\hat{b}_{\text{in}}$ with $\left[\hat{b}_{\text{in}}, \hat{b}_{\text{in}}^{\dagger}\right] = 1$ and $\left[\hat{b}_{\text{in}}, \hat{a}_{\text{in}}^{\dagger}\right] = 0$ so that

$$\hat{a}_{\text{out}} = \sqrt{G}\hat{a}_{\text{in}} + \sqrt{G-1}\hat{b}_{\text{in}}. \tag{A.1}$$

$\hat{b}_{\text{in}}$ is known as the idler mode, but can also be thought as a mode that introduces additional noise into the amplified signal. One way of measuring how much noise (usually not desired) to signal (desired) we have is the signal-to-noise ratio (SNR) $SNR = \frac{GS}{N}$ where N is the noise power at the output and S is the signal power at the input. Assuming there are no cross-correlations between the noise in the signal and idler mode the output noise from an amplifier[3] can written in power as

$$N_{\text{out}} = GN_a + |G-1|\, N_b, \tag{A.2}$$

1. This section is adapted from notes written by Audrey Bienfait

2. Known as linear non-degenerate amplifiers or phase-preserving amplifiers.

3. In the following section we will remove the absolute value expression with either $G-1$ or $1-G$ depending if $G > 1$ or $G < 1$ respectively

where N_a and N_b are noise powers at the input of the amplifier. We can now calculate the SNR for two amplifiers in series with gain G_1, G_2 that add noise N_1, N_2 with some additional noise at the input of the first amplifier N_L (L for load).

The total gain G_T and total noise N_T is

$$G_T = G_1 G_2 \tag{A.3}$$

$$N_T = G_2 \left(G_1 N_L + (G_1 - 1) N_1\right) + (G_2 - 1) N_2 \tag{A.4}$$

The SNR is

$$SNR = \frac{G_1 G_2 S}{G_2 \left(G_1 N_L + (G_1 - 1) N_1\right) + (G_2 - 1) N_2} \tag{A.5}$$

$$= \frac{S}{N_L + \left(1 - \frac{1}{G_1}\right) N_1 + \left(\frac{1}{G_1} - \frac{1}{G_1 G_2}\right) N_2} \tag{A.6}$$

$$\approx \frac{S}{N_L + N_1} \tag{A.7}$$

Where in the last line we assume $G_1 \gg 1$ and $G_2 \gg 1$. This shows that for a chain of amplifiers, if the gain of the first amplifier is large enough we can effectively neglect the noise contribution from subsequent stages. A gain of 20 dB for G_1 means we reduce the following stage's contribution to the SNR by approximately a factor of 100.

See Appendix 4.1.5 for how to roughly estimate the noise added by an amplifier using an SNR measurement.

A.2 JPA noise Model

The method will measure how the signal to noise ratio (SNR) at the measurement chain output improves when we turn on the JPA pump compared to when the pump is off[4]. As

4. The derivation for the JPA noise is adapted from notes written by Audrey Bienfait

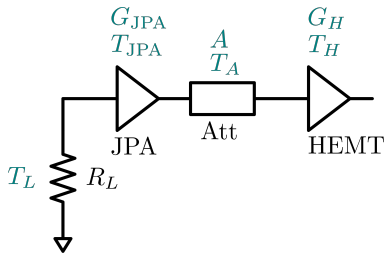

Figure A.1: **JPA noise model.** Noise model for amplifier chain. See text for variable definitions.

shown in Fig. A.1 we will model the system as two amplifiers connected in series, with some attenuation in between them and a load resistor on the input. See Appendix A.1 for a short introduction on how quantum noise propagates in a chain of devices connected in series. A load resister with resistance R_L at physical temperature T_L sends noise to the input of the JPA with gain G_{JPA} and noise temperature T_{JPA}. Connected in series to the JPA is an attenuator with attenuation A at a physical temperature T_A and finally the HEMT amplifier with gain G_H and noise temperature T_H. Some key assumptions for this model include

1. the JPA has unity gain when off, $G_{\text{JPA, off}} = 1$
2. the JPA gain is much larger than 1 when on, $G_{\text{JPA, on}} \gg 1$
3. the HEMT gain is much larger than 1, $G_{\text{H, on}} \gg 1$

The total gain G_C of the chain is

$$G_C = G_{\text{JPA}} A G_H. \tag{A.8}$$

While the total noise N_C at the output of the chain is

$$N_C = G_H[A[G_{\text{JPA}} N_L + (G_{\text{JPA}} - 1)N_{\text{JPA}}] + (1 - A)N_A] + (G_H - 1)N_H, \tag{A.9}$$

where the noise powers $N_L, N_{\mathrm{JPA}},$ and N_H are related to their respective temperatures T_i by $N_i = k_B B T_i$, with k_B the Boltzmann constant and B the measurement bandwidth. The SNR when the JPA is on is given by

$$\mathrm{SNR}_{\mathrm{on}} = \frac{G_C S}{N_C} = \frac{G_{\mathrm{JPA}} A G_H}{G_H[A[G_{\mathrm{JPA}} N_L + (G_{\mathrm{JPA}} - 1)N_{\mathrm{JPA}}] + (1-A)N_A] + (G_H - 1)N_H}. \tag{A.10}$$

Using our first assumption, when the JPA is off, $G_{\mathrm{JPA,\ off}} = 1$, and so when the JPA is off we have

$$\mathrm{SNR}_{\mathrm{off}} = \frac{A G_H}{G_H[A N_L + (1-A)N_A] + (G_H - 1)N_H}. \tag{A.11}$$

We can now introduce a variable $r = \frac{\mathrm{SNR}_{\mathrm{on}}}{\mathrm{SNR}_{\mathrm{off}}}$ which we are able to calculate from experimental data. Solving for N_{JPA} in terms of r (using Wolfram Mathematica), simplifying the resulting expression assuming $G_{\mathrm{JPA}} \gg 1$ and $G_{\mathrm{H}} \gg 1$, and sorting terms by noise source we get

$$N_{\mathrm{JPA}} = N_A\left(\frac{1}{G_{\mathrm{JPA}}} - \frac{1}{r} - \frac{1}{A G_{\mathrm{JPA}}} + \frac{1}{Ar}\right) + N_H\left(\frac{1}{Ar} - \frac{1}{A G_{\mathrm{JPA}}}\right) + N_L\left(\frac{1}{r} - 1\right). \tag{A.12}$$

We will redefine N_{JPA} to include the noise power from the load N_L

$$N_{\mathrm{JPA}} = N_A\left(\frac{1}{G_{\mathrm{JPA}}} - \frac{1}{r} - \frac{1}{A G_{\mathrm{JPA}}} + \frac{1}{Ar}\right) + N_H\left(\frac{1}{Ar} - \frac{1}{A G_{\mathrm{JPA}}}\right). \tag{A.13}$$

Finally, we divide the expression by $k_B B$ to get the JPA noise temperature

$$T_{\mathrm{JPA}} = T_A\left(\frac{1}{G_{\mathrm{JPA}}} - \frac{1}{r} - \frac{1}{A G_{\mathrm{JPA}}} + \frac{1}{Ar}\right) + T_H\left(\frac{1}{Ar} - \frac{1}{A G_{\mathrm{JPA}}}\right). \tag{A.14}$$

It's worth checking that the limits of this expression makes sense. If there is no attenuation, $A = 1 = 0\,\mathrm{dB}$, then the T_A term disappears as expected. If both $A = 1$ and $r = 1$, we get an estimated noise temperature near T_H. Finally, the attenuation is a value between 0 and 1 and always appears in the denominator so increases the estimated JPA noise. If we were to ignore this attenuation term, it would appear that our JPA is performing better than it

actually is.

APPENDIX B

FABRICATION

For any process in the cleanroom, intuitive justifications for a specific procedure can have weak experimental evidence behind them. For this reason we many times joke that whenever we have possible explanations for process steps that are based on intuition they are part of a "cleanroom theory". As our field matures, rigorous experiments will eventually prove or disprove these theories, however the unfortunate present reality is that fabrication is complicated and there is not enough time in a researcher's day to explore the correctness of each and every procedure in a given fabrication process. Although getting a given fabrication process to work may be difficult due to this complexity, if followed precisely, procedures tend to be reproducible. Because a specific procedure can be justified due to working devices, while individual steps in the process cannot, these motivations for steps are passed down as oral tradition within groups while the steps are recorded in writing.

This appendix chapter will have two goals. First, it will attempt to explore the steps of developing a JPA process from a new cleanroom and describe the troubleshooting process for achieving a working device, which in reality is a more complicated journey than the streamlined version typically presented in papers. Second, it will include the motivations behind the cleanroom recipe to show a fuller picture of this process than is typically recorded in the literature. Some (many?) of the cleanroom theories will likely turn out to be incorrect but it may be useful for future students to have some of these stated motivations written down. Although some care was put into making these descriptions and tips as accurate as possible it should be emphasized that this section will be less rigorous than other parts of this thesis.

Finally, our lab shares recipes for many of our projects and these are generally written down in detail in various theses from our group. For additional perspectives on similar fabrication recipes see [17, 18, 142, 143]

B.1 JPA fabrication

B.1.1 Recipe

These are the fabrication steps for the JPAs presented in chapter 4 for those who just want the recipe without additional discussion (Starting in Sec. B.1.2). Repeated steps (solvent clean, photolithography, etc.)are placed in sub-bullets with variations noted in process name:

- Start with a high resistivity (10 kΩ) Si wafer, 4 inch

Base Al layer

- Solvent clean
  - Sonicate in Acetone, 5 min
  - Sonicate in IPA, 5 min
  - Dry with Nitrogen (N_2) spray gun
  - Apply DI water from spray gun, 20 s
  - Dry with N_2 spray gun
- Hot plate, 200 °C, 10 min
- E-beam evaporation, Al, 100 nm, 2 Å/s, 50 mm deposition height, 5 rpm
- Solvent clean
- Hot plate, 115 °C
- Photolithography for base Al layer, Heidelberg Direct Write Lithographer 170 MJ/cm^2, AZ 1:1 developer for 3 min
  - Place wafer on spinner
  - Apply AZ MiR 703 photoresist using plastic transfer pipette
  - Spin, 4500 rpm, 500 rpm/s acceleration, 30 s
  - Hot plate 90 °C, 60 s
  - Expose with Heidelberg with 375 nm light
  - Hot plate 115 °C, 60 s
  - Develop with photoresist developer while gently agitating
  - DI water bath, 30 s

- Dry with N_2 spray gun

- Al etch in Chlorine (Cl) Reactive Ion Etcher (RIE)
  - With dummy wafer[1], 5 min O_2 clean in Cl RIE etch tool
  - With dummy wafer, 3 min Cl etch in Cl RIE etch tool
    - 5 mTorr, 33 W Bias, 400 W Inductively Coupled Plasma (ICP), 30 sccm Cl_2, 30 sccm BCl_3, 10 sccm Ar
  - With sample wafer, 24 s Cl etch in Cl RIE etch tool
  - Immediately after etch, immerse wafer in DI water for 10 min

- Photoresist strip for etch process
  - Preheat N-methyl-2-pyrrolidone (NMP), 10 min, covered, on hot plate
  - Downstream O_2 clean #7
    - 180 s, 70 °C, 350 W, 120 sccm O_2
  - Sonicate in NMP, 20 min total, varying 40 kHz-170 kHz sonication frequencies at medium power
  - Remove from NMP, squirt with IPA with bottle, 30 s
  - 2 IPA baths , 5 min each
  - DI water bath, 1 min
  - rinse wafer from DI water faucet, 30 s
  - Dry with N_2 spray gun

Dielectric layer

- Amorphous silicon (a-Si) deposition, High Density Plasma Chemical Vapor Deposition (HDPCVD)
  - 90 °C, with wafer in chamber
  - Predeposition mill, 30 s, 7 mTorr,50 W Bias, 600 W Run ICP,10 sccm Ar (gas ring), 10 sccm Ar
  - Thin SiN_x deposition
    - 10 s, 1 W Bias, 100 W Run ICP , 10 mTorr, 25 sccm SiH_4 (gas ring), 10 sccm Ar (gas ring), 30 sccm N_2
  - Thick a-Si deposition, 3 min, 1 W Bias, 1200 W Run ICP, 3 mTorr, 15 sccm SiH_4 (gas ring), 10 sccm Ar (gas ring), 10 sccm Ar
  - Thin SiN_x deposition

- Solvent clean

1. Cheap low resistivity silicon wafer used for quick tests and preconditioning RIE chambers

- Hot plate, 115 °C, 5 min
- Photolithography for dielectric layer, Heidelberg 160 mJ/cm^2, AZ 300 MiF developer for 1 min
- a-Si etch in Fluorine RIE
  - With dummy wafer, 5 min O_2 clean in Fluorine RIE etch tool
  - With dummy wafer, 3 min Fluorine etch in Fluorine RIE etch tool
    - 50 mTorr, 50 W Bias, 400 W Run ICP, 20 °C temperature, 50 sccm CF_4, 5 sccm O_2, 10 sccm Ar
  - With sample wafer, 6 min Fluorine etch in Fluorine RIE etch tool
- Photoresist strip for etch process
- Measure dielectric thickness with profilometer

Gold layer

- Photolithography for gold layer, Heidelberg 160 mJ/cm^2, AZ 300 MiF developer for 1 min
- Downstream O_2 clean #1
  - 25 s, 22 °C, 200 W, 50 sccm O_2
- E-beam evaporation, 10 nm Ti, 1 Å/s, then 150 nm Au, 2 Å/s, no rotation
- Photoresist strip for liftoff, 3 h in NMP heated water bath
  - Preheat NMP, 10 min, covered, on hot plate
  - Place sample in NMP, covered, 80 °C heated water bath
  - Remove from NMP, squirt with IPA with bottle, 30 s
  - 2 IPA baths, 5 min each
  - Dry with N_2 spray gun

Dice wafer

- Spin AZ158 photoresist, 2000 rpm, 500 rpm/s, 30 s
- Hot plate, 115 °C, 2 min
- Using dicing saw, dice wafer into 4 large squares with devices and 8 edge "triangles" with test capacitors, 6 cuts total 1 mm/s, 8A blade

Top capacitor plate Al, with test capacitor chip (edge triangle)

- DI water rinse from faucet
- Solvent clean, spray with Acetone from bottle first to remove dicing particles (don't let Acetone dry in air)
- Hot plate, 115 °C, 5 min
- Photolithography for test capacitors, Heidelberg 160 mJ/cm^2, AZ 1:1 developer for 3 min
- Downstream O_2 clean #1
- E-beam evaporation, Al, 200 nm, 2 Å/s, no rotation
- Photoresist strip for liftoff, 3 h in NMP heated water bath, Sonication during first IPA bath
- Measure test capacitors with microwave probe station, fit capacitance, adjust device top plate capacitance accordingly

Top capacitor plate Al, with device quarter (inner square)

- DI water rinse from faucet
- Solvent clean, spray with Acetone from bottle first to remove dicing particles (don't let Acetone dry in air), No DI water
- Hot plate, 115 °C, 5 min
- Photolithography for top Al for capacitor, Heidelberg 160 mJ/cm^2, AZ 300 MiF developer, 1 min
- Downstream O_2 clean #1
- E-beam evaporation, Al, 200 nm, 2 Å/s, no rotation
- Photoresist strip for liftoff, 3 h in NMP heated water bath, Sonication during first IPA bath

Josephson junction deposition, with device quarter

- Spin e-beam resist
  - Spin MAA EL9, 1500 rpm, 500 rpm/s, 45 s
  - Hot plate, 160 °C, 600 s
  - Spin PMMA 950K A4, 2000 rpm, 500 rpm/s, 40 s
  - Hot plate, 160 °C, 600 s

- Deposit gold conduction layer with thermal deposition, 10 nm, 0.5 Å/s
- E-beam write, MAA undercut 350 μC/cm^2, PMMA + MAA (junctions) 1500 μC/cm^2, clearing dose (bandage connections) 2000 μC/cm^2
- Etch gold conduction layer
  - Gold etchant type TFA (KI 18-42 ppm solution), 10 s
  - DI water bath, 30 s
  - DI water rinse from faucet
  - Dry with N_2 spray gun
- Develop e-beam resist
  - Develop e-beam, 3:1 IPA, MIBK mixture, 40 s, gentle agitation
  - IPA bath, 30 s
  - Dry with N_2 spray gun
  - Downstream O_2 clean #1
- Evaporate Al with Plassys angled e-beam deposition, no ion mill, $\sim 1 \times 10^{-7}$mbar
  - Al deposition, 65 nm, -60 deg,0.2 nm/s
  - Oxidize in 15 % O_2 in Ar, 0.8 mbar for 30 min
  - Al deposition, 100 nm, 0 deg,0.2 nm/s
- Photoresist strip for liftoff, two NMP heated water baths: first 3 h, then squirt NMP from bottle to remove Al layer (don't let it dry in air), then 1 h in new NMP heated water bath.

Al Josephson junction bandages and crossovers, with device quarter

- Photolithography for Al Josephson junction bandages and crossovers, Heidelberg 160 mJ/cm^2, AZ 1:1 developer, 3 min
- Downstream O_2 clean #1
- Evaporate Al with Plassys, $\sim 1 \times 10^{-6}$mbar
  - 5 min ion mill
  - 200 nm Al
- Photoresist strip for liftoff, 3 h in NMP heated water bath, no sonication

Dice device quarter

- Spin AZ158 photoresist, 2000 rpm, 500 rpm/s, 30 s
- Hot plate, 115 °C, 2 min
- Using dicing saw, dice wafer into square chips with side 3 mm, 16 cuts total 1 mm/s, 8A blade

B.1.2 Substrate

Choosing a Substrate

Two commonly used substrates for superconducting circuits are sapphire and silicon, both materials work well with most of the cleanroom processes. Silicon wafers can be made with different bulk resistances. Low resistivity silicon (10-20 $\Omega-$cm) is relatively inexpensive, but devices made with this would be much lossier than those made with high resistivity silicon (10 k$\Omega-$cm) or sapphire. Because of this, we prefer to make devices using high resistivity silicon or sapphire. Our Sapphire wafers are purchased from Kyocera corporation, high resistivity silicon wafers from Silicon Quest International, and low resistivity wafers from Silicon Valley Microelectronics, Inc.

Low resistivity silicon is typically used for developing photolithography, deposition, or etch recipes. This low resistivity can be an issue when developing a process where we need an accurate measure of the resistance, such as Josephson junction fabrication. For this case we grow 500 nm of oxide using the cleanroom's furnace (Tystar Mini-Tytan 4600 Furnace System). Although these wafers covered with SiO2 are still not suitable for devices because SiO2 can be a lossy material, they are at least sufficiently insulating for measuring device resistances. We also use low resistivity silicon as a carrier wafer to hold small chips in ICP etch or deposition processes.

When deciding to make devices from either high-resistivity silicon and sapphire, qubits with lifetimes above 10s of μs have been made both [144, 22]. Although many process parameters will be similar between the two substrates, they will not necessarily give identical

results. For example, sapphire is transparent while silicon is not which will mean slightly different results during photolithography. Practically, a good rule of thumb is to check if there already exists an established cleanroom process for the given substrate. Initially we developed the JPA process on sapphire, but it was discovered that the failure rate when depositing the capacitor dielectric was reduced when using silicon (troubleshooting this issue will be discussed in depth later).

Cleaning the substrate

The first step when starting a fabrication process is to clean the substrate, which can be done with varying levels of cleanliness. For very aggressive cleaning, one could do a Buffered HF etch or Piranha etch. However, we instead do a simpler cleaning procedure which seems to give us reasonable lifetimes for our qubits. First putting the wafer in a beaker with Acetone while sonicating for 5 minutes, this removes organic residue. Then an IPA bath while sonicating removes Acetone (it's not a good idea to have Acetone dry on your wafer as it leaves a residue), and dry the wafer with Nitrogen gas(N2). The next step is to spray the wafer with DI water, which is supposed to provide a more physical cleaning step compared to the Acetone/IPA chemical clean. It is also thought that the DI water is cleaner than Acetone/IPA so better to finish with it.

We then put the substrate on a hot plate for 10 minutes. This is to evaporate any adsorbed water that may be present on the surface before depositing the base layer metal. Note that because no metal is currently on the substrate and the wafer can be safely heated to much higher temperatures than other times in the process.

B.1.3 Base layer

Base layer deposition

Two common metals used for fabricating superconducting circuits are Aluminum (Al) and Niobium (Nb). One notable difference between these two materials are their superconducting transition temperatures Tc. Al has a Tc near 1.2 K [24] while Nb has a Tc around 9.3 K [145]. If we were making resonators that operate near these Tc this could be important, as the quality factor of superconducting resonators continues to decrease below Tc and then saturates to some level once a low enough temperature is reached [33]. However, since we operate circuits in a dilution refrigerator at 10 mK, which is much lower than either Tc the difference between the two does not contribute to differences in the respective losses. Another difference between the two metals is that the native oxide growth on Al grows faster than that of Niobium. This means that when galvanic contact is needed between two metal layers, such as in junction deposition, Al base layers require an ion milling step to remove the native oxide while Nb base layers do not. Finally, etching the metals require different etch chemistries (ex:chlorine based vs. fluorine based etches). There are many groups using both base layers, it is not clear either metal gives better resonator lifetimes. For consistency between processes, our lab uses Al as a base layer for most processes.

We deposit base layer Al using an e-beam evaporator (Angstrom EvoVac Electron Beam Evaporator). Al can be sputtered, however sputtering tends to give larger grain sizes, which may be a source of loss due to more Aluminum oxide barriers between grains. The Al source in the evaporator, located below the wafer at the bottom of the vacuum chamber, is not vertically aligned with the wafer which may cause a gradient in the deposited Al. For this reason, when depositing the base layer, the sample is rotated to help get a more uniform thickness across the wafer. The thickness is measured using the tool's built in crystal oscillator, which changes frequency as material is deposited on it. Because the thickness measurement relies on good tool calibration, if the exact thickness is important it is good to

check the metal thickness with the profilometer after etching the base layer (see below). We typically make this layer 100 nm. Making thicker base layers than this tends to cause issues when getting later layers (such as junctions) to get over steps to get good galvanic contact. After depositing any materials on the wafer, we clean the wafer with the standard cleaning recipe because metal deposition is thought to be a relatively "dirty" process. This is also a good time to examine the wafer in the microscope to check the quality of the deposited material.

Base layer photolithography – Photoresist

For most photolithography processes we use AZ MiR 703, which is a positive photoresist (exposure to light removes resist with developer). We use this resist for both etch and liftoff processes. When using the standard spin recipe #3 (4500 rpm, 500 rpm/s, 30 s), this photoresist comes out around 900 nm thick. For a given spin speed, the photoresist tends to stabilize to a certain thickness, the spin time is relatively less important for setting the thickness. There is some variation in the photoresist's absorption with thickness and so you should re-calibrate the photolithography step if the spin parameters change for any reason and you have small features to expose. When doing liftoff processes a good rule of thumb is that the resist should be more than 3 times thicker than the material you are removing, so if you need to remove more than 300 nm of material you should use a thicker resist.

The spinner vacuum chucks can sometimes not be mounted well. This can lead to bad suction between the chuck and the wafer, and so at high speeds the wafer can fly off, ruining the device. Before turning on the spinner, it is a good idea to turn on the vacuum and slightly push the wafer to check if it stays in place well. If not you may need to remount the vacuum chuck.

Photolithography is one of the only processes in the cleanroom where you can "do-over" the step. You can clean off the photoresist with the standard cleaning recipe and redo the photolithography. However, the developer can partially etch away at Al and so there is a

limited number of times you can do this without over-etching the metal.

Photoresist is stored in the fridge in large containers, which we then transfer to the smaller glass bottles. When removing the large photoresist container from the fridge, we let it sit on the table for several hours before opening it. This is done so that water from the air does not condensate inside the bottle then mix with the photoresist. We solvent clean the small photoresist bottles and let they dry before putting photoresist inside in case the bottles happen to be dirty from wherever they come from. After pouring the photoresist from the large container, you should clean the container opening that now has some liquid photoresist on it. Photoresist on bottle lips dries, and the flakes can fall into the photoresist, creating large defects in your pattern when exposed. Keeping your small bottle clean from this dried photoresist is also important.

When putting photoresist on a wafer with a pipette, the most important points to keep in mind are to put enough photoresist so that it covers the entire wafer when spun and to avoid putting photoresist bubbles on the wafer. Popping bubbles might be bad, though this is claimed without evidence. Each person has their own technique on how to put photoresist on wafers (spirals, zigzag, in one spot), with few differences in results it likely does not matter.

Base layer photolithography – tools

When the PNF opened in 2016, we initially did our photolithography with a custom photomask for each design and and used the stepper for exposure (3C Technical GCA AutoStep 200 5x Reduction Stepper). Benefits of using a stepper are 500 nm feature resolution, 100 nm alignment precision between layers, and the ability to expose repeated patterns over an entire 4 inch wafer relatively quickly, on the order of several minutes. The main issue with using the stepper are that the designs are fixed, and ordering new photomasks takes several weeks to ship.

The Heidelberg maskless exposure tool takes a digital design file (DXF or GDS) as input

and exposes using a laser that directly exposes the photoresist (Heidelberg MLA150 Direct Write Lithographer). Because the laser is only able to write out features one at a time, exposing a full 4 inch wafer takes longer than the stepper, around 20 minutes. Directly writing the features means you have the useful ability to vary device parameters across the wafer. It also means you can design and write your pattern to the wafer within the same day. This flexibility also allows you to modify the design during the fabrication process, for example modifying the area of a parallel plate capacitor based on measurements from test devices. With careful calibration the Heidelberg can expose down to 1 um features, but 1.5 um is a safer minimum for typical use. Although this minimum feature size is larger than the stepper's, it is large enough for a wide variety of devices. As of this writing the Heidelberg is usually the most popular tool in the cleanroom, and so scheduling your processes in advance is useful.

Base layer photolithography – exposure

When calibrating a dose for a given process, you should lean towards overdosing rather than choosing the optimal line width for your process. This is because fluctuations in the tool parameters may lead to underdosing the exposure which will ruin your process. To compensate for the increased width due to overdosing, you can make features slightly smaller in the design. The Heidelberg has an option called "biasing" that does this for you, -200 nm is usually good.

Base layer photolithography - developers

We use two types of photoresist developers in our processes: AZ 300 MiF and AZ 1:1. The main differences between these is that AZ 300 MiF is faster and more reliable that AZ 1:1, however AZ 300 MiF also etches Al more. This etching can usually be ignored for processes with a Sapphire substrate. However, a silicon substrate is also etched for a non-negligible thickness in an Inductively Coupled Plasma (ICP) chlorine etch, which we use for

patterning our base Aluminum layer. If the Al was perfectly uniform, this effect would not be an issue but any roughness in the Al due to development is then transferred to the silicon substrate. Substrate roughness can cause issues when depositing Josephson junctions later in the process. So for Sapphire substrates we use AZ300 MiF to etch the base Al layer but for silicon AZ 1:1 is a better choice.

The amount that the photoresist develops is a function of the exposure dose, exposure area, developer type, agitation amount, and development time. If after placing the wafer for the standard time in the developer the patterns are not fully developed, you can continue with the development for slightly longer to develop more. For example, 30 second intervals of extra development and then look in the microscope to see if the pattern has improved.

One of the most frustrating issues in the cleanroom is that AZ 1:1 periodically fails to develop AZ MiR 703 even when using doses that previously worked well. Assuming this failure is due to the AZ 1:1, it is possible that when the AZ 1:1 level gets low it has a bad balance of chemicals due to evaporation or bad mixing and so we avoid using AZ 1:1 when the bottle is almost empty.

Base layer etch

Al is etched well by Chlorine chemistries so we use the chlorine RIE etcher (Plasma-Therm ICP Chlorine Etch). We originally had a run bias of 50 W, however we were having issues with burnt resist which remained after stripping the photoresist so we reduced the run power to 33 W. At this run power, 100 nm of Al are etched in about 12 s at which point you can see through the etcher's window that the Al disappears from the areas without photoresist. To make sure that we don't have any residual Al on the wafer, we etch for an additional 12 s for a total process time of 24 s. If the substrate is sapphire, this extra etching time is negligible because Cl etch does not etch sapphire very well. However, as previously mentioned, silicon is partially etched and so any surface roughness on the Al will be transferred to the substrate at this time.

Immediately after the Cl etch we put the wafer in a bath of water for 10 minutes. This is because of the possibility that there might be some volatile compounds remaining on the wafer after the etch process which may degrade the Al quality. Water will neutralize these compounds.

After removing and drying the wafer, this is a good time to look for defects in the base layer due to particulates. At this time, the particulates that caused the issue should still be on the wafer and so the defects much easier to notice than after the photoresist is removed.

Base layer photoresist strip

After some bad experiences with burnt photoresist that sticks to the sample even after stripping, we added an O_2 ashing step before the strip (YES G1000 Plasma Cleaning System). The idea behind this is that the RIE etch would form a hard layer of photoresist on top while the photoresist below is soft because it was protected. If we ash the wafer first with an aggressive O2 step, we remove the hard photoresist layer and can then remove the soft layer underneath with the standard strip recipe.

We preheat the NMP bath for 10 minutes on a hot plate before placing the wafer inside because cold NMP does not work very well as a stripper. Rather than wait for the NMP to heat up with the wafer inside we let it work on the photoresist immediately at a hot temperature. Note that although the hot plate is set to 80 C, the NMP actually only gets to around 60 C after the temperature stabilizes (K. Satzinger measured this once).

The wafer is placed upside-down in the NMP using a Teflon tripod holder so that any particulates fall on the beaker bottom rather than on your wafer. Sonication is done at multiple frequencies to more aggressively remove the photoresist. Our standard recipe mentions to do this at a medium power, however there is no particular reason for this other than to keep a consistent process. Although having different water levels in the sonication bath will also vary the effective sonication power so it's not clear if a consistent power matters in this case.

Base layer characterization

The first few times you do a deposition it useful to measure the material thickness, to get a sense for the variation in the deposition parameters over time. For the base layer we can use a profilometer (KLA-Tencor P-7 Surface Profilometer). While it is possible to get an estimate for the thickness by using the shadow of the clip holding the wafer in the electron-beam (e-beam) evaporator, this is not a particularly sharp edge and will likely underestimate the real thickness. Instead, it is more precise to use a large etched feature to measure the thickness. Al scratches easily, and so this feature for measuring should not be a critical feature in the device as the profilometer makes physical contact with the sample to measure the thickness. The profilometer needs a reference to calibrate the wafer slope, use the top of the Al for this rather than the etched substrate because the etch may not be entirely uniform.

Looking at the sample in the SEM can also provide useful information. We had a process issue where we found that all our junctions came out open after deposition. The cause only became obvious after looking the sample in the SEM and noticing the rough surface. We eventually pinned down the cause to the developer etching the Al layer, which was then transferred to the substrate silicon during etching.

B.1.4 Dielectric layer

Dielectric layer - photolithography

If a photolithography step immediately follows a stripping step, you should immediately spin photoresist on the wafer after finishing the strip, even if you are not planning to expose the wafer at that moment. Since the wafer is currently "clean", this is done to avoid dust and other particulates falling on your sample between steps. Non-exposed photoresist is stable as long as you don't expose it to light, though you probably don't want to wait several weeks in this state.

The Heidelberg sometimes struggles with keystone issues, that appears as flags after

development. This kind of additional feature is not as significant for the dielectric layer, however, for a top metal layer could lead to shorting a parallel plate capacitor. This was a bug related to not correctly assigning shape boundaries in the Heidelberg conversion software. There is a setting in the file conversion process that fixes this issue, although the conversion takes slightly longer for large files. While this issue was being debugged, one common stopgap solution was to add additional polygons to the design file to cover any breaks between polygons.

After photolithography before a liftoff process, we put the wafer in the O2 asher for a short amount of time and small power. This is done to remove any trace photoresist on the exposed areas which may impede good adhesion of the deposited material.

Dielectric layer - deposition

We form our dielectric layer from amorphous silicon (a-Si) a low loss dielectric that can be deposited in an HDPCVD tool (Plasma-Therm Apex SLR HDPCVD). Troubleshooting this step was one of the most time-consuming parts of developing the JPA. For nearly all a-Si depositions, after a few days the surface would be full of cracks and defects, likely caused by high material stress. Material stress can be measured by measuring the wafer curvature before and after deposition. Despite changing a wide variety of parameters that may impact the stress, and replacing the substrate from sapphire to silicon, no recipe produced a-Si that did not eventually have defects appear. Eventually, a working recipe was found by depositing a thin layer (10 nm) of SiN before depositing the aSi. We also discovered that a-Si was etched by the 300 MiF photoresist developer that is used in a later fabrication step. Depositing another thin layer (10 nm) of SiN on top of the a-Si was found to protect the dielectric during this step. This three layer process is all deposited at the same time in the HDPCVD tool, and so the final process does not take up much more time than just a single layer.

Dielectric layer - liftoff

Liftoff is done by leaving the sample upside down in a beaker of NMP for an extended period of time in a heated water bath. Smaller and delicate features such as Josephson junctions are in the bath for a total of four hours without sonication. The dielectric layer has larger features and so two hours is usually enough, and the sample can be put through a sonication bath at the end.

B.1.5 Gold Deposition and Liftoff

The e-beam process needs an alignment marker that has high contrast to its surroundings. Some groups achieve this contrast by deeply etching into the substrate. We prefer to deposit alignment markers. The thin film of aluminum and the dielectric do not effectively scatter electrons making them nearly invisible to the e-beam writer and not useful for alignment. Gold has a high atomic number relative to the substrate and so can be used for making alignment markers. The Heidelberg can have alignment errors up to around half a micron, and so this inaccuracy will translate to errors in the Josephson junction placement. For making JPAs, this error is tolerable but should be kept in mind for more accurate designs. After depositing gold, we avoid putting the chip in contact with water as gold and Aluminum can have an electrochemical reaction that causes defects on the Al surface.

B.1.6 Dicing into quarters

We spin AZ1518 at a relatively slow rate of 1500 rpm and then bake it for two minutes to harden it. The choice of AZ1518 is simply that it is a viscous resist and so when spun will result in a thicker layer that will better protect the wafer when dicing (Disco DAD3240 Automatic Dicing Saw) and when the wafer is flipped upside-down to attach adhesive tape to its back. Depending on the substrate material we dice at different speeds, sapphire is harder to dice and so needs a slower speed (usually 0.5 mm/s) than silicon which can be

diced faster. To maximize usable surface area the JPA wafer is subdivided into areas with devices and tests. During the dicing step we cut a total of 6 times, 3 on each axis. After dicing we end up with a total of 4 device array chips and 8 test device array chips. Depending on subsequent process steps the test devices are used to measure process parameters such as capacitances, galvanic contact between metal layers, and junction dose arrays. These tests are useful in optimizing later process steps for targeting specific device parameters.

B.1.7 Test Capacitors

Troubleshooting the process parameters for the dielectric layer caused the layer to have different thicknesses for the same deposition time. This made the resulting capacitances highly unpredictable. To get around this issue, we made capacitors of different areas and measured their capacitances. We can then adjust the area of the JPA top plate based on these measurements. After depositing and lifting off the top Al electrodes for these test capacitors, we can measure the capacitances at room temperature using a microwave probe station (Signatone 1160 series probe station) connected to a Vector Network Analyzer (Keysight PNA-X Network Analyzer N5242A). The VNA is first calibrated to remove the effect of the connected coaxial cables, and the capacitors are then measured over a wide frequency range and the scattering parameters are then fit to extract the capacitances.

B.1.8 Top layer capacitor pad deposition and liftoff

While we could have created the top capacitor pad during the junction bandage step, we wanted to avoid ion milling the capacitor pad in case it might change the capacitance values. When depositing the Al for the top capacitor layer, we don't rotate the sample. Rotating the sample would deposit metal on all four edges of the photoresist opening, which would make for a more difficult liftoff process. This metal layer is around 200 nm, twice as thick as the base layer, in order to be able to get over the etched base layer steps smoothly.

We do not have Teflon holders for these smaller chip arrays, so to place the chip upside-

down in the NMP we place it on a smaller beaker lid inside the bath. The curved edges of the lid prevent the chip from touching the bottom.

B.1.9 Josephson junction fabrication

E-beam resist spinning

Like photoresist, e-beam resist is also stored in small personal bottles. Unlike photoresist, e-beam resist can be used far past its expiration date without degrading its quality. There are two e-beam resists for depositing Josephson junctions, MAA and PMMA. PMMA is spun on top of the MAA. MAA develops more easily for the same e-beam dose and so is used to create undercuts in the resist that form the Dolan bridge for making Josephson junctions. These undercuts are also helpful for the liftoff process because smaller features tend to take more time to fully lift off in NMP. After spinning each resist layer we bake the resist for 10 minutes at 160 C. This is the highest temperature we expose the Al to during fabrication because higher temperatures can damage the quality of Al films. After spinning e-beam resist it is stable and does not need to be immediately exposed

We thermally deposit a 10 nm layer of gold to improve conduction on the sample for e-beam, since charging effects can significantly change features. This is a thermal deposition instead of e-beam deposition in order to avoid exposing the resist.

E-beam writing

We pattern our junctions with the an e-beam writer (Raith EBPG5000 Plus E-Beam Writer). Although the e-beam is capable of aligning to local alignment markers near the features of interest which may improve alignment precision, because we made the alignment markers relatively imprecisely using the Heidelberg a global alignment with only a few alignment markers is fine. To avoid errors while writing, it is important to make sure the chip is flat (within 20 um across the chip is usually a good target), and aligned well to the correct axis.

In my experience, one of the most common e-beam errors among new users is to align the chip to the wrong axis, so this is worthwhile to double check.

JPAs require large area junctions, however Dolan bridges have limitations to their size due to fabrication issues such as bridge collapse for the length and deposition angle for the width. We found that the largest area junctions we could reliable write around $0.5\,\mu$m x $4\,\mu$m. Due to overdosing, the junction areas that are written are typically larger than the design areas. For our e-beam current (1 nA) and dose ($1500\,\mu\mathrm{C/cm^2}$), this bias increases the width and length on the order of 100 nm, give or take a few tens of nm depending on the junction size.

E-beam Gold Etch and development

Before developing the e-beam resist we need to etch away the gold film on top. With the gold etchant type TFA (KI 18-42 ppm solution), this etch process takes only 10 seconds. It seems that different people sometimes get different junction resistances for identical processes, one potential cause is that each person has a different technique for agitating the chip in the IPA/MIBK developer. This could cause the junction sizes to be different between fab runs, and so consistency in this process is important. After drying off the chip it is put into the O_2 asher for a gentle clean and then immediately put into the Plassys evaporator for deposition.

Junction deposition

We deposit junctions using an e-beam evaporator (Plassys Electron Beam Evaporator). The Plassys has a few important features that allow it to be used to deposit junctions. First, the stage can be rotated to deposit at an angle. Second, we can connect an oxygen bottle to the tool to oxidize junctions at a specific pressure and time. The Josephson junction resistance is a function of both the oxidation pressure and the oxidation time. We oxidize for a relatively long time (currently 50 minutes) so that the oxidized layer reaches a steady state and becomes insensitive to the exact oxidation time. This makes our junctions more reproducible for a

given pressure. However, the pressure sensors are not necessarily accurate and so we try to reuse the same junction deposition pressure and time, and then modify junction resistances by changing the junction area. The resulting Josephson junction resistances tend to fluctuate around ±20% between depositions with nominally identical design parameters. It's not clear if this is due to variations in junction area (either from e-beam writing or development) or due to variations in deposition conditions. It's good practice to check the beam location on the crucible and adjust if necessary. Keeping the beam location in one spot for too many depositions can form a deep valley in the crucible metal that can affect metal thickness and possibly destroy the tool if the beam reaches the crucible base.

When designing the junctions, it is important to add generous undercut areas below the junction area (currently 800 nm). This is because the angled evaporation evaporates onto the resist wall if the area is not large enough, which can create walls of metal near the junction. This wall of metal can make the liftoff harder and possibly collapse on the junction during liftoff.

Junction liftoff

Because Josephson junctions have small features, the liftoff is a long process. Josephson junctions are delicate structures and so we avoid sonicating them. After a 3 hour NMP bath, we spray away the Al with a spray bottle and return the chip to NMP for another hour in case there is any remaining Al on the chip.

Bandage deposition

The Josephson junctions need to be galvanically connected to the base layer, however Al has a thin oxide that prevents electrical contact. While we could ion mill the substrate during the junction deposition step, this might change the junction size. We instead have a second Al deposition step where we connect the junctions to the base layer by adding a bandage. The ion mill does not remove material equally everywhere on the wafer, it is a good idea

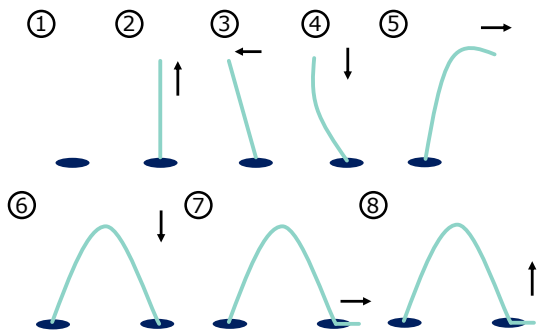

Figure B.1: **Wirebond steps cartoon.** Cartoon showing the steps involved in moving the manual wire bonder tip for good wirebonds.

to first determine the etch rate over the wafer using silicon wafer that has been thermally oxidized. One can then convert the SiO_2 etch rate to Al02 rate to determine how long to etch for. Crossovers also require galvanic contact and so the bandage deposition is also used to create the top Al layer for the crossovers.

B.1.10 Chip design

Here we outline several of the JPA design characteristics that relate to fabrication considerations.

Josephson junctions are sensitive to shocks and so any time we touch a part of the chip that electrically connects to the junctions we risk shorting the junctions. One simple design change with this in mind is to create a border at the edge of each device, so that when we handle the chip array each device chip is electrically isolated.

When the chips are diced into individual devices, you need a way to hold the chips. For small chips such as the JPA chip you can use tweezers and hold it across both edges. For larger chips you should leave some space on the corners to hold the chip.

B.1.11 Wire bonding

When first learning to wire bond by hand, Étienne Dumur drew a helpful figure for explaining step by step the hand motions involved. Fig. B.1 is a reproduction of this explanation.

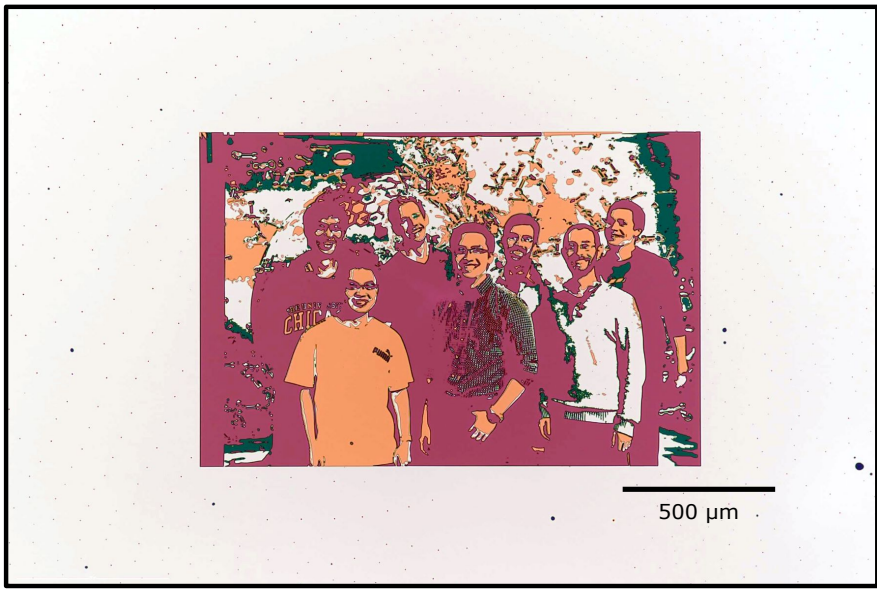

Figure B.2: **Group picture photolithography.** Microscope picture of patterned Al and a-Si on a thermally oxidized Si substrate. The original picture was of Cleland lab graduate students taken at the UChicago Institute for Molecular Engineering holiday party in December 2015, which was the first quarter the Cleland lab was in Chicago. The colors are real, with purple (SiO2 on Si), green (a-Si on SiO2 on Si), white (Al) and orange (a-Si on Al). The vast majority of laser writing time for photolithography is spent physically moving the laser around the wafer, so adding pictures such as this between test samples does not add significant time to the process. Left to right: Ming-Han Chou, Youpeng Zhong, Kevin Satzinger, Hung-Shen Chang, Greg Peairs, Joel Grebel, Rhys Povey.

B.2 Remote resonator communication device fabrication

B.2.1 Recipe

This is the recipe for the resonator communication experiment in chapter 5. See subsection B.1.1 for more details about repeated process steps (ex: solvent clean, photolithography, etc.), and starting in subsection B.2.2 for additional discussion about fabrication steps not present for the JPA.

- Start with a sapphire wafer, 4 inch

Base layer Al Same as in section B.1.1, except develop photoresist with AZ 300 MiF developer for 1 min instead of AZ 1:1.

Fix base layer transmission line shorts

- Measure transmission line resistances with DC probe
- Locate shorts with e-beam microscope and record coordinates on wafer
- Photolithography to fix base layer shorts, Heidelberg 200 $\mathrm{mJ/cm^2}$, AZ 1:1 developer for 3 min
- Al etch in Cl RIE
- Photoresist strip for etch process

Dielectric layer

- 115 °C bake, 5 min
- Photolithography for dielectric layer, Heidelberg 200 $\mathrm{mJ/cm^2}$, AZ 1:1 developer for 3 min
- Downstream O_2 clean #1
- SiO_2 e-beam evaporation
  - Replace SiO_2 in crucible with fresh SiO_2 from bottle
  - Load wafer using angled sample holder facing target.
  - Deposit 200 nm, 1.5 Å/s, no rotation, $\sim 1 \times 10^{-6}$ Torr
- Photoresist strip for liftoff, 3 h in NMP heated water bath, sonicate 5 min in first IPA bath

Gold Layer Same as in section B.1.1, except Heidelberg dose is 180 mJ/cm^2 instead of 160 mJ/cm^2

Dice wafer Same as in section B.1.1, except dice at 0.5 mm/s with 8A blade. Inner device "squares" are 44.5 mm to a side, with one corner reaching the wafer edge

Josephson junction deposition Same as in section B.1.1, except Al deposition is 1 nm/s instead of 0.2 nm/s. Oxidation is 50 mbar for 50 min instead of 0.8 mbar for 30 min

Al Josephson junction bandages and crossovers Same as in section B.1.1, except Heidelberg is 180 mJ/cm^2

Check devices

- Measure Josephson junctions with DC probe
- Look for defects on chips

Dice device quarter Same as in section B.1.1, except square chips have 2 cm side

Vapor HF release

- DI water rinse from faucet
- Solvent clean, spray with Acetone from bottle first to remove dicing particles (don't let Acetone dry in air)
- Hot plate, 115 °C, 5 min
- Vapor HF, 15 Torr, 5 mg/min water flow, 3 min etch time.

B.2.2 Base Al etch with 2 m *waveguide*

Fabricating the 2 m long CPW transmission line is done in the base layer Al etch step. Because of its long length, and small gap size[2], it is difficult to get a high yield rate. Instead of AZ 1:1 as in the JPA fabrication, we use AZ 300 MiF developer for the base layer due to its higher reliability for development. One common reason for transmission line shorts are dried photoresist particles a few μm in diameter that are on the photoresist during resist exposure. These particles may either originate from our small personal photoresist bottles

2. 4 μm center trace and 2 μm gap

or come from resist rebounding from the photoresist spinner covered by old dried resist. The lines have had fewer defects when using fresh photoresist from the source bottle and a clean photoresist spinner.

Detecting defects in the line is not a trivial task as the search area is large and the features are small. We added an electrical probe in the center of the waveguide[3] which helps to detect the presence of opens or shorts. While the electrical test is useful, it does not detect all shorts as Al still has a finite resistance at room temperature which would cause issues when the metal superconducts at cryogenic temperatures.

We can visually locate the defects by using a dark-field technique using the e-beam microscope. When angled light scatters off the etched transmission lines, any features parallel to the light source are attenuated while features perpendicular to the light sources are amplified, allowing us to detect breaks in the transmission line only a few μm in size. Furthermore, the e-beam microscope has position tracker for wafers that lets us note the precise locations of these defects and correct them in a follow up step using the laser writer. This method of correcting transmission line shorts was used for the experiments in this work, although it is quite time consuming. A newer, promising technique developed by Haoxiong in our lab instead etches the entire waveguide in two lithography steps, which seems to provide a high device yield rate with less effort.

3. This electrical probe later caused issues in wavepacket distortion for communication when we cooled down the device. This was fixed by scratching the connection to the probe using a wire bonder with an old wirebond tip in order to reduce its capacitive load.

APPENDIX C

HALF WAVE PURCELL FILTER

Purcell filters are used to filter out noise from the readout line while maintaining high readout fidelity. Dan Sank's Thesis [63] (Chapter 4) has several useful design equations for designing a quarter-wave bandpass filter as a Purcell filter. In this thesis we use a half-wave bandpass filter, and so some of the equations need to be slightly modified from that thesis but the design follows similar principles and so we will be following the derivations there closely. Similar half-wave filters as in this thesis were used by other experiments in our group in [42, 43]. A picture of a half-wave filter used in this thesis is shown in Fig. C.1

When designing our half-wave bandpass filter we need to calculate the length, input tap location, output tap location, and the locations of any resonators that are inductively coupled to the filter. These quantities will be derived in this order.

C.1 Filter length

The length of the filter l_p is given by half a wavelength in a CPW transmission line

$$l_p = \frac{\lambda}{2} = \frac{\pi c}{\omega_F \sqrt{\epsilon_{\text{eff}}}}, \tag{C.1}$$

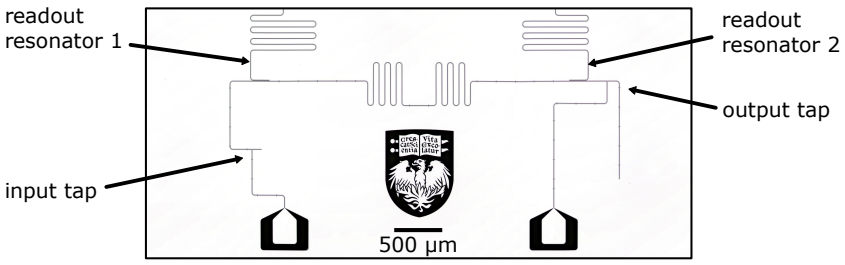

Figure C.1: **Half-wave Purcell filter.** Half-wave Purcell filter with labeled input tap, output tap and coupled readout resonators

where λ is the wavelength, c the speed of light, ω_F the filter frequency, and ϵ_{eff} is the effective relative dielectric constant of the waveguide. $\epsilon_{\text{eff}} \approx \frac{1+\epsilon_s}{2}$ is a reasonable approximation of this value, with ϵ_{sub} the dielectric constant of the substrate and 1 is the dielectric constant of vacuum. $\epsilon_{\text{sub}} = 11.4$ is the value we typically use for sapphire substrate.

C.2 Tap locations

The input to a bandpass filter is designed to be weakly coupled, while the output is strongly coupled. This asymmetric coupling significantly reduces the qubit loss through the input line while maintaining readout fidelity. Intuitively, the reflection due to the weak input coupling shouldn't affect the fidelity because you can drive harder to get the same photon number at the readout resonator. In the filter used in this thesis, both the input and output couple to external lines through taps. These taps are CPW lines that connect to the bandpass filter. Taps have the strongest coupling to the resonator mode at the voltage maxima. For the half-wave resonator, this voltage maxima occurs in the middle of the line. To calculate the coupling quality factor at this voltage maxima we first approximate the resonance as a lumped element RLC circuit as given in Table 2.1, specifically the 1 open 1 short resonator with the coupling near the open. Coupling to this location, the circuit is equivalent to two short-circuited quarter-wave resonators in parallel [1]. The shorted quarter-wave resonator operating at its lowest harmonic has an equivalent inductance $L_{p4} = \frac{4Z_{0p}}{\pi\omega_p}$ and an equivalent capacitance $C_{p4} = \frac{\pi}{4\omega_p Z_0}$, where Z_{0p} is the characteristic impedance of the resonator CPW. The equivalent impedance of each quarter-wave resonator is $\sqrt{\frac{L_p}{C_p}} = \frac{4Z_{0p}}{\pi}$, and both combined in parallel is $Z_p = \frac{2Z_{0p}}{\pi}$.

The environmental coupling is modeled as a resistance R_0 to ground where $R_0 = Z_{0c}$, with Z_{0c} the characteristic impedance of the coupling line. Finally, the coupling quality factor at the voltage maxima is given by $Q_{Fm} = \frac{R_0}{Z_p} = \frac{\pi}{2}$, the expression for the quality

1. It's important to note that this is a different circuit than the shorted half-wave resonator described in [27] Chapter 6. There the coupling is at the end of the resonator while here the coupling is in the middle

factor of a parallel resonator.

To calculate the coupling quality factor Q_F at an arbitrary point on the resonator we scale Q_{Fm} proportionally to the square of the voltage at the point of interest relative to that at the voltage maxima. Placing the tap at a distance l_t from a shorted end of the resonator we find[2]

$$Q_F = \frac{Q_{Fm}}{\sin^2\left(\pi l_t/l_p\right)} = \frac{\pi}{2\sin^2\left(\pi l_t/l_p\right)}. \tag{C.2}$$

The inverted expression tends to be more useful for design, $l_t = \frac{l_p}{\pi}\arcsin\left(\sqrt{\frac{\pi}{2Q_F}}\right)$.

C.3 Resonator locations

This calculation is similar to that determining the tap locations in the previous section in that we first create a lumped element RLC model of the bandpass filter, find the maximum coupling to the filter, and then scale that coupling by varying the coupling location. The sections are different in that we are now coupling a resonator rather than an input/output line and that coupling is inductive.

As shown in Fig. C.1 the resonators are inductively coupled to the half-wave bandpass filter which means that the location with maximum coupling is the current maxima rather than the voltage maxima. For two inductively coupled lumped element resonators, the coupling g is given by[17]

$$g = \frac{1}{2}\frac{M}{\sqrt{L_1 L_2}}\sqrt{\omega_1\omega 2}, \tag{C.3}$$

where M is the mutual inductance, and L_1 and L_2 are the lumped element inductances for resonators 1 and 2. The points of maximum coupling with current maxima are at either end of a half-wave resonator, and so we model the bandpass filter as a single half-wave resonator. Reading off from Table 2.1 using the 2 short type resonator, the equivalent inductance is

2. The factor of 2 difference here in the sin compared to the Sank thesis is due to using the full length l_p of the filter in the expression instead of the distance from the voltage maxima to the shorted end $l_p/2$

$L_p = \frac{Z_{0p}\pi}{2\omega_p}$. The readout resonator is a quarter-wave resonator with the coupling near the short and has an equivalent inductance of $L_r = \frac{Z_{0r}\pi}{4\omega_r}$, where Z_{0r} is the characteristic impedance of the resonator CPW. Assuming that $\omega_p \approx \omega_r$ and that $Z_{0p} = Z_{0r} = Z_0$, The coupling strength at the current maximum is then $g_{max} = \frac{\sqrt{2}\omega^2 M}{Z_0\pi}$. The coupling is reduced by the relative amplitude of the current $\cos\left(\pi l_r/l_p\right)$ at different locations l_r of the resonator. the resonator coupling g_r is now

$$g_r = \frac{\sqrt{2}\omega^2 M}{Z_0\pi}\cos\left(\pi l_r/l_p\right). \tag{C.4}$$

The decay rate for a resonator coupled to another dissipative resonator on resonance is[3] [15] $\kappa_r = \frac{g^2 Q_p}{r}$. Substituting the expression in Eq. C.4 using the two equivalent resonator inductances, the resonator decay rate κ_r is

$$\kappa_r = \frac{2M^2\omega_r^3 Q_p}{Z_0^2\pi^2}\cos^2\left(\pi l_r/l_p\right) \tag{C.5}$$

C.4 Additional design considerations

κ_r should be chosen with the goal of maximizing visibility with the criterion [63]

$$\kappa_r = 2\chi, \tag{C.6}$$

with χ the dispersive shift. With this equation we still have an additional degree of freedom, as we can increase both κ_r and χ together to keep the maximum visibility condition. Typically, we choose a χ that leads to some acceptable qubit Purcell decay $\gamma = \frac{1}{T_1}$, where T_1 is the relaxation time of the qubit. When the qubit and resonator are in the dispersive

3. The derivation in [15] in the Purcell filter section is for capacitive coupling of a qubit to a resonator, but the final answer is in terms of a generic coupling between resonators which should equally apply to inductive coupling between two resonators

regime, without a Purcell filter $\gamma_{\text{no filter}}^{\text{purcell}} = \left(\frac{g}{\Delta}\right)^2 \kappa_r$, while with a Purcell filter [15],

$$\gamma_{\text{yes filter}}^{\text{Purcell}} = \kappa_r \left(\frac{g}{\Delta}\right)^2 \left(\frac{\omega_q}{\omega_r}\right) \left(\frac{\omega_r}{2Q_p\Delta}\right). \tag{C.7}$$

Here g is the qubit/resonator coupling, ω_q is the qubit frequency, and $\Delta = \omega_q - \omega_r$.

APPENDIX D

SINGLE QUBIT TUNE UP TUTORIAL

One of the first steps that a researcher needs to do when their qubit sample cools down is to tune up the qubit. The tutorial builds upon a presentation I originally made for myself in the lab when learning how to tune up qubits from Audrey Bienfait, which turned out to be surprisingly popular by others despite its rough presentation. The two example samples here are transmon qubits with tunable frequency, which are measured dispersively through a readout resonator. The first sample which I will name "Sample1" is the first qubit that I tuned up myself (fabricated by Youpeng Zhong), which I include both for sentimental and illustrative reasons. The second qubit sample (fabricated by me) which I will name "Sample2" has additional data to fill in some missing plots which is also useful to contrast with the first sample. Neither of these represents the better samples or qubit parameters that we achieve in our group.

Before beginning, a word of encouragement to those afraid of destroying their sample by applying too large of a signal. Using typical electronics found in a superconducting circuits laboratory it is difficult to unintentionally destroy a sample cooled down in a dilution refrigerator (DR). For more specific guidelines, assuming typical wiring for qubit measurements (See section 3.1.3), sending powers below 0 dBm and voltages of a few volts at room temperature should be fine. For higher powers up to 10 or 20 dBm, the DR may heat up and the sample may go above its superconducting temperature, but shouldn't damage it. Although it's always a good idea to check that lines are correctly connected.

The first step to do after DR cools to base temperature is to do a broad frequency scan of the readout line. This can either be done with a VNA or with the FPGA DACs and ADCs. The VNA may be faster and simpler to set up for these simple kinds of scans. The scan should be done at low power to avoid non-linear effects. For reference, -140 dBm at a few GHz very roughly corresponds to order of 1 photon at the sample. For example, if there is 60 dB attenuation in the DR, an input power of -80 dBm at room temperature should work

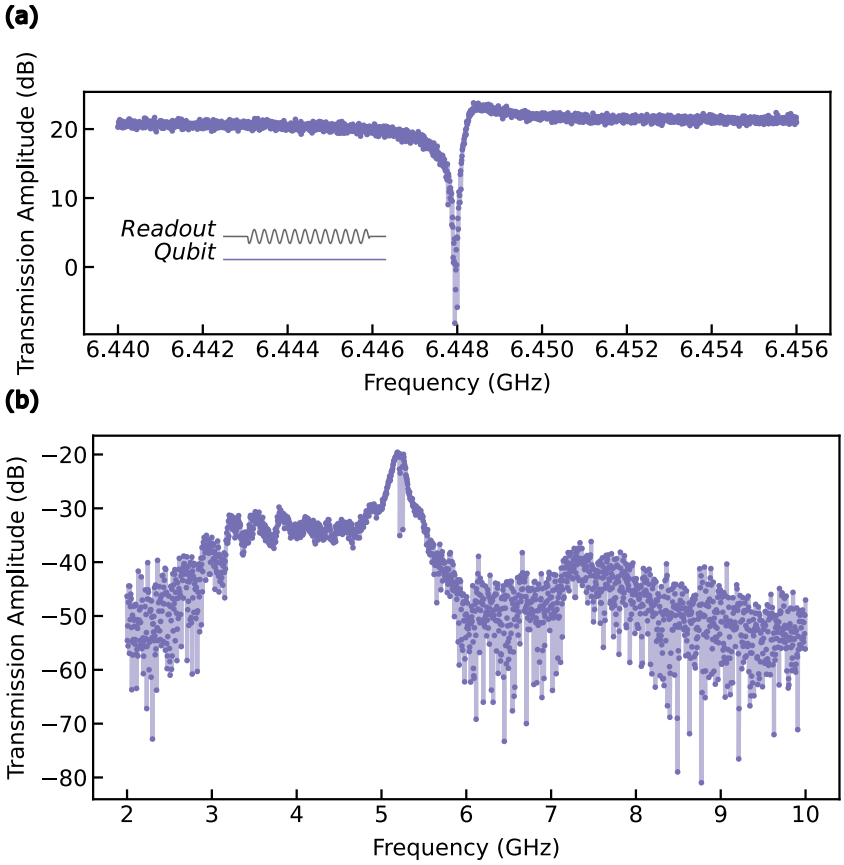

Figure D.1: **Locating the readout resonator.(a)** Sample1 transmission measurement through the readout line. **(b)** Sample2 wide frequency scan through the readout line. The high transmission peak is due to a Purcell filter on this sample, and two dips are visible within the feature. Other peaks visible in this scan are likely chip and packaging box modes.

well for an initial scan. The readout resonator frequency will appear as a narrow (typically designed to be a few MHz) dip in the signal as in Fig. D.1. If you do not see a resonator dip at the expected frequency, you can try expanding the scan range, increasing the number of measured points within the frequency range, or reducing noise (either by reducing the IF bandwidth or increasing averaging).

After locating the readout resonator frequency, scan the transmitted signal through the readout line as a function of the signal frequency (narrowly around the readout resonator, maybe a few tens of MHz) and the input signal power. If the readout resonator was a superconducting resonator by itself, its frequency would be independent of the power used to probe it. However, when coupled to a 2 state system, the resonator frequency will shift

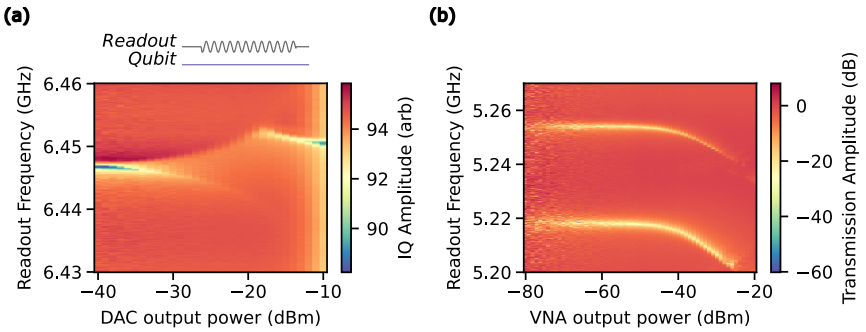

Figure D.2: **Power spectroscopy.(a)** Sample1 power spectroscopy scan showing readout resonator detuning as a function of DAC output power. **(b)** Sample2 power spectroscopy scan. The ideal readout power for qubit measurement is a tradeoff between noisy data at low readout power and non-linear effects at higher readout power as is seen in this scan.

as a function of frequency as in Fig. D.2. If you see this non-linear shift, it is great news, because it means that the qubit is "alive". For our systems this shift is on the order of a few MHz, and is set by the dispersive shift χ. At high powers the qubit will saturate and decouple from the readout resonator (same process as hole-burning Two Level Systems). When we will eventually maximize the qubit readout fidelity, readout power will be one of the parameters we vary. However, to find the qubit frequency we will initially set the readout power low where frequency varies little with readout power to simplify the effects that might occur. The ideal readout power will likely be higher than this initial value.

For qubits with tunable frequency, we can now scan the transmitted signal in the readout line as a function of frequency around the readout resonator (again narrowly around the readout resonator, maybe a few tens of MHz) and the qubit DC bias. The resulting plot looks different depending on whether the qubit frequency crosses the resonator frequency during the tuning process, but both cases can be fully explained with the Jaynes-Cumming Hamiltonian at low power. If the qubit does not cross the resonator, then the resonator frequency will increase and decrease with the qubit frequency, as seen in Fig. D.3c. The maximum (minimum) resonator frequency corresponds with maximum (minimum) qubit frequency, whether the resonator is above or below the qubit. If the qubit crosses the resonator we see avoided level crossings as in Fig. D.3a, where the positive parabolic-like region

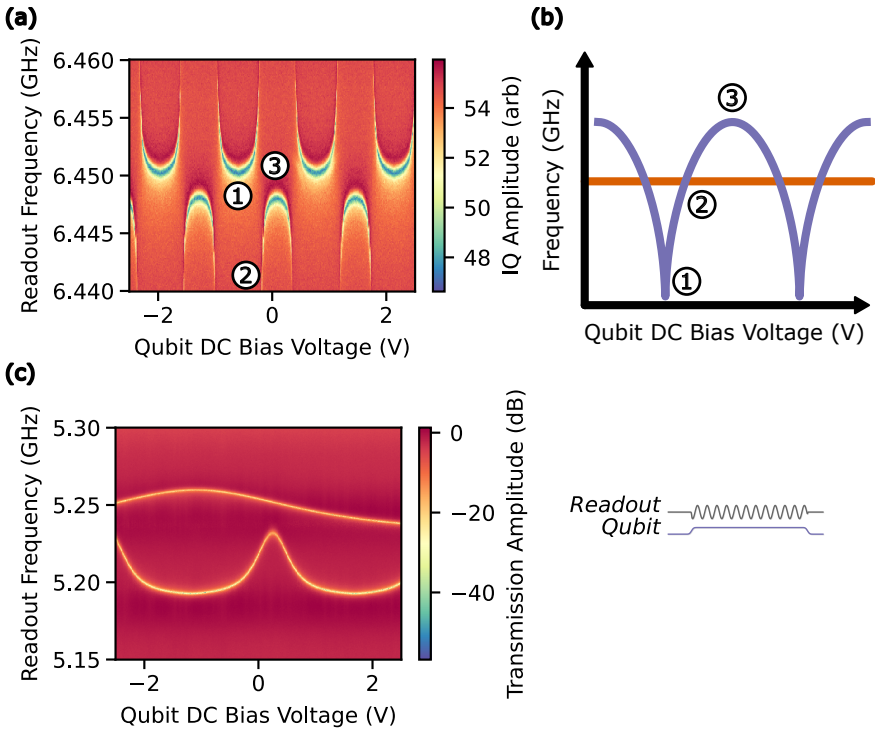

Figure D.3: **Bias spectroscopy.(a)** Sample1 bias spectroscopy scan showing readout resonator detuning with qubit bias when the qubit crosses the readout resonator **(b)** Cartoon showing how a decoupled qubit (blue curve) and resonator (orange horizontal line) would result in the readout resonator plot in (a) **(c)** Sample2 bias spectroscopy scan showing readout resonator detuning with qubit bias when the qubit is always below the resonator frequency. The lower frequency resonance is the resonator coupled to the qubit we are biasing, while the upper frequency resonator is changing to large qubit/qubit flux crosstalk. See Section 5.2.4 for more information about flux crosstalk

indicates the qubit is below the resonator and the negative parabolic-like region indicates the qubit is above the resonator. If the qubit does not cross the readout resonator, we can set the bias to where the qubit frequency is maximized. Otherwise, if there is an avoided level crossing we can choose a bias where the readout resonator is detuned only a few MHz away from its center value. We typically design the qubit frequency to be below the readout resonator because when placed above the resonator higher resonator modes reduce the qubit T_1 [146].

To find the exact qubit frequency we now do two-tone spectroscopy [128]. While reading out at the resonator minimum (a slightly positive frequency from the resonator minimum is also fine), scan the frequency of a long (few μs) continuous microwave tone on the qubit

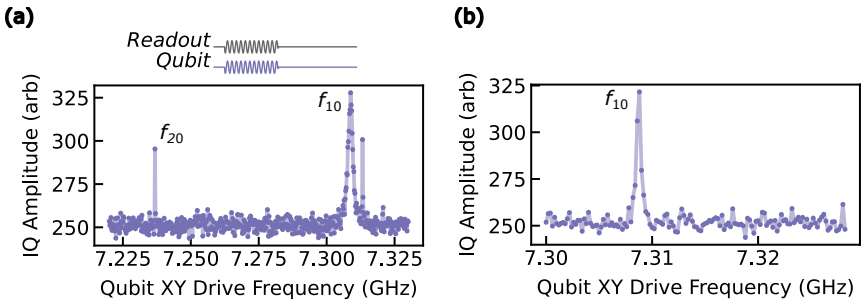

Figure D.4: **Two-tone spectroscopy(a)** Sample1 two-tone spectroscopy at high XY drive power. The qubit $0 \rightarrow 1$ transition peak f_{10} is shown with the two photon $0 \rightarrow 2$ transition as well as a third undesired peak. **(b)** Sample1 two-tone spectroscopy at lower XY drive power, the extra undesired peak around the 10 peak is gone. Not shown, the f_{20} peak is also not visible at this lower drive power

XY line. When the XY line tone is resonant with the qubit frequency, the qubit will go from its ground state to a mixed state between the $|0\rangle$ and $|1\rangle$ states. The qubit mixed state will cause the resonator frequency to shift down, leading the readout signal to increase because we chose to read out at the resonator minimum. This will show up as a peak in the scan as shown in Fig. D.4. If the XY line tone is strong enough, a second sharper peak will appear which is associated with the two-photon excitation of the qubit $|0\rangle$ to $|2\rangle$ state. Given a qubit anharmonicity α, the frequency f_{20} of the $0 \rightarrow 2$ transition will be $-\alpha/2$ (note α is negative for transmon qubits) lower than the frequency f_{10} of the $0 \rightarrow 1$ transition. Other unexpected peaks that might show up during this scan usually go away after reducing the XY line tone power[1]. We now set the qubit frequency at the maximum of the f_{10} peak. If you can't see any peaks, the qubit may be detuned outside of the scan range and you can try a different qubit DC bias. It's also possible that the XY drive line is disconnected, either due to faulty DR wiring or forgetting to connect the line at room temperature. As previously mentioned, it's always a good idea to check that lines are correctly connected. And that the signal generator is powered on.

The following measurements require more precise time control, and so can't be done with a VNA. For a description of the electronics we use for qubit measurements in our lab

1. Peak linewidth is proportional to the square root of drive power [147]

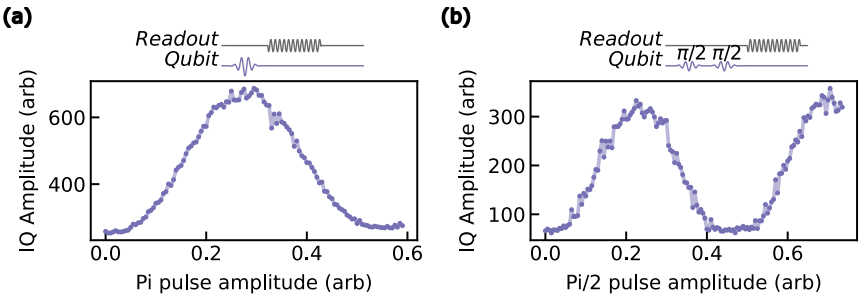

Figure D.5: **Qubit pulse tuning (a)**Sample2 pi pulse calibration. **(b)** Sample2 pi/2 pulse calibration

see [18]. To tune up the pi pulse we first apply an XY drive (the pi pulse) at the qubit frequency shaped by a Gaussian envelope and then apply a readout pulse with rectangular envelope (initial value of 1 μs can work) to monitor the readout amplitude. The maximum length of the pi pulse is limited by the qubit T_1 ($10s$ of μs at the time of this writing for our lab) while the minimum length is limited by α and may be brought down to a few 10s of ns [148]. For our lab's experiments we don't usually over-optimize this value and choose a reasonable value, like 80 ns. Assuming the qubit starts in its ground state, the amplitude will start at a minimum at 0 power, increase to a maximum and then oscillate between the two values as seen in Fig. D.5a. These are Rabi oscillations [149]. We choose for the pi pulse amplitude the first of these maxima. The pi/2 pulse tuneup is similar to the pi pulse tuneup, except we chain two pi/2 pulses together and choose an amplitude at the first maxima of the oscillations.

With a tuned up pi pulse we can calibrate the IQ scatter plot as shown in Fig. D.6. I and Q are the x and y axes of the IQ scatter plot respectively and refer to the readout signal quadratures. For example points on the I and Q axes with the same amplitude are the readout signal at the readout frequency measured at the ADC as sine waves with relative phase 0 and $\pi/2$ respectively. If the qubit remains in the ground state and we perform a series of identical measurements, the measured points will form a Gaussian distributed cloud where the width of the Gaussian distribution represents the measurement noise. Applying a pi pulse before reading out the state will shift the location of this cloud in the IQ plane. We

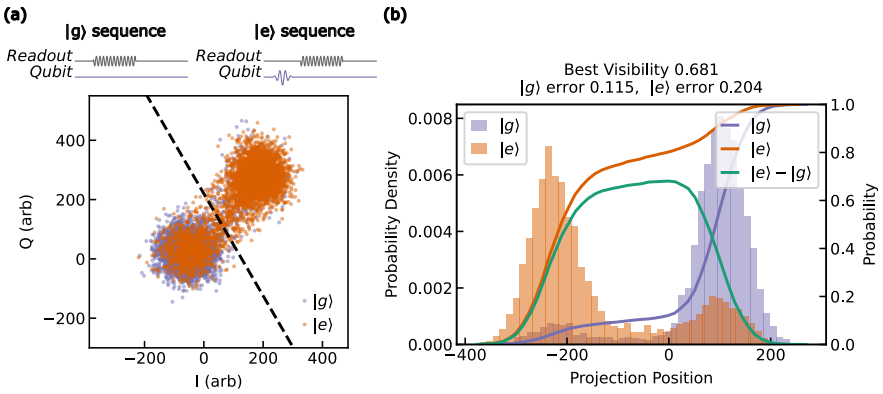

Figure D.6: **IQ scatter plot (a)**Sample2 IQ scatter plot **(b)** Histogram of data from (a) collapsed along axis perpendicular to IQ dividing line. From this plot we can see that some population in both the excited and ground state are misassigned, lowering the visibility further than just calculating the SNR would predict.

will use these clouds to split up the IQ plane into two regions separated by line and infer that if a subsequent measurement falls in one of the two regions that the qubit was either in the ground state. We choose to place the line so that we maximize the measurement visibility, defined as the percent of the ground state and excited state clouds that are in the "correct" side of the IQ plane.

Improving the achieved measurement visibility is an ongoing research effort and is a critical metric for scaling up quantum systems. The causes of low visibility are usually bundled up into the general category of SPAM (State Preparation and Measurement) errors. Fig. D.6 shows misassigned states in the IQ scatter plot which may have several causes. First, it is possible that the qubit state was not prepared correctly. For example, the qubit may be hot leading to a partial mixed state. Or the pi pulse fidelity may not be tuned up correctly in frequency, amplitude, length, or pulse shape [150]. A qubit prepared in the excited state may also decay before or during measurement due to low T_1.

Assuming the qubit was prepared correctly, the measurement process may lead to incorrect assignment of the qubit state. The two clouds we use to divide up the IQ plane may be partially overlapping, and so there is some error in this measurement of the qubit state. The larger the separation between the clouds relative to the cloud width the better we will be able

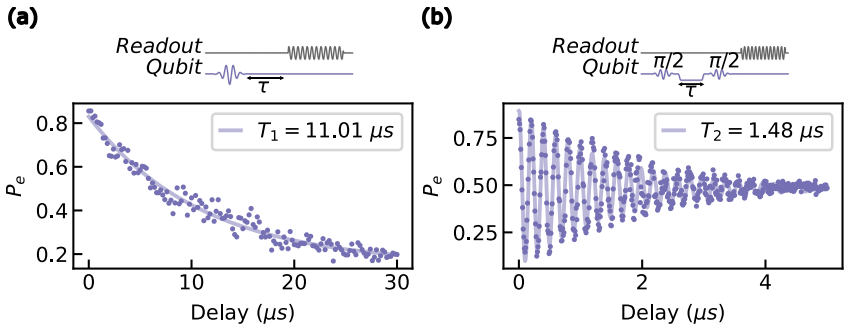

Figure D.7: **Qubit T1 and T2 measurement(a)** Sample2 T1 measurement fit to exponential **(b)** Sample2 T2 measurement fit to decaying sine

to distinguish between the two qubit states. This is also known as the SNR (Signal to Noise Ratio). See Sec. A.1 for more information on low noise measurement. [63] is also a good resource for understanding the relevant factors in qubit measurement. In practice, varying the readout pulse duration, power, and frequency may lead to improvements in visibility.

The next step is to characterize the qubit quality through the parameters T_1 and T_2 as shown in Fig. D.7. These values are both functions of the qubit frequency, and so choosing the qubit frequency is a tradeoff between good visibility, good T_1 and potentially detuning from other devices part of the experiment to be run.

BIBLIOGRAPHY

[1] Richard P Feynman. Simulating physics with computers. *International Journal of Theoretical Physics*, 21(6-7):467–488, 1982. [Cited on page 1.]

[2] David Deutsch and Roger Penrose. Quantum theory, the Church–Turing principle and the universal quantum computer. *Proceedings of the Royal Society of London. A. Mathematical and Physical Sciences*, 400(1818):97–117, 1985. [Cited on page 1.]

[3] Ethan Bernstein and Umesh Vazirani. Quantum complexity theory. In *Proceedings of the twenty-fifth annual ACM symposium on Theory of computing*, pages 11–20, 1993. [Cited on page 1.]

[4] Daniel R. Simon. On the power of quantum computation. *SIAM Journal on Computing*, 26(5):1474–1483, 1997. [Cited on page 1.]

[5] Peter W. Shor. Polynomial-time algorithms for prime factorization and discrete logarithms on a quantum computer. *SIAM Review*, 41(2):303–332, 1999. [Cited on page 1.]

[6] Frank Arute, Kunal Arya, Ryan Babbush, Dave Bacon, Joseph C. Bardin, Rami Barends, Rupak Biswas, Sergio Boixo, Fernando G. S. L. Brandao, David A. Buell, Brian Burkett, Yu Chen, Zijun Chen, Ben Chiaro, Roberto Collins, William Courtney, Andrew Dunsworth, Edward Farhi, Brooks Foxen, Austin Fowler, Craig Gidney, Marissa Giustina, Rob Graff, Keith Guerin, Steve Habegger, Matthew P. Harrigan, Michael J. Hartmann, Alan Ho, Markus Hoffmann, Trent Huang, Travis S. Humble, Sergei V. Isakov, Evan Jeffrey, Zhang Jiang, Dvir Kafri, Kostyantyn Kechedzhi, Julian Kelly, Paul V. Klimov, Sergey Knysh, Alexander Korotkov, Fedor Kostritsa, David Landhuis, Mike Lindmark, Erik Lucero, Dmitry Lyakh, Salvatore Mandrà, Jarrod R. McClean, Matthew McEwen, Anthony Megrant, Xiao Mi, Kristel Michielsen, Masoud Mohseni, Josh Mutus, Ofer Naaman, Matthew Neeley, Charles Neill, Murphy Yuezhen Niu, Eric Ostby, Andre Petukhov, John C. Platt, Chris Quintana, Eleanor G. Rieffel, Pedram Roushan, Nicholas C. Rubin, Daniel Sank, Kevin J. Satzinger, Vadim Smelyanskiy, Kevin J. Sung, Matthew D. Trevithick, Amit Vainsencher, Benjamin Villalonga, Theodore White, Z. Jamie Yao, Ping Yeh, Adam Zalcman, Hartmut Neven, and John M. Martinis. Quantum supremacy using a programmable superconducting processor. *Nature*, 574(7779):505–510, 2019. [Cited on page 1.]

[7] Yulin Wu, Wan-Su Bao, Sirui Cao, Fusheng Chen, Ming-Cheng Chen, Xiawei Chen, Tung-Hsun Chung, Hui Deng, Yajie Du, Daojin Fan, Ming Gong, Cheng Guo, Chu Guo, Shaojun Guo, Lianchen Han, Linyin Hong, He-Liang Huang, Yong-Heng Huo, Liping Li, Na Li, Shaowei Li, Yuan Li, Futian Liang, Chun Lin, Jin Lin, Haoran Qian, Dan Qiao, Hao Rong, Hong Su, Lihua Sun, Liangyuan Wang, Shiyu Wang, Dachao Wu, Yu Xu, Kai Yan, Weifeng Yang, Yang Yang, Yangsen Ye, Jianghan Yin, Chong Ying, Jiale Yu, Chen Zha, Cha Zhang, Haibin Zhang, Kaili Zhang, Yiming Zhang, Han Zhao, Youwei Zhao, Liang Zhou, Qingling Zhu, Chao-Yang Lu, Cheng-Zhi Peng, Xiaobo Zhu, and Jian-Wei Pan. Strong quantum computational advantage using a superconducting quantum processor. *Phys. Rev. Lett.*, 127:180501, October 2021. [Cited on page 1.]

[8] Lars S. Madsen, Fabian Laudenbach, Mohsen Falamarzi. Askarani, Fabien Rortais, Trevor Vincent, Jacob F. F. Bulmer, Filippo M. Miatto, Leonhard Neuhaus, Lukas G. Helt, Matthew J. Collins, Adriana E. Lita, Thomas Gerrits, Sae Woo Nam, Varun D. Vaidya, Matteo Menotti, Ish Dhand, Zachary Vernon, Nicolás Quesada, and Jonathan Lavoie. Quantum computational advantage with a programmable photonic processor. *Nature*, 606(7912):75–81, 2022. [Cited on page 1.]

[9] C. L. Degen, F. Reinhard, and P. Cappellaro. Quantum sensing. *Rev. Mod. Phys.*, 89:035002, July 2017. [Cited on page 2.]

[10] Mouzhe Xie, Xiaofei Yu, Lila V. H. Rodgers, Daohong Xu, Ignacio Chi-Durán, Adrien Toros, Niels Quack, Nathalie P. de Leon, and Peter C. Maurer. Biocompatible surface functionalization architecture for a diamond quantum sensor. *Proceedings of the National Academy of Sciences*, 119(8):e2114186119, 2022. [Cited on page 2.]

[11] Nicolas Gisin and Rob Thew. Quantum communication. *Nature Photonics*, 1(3):165–171, 2007. [Cited on pages 2 and 61.]

[12] Juan Yin, Yuan Cao, Yu-Huai Li, Sheng-Kai Liao, Liang Zhang, Ji-Gang Ren, Wen-Qi Cai, Wei-Yue Liu, Bo Li, Hui Dai, Guang-Bing Li, Qi-Ming Lu, Yun-Hong Gong, Yu Xu, Shuang-Lin Li, Feng-Zhi Li, Ya-Yun Yin, Zi-Qing Jiang, Ming Li, Jian-Jun Jia, Ge Ren, Dong He, Yi-Lin Zhou, Xiao-Xiang Zhang, Na Wang, Xiang Chang, Zhen-Cai Zhu, Nai-Le Liu, Yu-Ao Chen, Chao-Yang Lu, Rong Shu, Cheng-Zhi Peng, Jian-Yu Wang, and Jian-Wei Pan. Satellite-based entanglement distribution over 1200 kilometers. *Science*, 356(6343):1140–1144, 2017. [Cited on pages 2 and 62.]

[13] Artur K. Ekert. Quantum cryptography based on Bell's theorem. *Phys. Rev. Lett.*, 67:661–663, August 1991. [Cited on pages 2 and 61.]

[14] H. J. Kimble. The quantum internet. *Nature*, 453(7198):1023–1030, 2008. [Cited on pages 2 and 61.]

[15] P. Krantz, M. Kjaergaard, F. Yan, T. P. Orlando, S. Gustavsson, and W. D. Oliver. A quantum engineer's guide to superconducting qubits. *Applied Physics Reviews*, 6(2):021318, 2019. [Cited on pages 3, 13, 18, 19, 23, 27, 32, 35, 143, and 144.]

[16] David Isaac Schuster. *Circuit Quantum Electrodynamics*. PhD thesis, Yale University, 2007. [Cited on pages 3, 13, and 24.]

[17] Kevin Joseph Satzinger. *Quantum control of surface acoustic wave phonons*. PhD thesis, University of California, Santa Barbara, 2018. [Cited on pages 3, 10, 11, 17, 85, 96, 114, and 142.]

[18] Youpeng Zhong. *Violating Bell's inequality with remotely-connected superconducting qubits*. PhD thesis, The University of Chicago, 2019. [Cited on pages 3, 5, 17, 22, 29, 68, 92, 96, 114, and 150.]

[19] Michael Tinkham. *Introduction to superconductivity*. Courier Corporation, 2004. [Cited on pages 3 and 14.]

[20] Leon N. Cooper. Bound electron pairs in a degenerate fermi gas. *Phys. Rev.*, 104:1189–1190, November 1956. [Cited on page 3.]

[21] C. R. H. McRae, H. Wang, J. Gao, M. R. Vissers, T. Brecht, A. Dunsworth, D. P. Pappas, and J. Mutus. Materials loss measurements using superconducting microwave resonators. *Review of Scientific Instruments*, 91(9):091101, 2020. [Cited on page 4.]

[22] Alexander P. M. Place, Lila V. H. Rodgers, Pranav Mundada, Basil M. Smitham, Mattias Fitzpatrick, Zhaoqi Leng, Anjali Premkumar, Jacob Bryon, Andrei Vrajitoarea, Sara Sussman, Guangming Cheng, Trisha Madhavan, Harshvardhan K. Babla, Xuan Hoang Le, Youqi Gang, Berthold Jäck, András Gyenis, Nan Yao, Robert J. Cava, Nathalie P. de Leon, and Andrew A. Houck. New material platform for superconducting transmon qubits with coherence times exceeding 0.3 milliseconds. *Nature Communications*, 12(1):1779, March 2021. [Cited on pages 4 and 120.]

[23] Russell A McLellan, Aveek Dutta, Chenyu Zhou, Yichen Jia, Conan Weiland, Xin Gui, Alexander PM Place, Kevin D Crowley, Xuan Hoang Le, Trisha Madhavan, et al. Chemical profiles of the oxides on tantalum in state of the art superconducting circuits. *arXiv preprint arXiv:2301.04567*, 2023. [Cited on page 4.]

[24] John F. Cochran and D. E. Mapother. Superconducting transition in aluminum. *Phys. Rev.*, 111:132–142, Jul 1958. [Cited on pages 4 and 122.]

[25] B. L. Blackford and R. H. March. Temperature dependence of the energy gap in superconducting al–al2o3–al tunnel junctions. *Canadian Journal of Physics*, 46(2):141–145, 1968. [Cited on page 4.]

[26] Aaron D. O'Connell, M. Ansmann, R. C. Bialczak, M. Hofheinz, N. Katz, Erik Lucero, C. McKenney, M. Neeley, H. Wang, E. M. Weig, A. N. Cleland, and J. M. Martinis. Microwave dielectric loss at single photon energies and millikelvin temperatures. *Applied Physics Letters*, 92(11):112903, 2008. [Cited on page 4.]

[27] David M Pozar. *Microwave engineering*. John Wiley & Sons, 2009. [Cited on pages 5, 8, 44, 45, 51, 54, 68, 70, and 141.]

[28] Byeong Ho Eom, Peter K. Day, Henry G. LeDuc, and Jonas Zmuidzinas. A wideband, low-noise superconducting amplifier with high dynamic range. *Nature Physics*, 8(8):623–627, August 2012. [Cited on page 9.]

[29] Bernard Yurke and John S. Denker. Quantum network theory. *Phys. Rev. A*, 29:1419–1437, Mar 1984. [Cited on page 10.]

[30] Uri Vool and Michel Devoret. Introduction to quantum electromagnetic circuits. *International Journal of Circuit Theory and Applications*, 45(7):897–934, 2017. [Cited on pages 10 and 17.]

[31] Sihao Huang, Benjamin Lienhard, Greg Calusine, Antti Vepsäläinen, Jochen Braumüller, David K. Kim, Alexander J. Melville, Bethany M. Niedzielski, Jonilyn L.

Yoder, Bharath Kannan, Terry P. Orlando, Simon Gustavsson, and William D. Oliver. Microwave package design for superconducting quantum processors. *PRX Quantum*, 2:020306, Apr 2021. [Cited on pages 10 and 78.]

[32] A. Dunsworth, R. Barends, Yu Chen, Zijun Chen, B. Chiaro, A. Fowler, B. Foxen, E. Jeffrey, J. Kelly, P. V. Klimov, E. Lucero, J. Y. Mutus, M. Neeley, C. Neill, C. Quintana, P. Roushan, D. Sank, A. Vainsencher, J. Wenner, T. C. White, H. Neven, John M. Martinis, and A. Megrant. A method for building low loss multi-layer wiring for superconducting microwave devices. *Applied Physics Letters*, 112(6):063502, 2018. [Cited on page 11.]

[33] A. Megrant, C. Neill, R. Barends, B. Chiaro, Yu Chen, L. Feigl, J. Kelly, Erik Lucero, Matteo Mariantoni, P. J. J. O'Malley, D. Sank, A. Vainsencher, J. Wenner, T. C. White, Y. Yin, J. Zhao, C. J. Palmstrøm, John M. Martinis, and A. N. Cleland. Planar superconducting resonators with internal quality factors above one million. *Applied Physics Letters*, 100(11):113510, 2012. [Cited on pages 11 and 122.]

[34] Audrey Bienfait. *Magnetic Resonance with Quantum Microwaves*. PhD thesis, Universite Paris-Saclay, 2016. [Cited on pages 13 and 35.]

[35] B.D. Josephson. Possible new effects in superconductive tunnelling. *Physics Letters*, 1(7):251 – 253, 1962. [Cited on page 13.]

[36] W. C. Stewart. Current-voltage characteristics of Josephson junctions. *Applied Physics Letters*, 12(8):277–280, 1968. [Cited on page 14.]

[37] D. E. McCumber. Tunneling and weak-link superconductor phenomena having potential device applications. *Journal of Applied Physics*, 39(6):2503–2508, 1968. [Cited on page 14.]

[38] John Clarke and Alex I Braginski. *The SQUID Handbook, 1: Fundamentals and Technology of SQUIDs and SQUID Systems*, volume 1. Wiley-Vch, 2004. [Cited on page 15.]

[39] Michael R. Geller, Emmanuel Donate, Yu Chen, Michael T. Fang, Nelson Leung, Charles Neill, Pedram Roushan, and John M. Martinis. Tunable coupler for superconducting Xmon qubits: Perturbative nonlinear model. *Phys. Rev. A*, 92:012320, Jul 2015. [Cited on pages 16 and 65.]

[40] R. Barends, J. Kelly, A. Megrant, D. Sank, E. Jeffrey, Y. Chen, Y. Yin, B. Chiaro, J. Mutus, C. Neill, P. O'Malley, P. Roushan, J. Wenner, T. C. White, A. N. Cleland, and John M. Martinis. Coherent Josephson qubit suitable for scalable quantum integrated circuits. *Phys. Rev. Lett.*, 111:080502, Aug 2013. [Cited on pages 16 and 19.]

[41] K. J. Satzinger, Y. P. Zhong, H.-S. Chang, G. A. Peairs, A. Bienfait, Ming-Han Chou, A. Y. Cleland, C. R. Conner, É. Dumur, J. Grebel, I. Gutierrez, B. H. November, R. G. Povey, S. J. Whiteley, D. D. Awschalom, D. I. Schuster, and A. N. Cleland. Quantum control of surface acoustic-wave phonons. *Nature*, 563(7733):661–665, November 2018. [Cited on page 17.]

[42] A. Bienfait, K. J. Satzinger, Y. P. Zhong, H.-S. Chang, M.-H. Chou, C. R. Conner, É. Dumur, J. Grebel, G. A. Peairs, R. G. Povey, and A. N. Cleland. Phonon-mediated quantum state transfer and remote qubit entanglement. *Science*, 364(6438):368–371, 2019. [Cited on pages 17, 71, 93, and 140.]

[43] A. Bienfait, Y. P. Zhong, H.-S. Chang, M.-H. Chou, C. R. Conner, É. Dumur, J. Grebel, G. A. Peairs, R. G. Povey, K. J. Satzinger, and A. N. Cleland. Quantum erasure using entangled surface acoustic phonons. *Phys. Rev. X*, 10:021055, Jun 2020. [Cited on pages 17 and 140.]

[44] Y. P. Zhong, H.-S. Chang, K. J. Satzinger, M.-H. Chou, A. Bienfait, C. R. Conner, É. Dumur, J. Grebel, G. A. Peairs, R. G. Povey, D. I. Schuster, and A. N. Cleland. Violating Bell's inequality with remotely connected superconducting qubits. *Nature Physics*, April 2019. [Cited on pages 17, 64, 65, 66, 70, 75, 93, and 96.]

[45] H.-S. Chang, Y. P. Zhong, A. Bienfait, M.-H. Chou, C. R. Conner, É. Dumur, J. Grebel, G. A. Peairs, R. G. Povey, K. J. Satzinger, and A. N. Cleland. Remote entanglement via adiabatic passage using a tunably dissipative quantum communication system. *Phys. Rev. Lett.*, 124:240502, Jun 2020. [Cited on pages 17 and 63.]

[46] Youpeng Zhong, Hung-Shen Chang, Audrey Bienfait, Étienne Dumur, Ming-Han Chou, Christopher R. Conner, Joel Grebel, Rhys G. Povey, Haoxiong Yan, David I. Schuster, and Andrew N. Cleland. Deterministic multi-qubit entanglement in a quantum network. *Nature*, 590(7847):571–575, February 2021. [Cited on pages 17 and 63.]

[47] Yu Chen, C. Neill, P. Roushan, N. Leung, M. Fang, R. Barends, J. Kelly, B. Campbell, Z. Chen, B. Chiaro, A. Dunsworth, E. Jeffrey, A. Megrant, J. Y. Mutus, P. J. J. O'Malley, C. M. Quintana, D. Sank, A. Vainsencher, J. Wenner, T. C. White, Michael R. Geller, A. N. Cleland, and John M. Martinis. Qubit architecture with high coherence and fast tunable coupling. *Phys. Rev. Lett.*, 113:220502, Nov 2014. [Cited on pages 17, 65, and 97.]

[48] David P DiVincenzo. The physical implementation of quantum computation. *Fortschritte der Physik: Progress of Physics*, 48(9-11):771–783, 2000. [Cited on page 17.]

[49] Y. Nakamura, Yu. A. Pashkin, and J. S. Tsai. Coherent control of macroscopic quantum states in a single-cooper-pair box. *Nature*, 398:786, April 1999. [Cited on page 18.]

[50] Jens Koch, Terri M. Yu, Jay Gambetta, A. A. Houck, D. I. Schuster, J. Majer, Alexandre Blais, M. H. Devoret, S. M. Girvin, and R. J. Schoelkopf. Charge-insensitive qubit design derived from the cooper pair box. *Phys. Rev. A*, 76:042319, Oct 2007. [Cited on page 18.]

[51] M. Sandberg, C. M. Wilson, F. Persson, T. Bauch, G. Johansson, V. Shumeiko, T. Duty, and P. Delsing. Tuning the field in a microwave resonator faster than the photon lifetime. *Applied Physics Letters*, 92(20):203501, 2008. [Cited on page 20.]

[52] T. Yamamoto, K. Inomata, M. Watanabe, K. Matsuba, T. Miyazaki, W. D. Oliver, Y. Nakamura, and J. S. Tsai. Flux-driven Josephson parametric amplifier. *Applied Physics Letters*, 93(4):042510, 2008. [Cited on pages 20 and 35.]

[53] Etienne Dumur. *A V-shape superconducting artificial atom for circuit quantum electrodynamics*. PhD thesis, Universite de Grenoble, 2015. [Cited on page 20.]

[54] Z. L. Wang, Y. P. Zhong, L. J. He, H. Wang, John M. Martinis, A. N. Cleland, and Q. W. Xie. Quantum state characterization of a fast tunable superconducting resonator. *Applied Physics Letters*, 102(16):163503, 2013. [Cited on pages 21, 75, and 80.]

[55] M. Wallquist, V. S. Shumeiko, and G. Wendin. Selective coupling of superconducting charge qubits mediated by a tunable stripline cavity. *Phys. Rev. B*, 74:224506, Dec 2006. [Cited on pages 21 and 22.]

[56] Christopher Eichler and Andreas Wallraff. Controlling the dynamic range of a Josephson parametric amplifier. *EPJ Quantum Technology*, 1(1):2, Jan 2014. [Cited on pages 22 and 40.]

[57] Gustav Andersson. *Quantum acoustics with superconducting circuits*. PhD thesis, Chalmers University of Technology, 2020. [Cited on page 24.]

[58] Alexander Holm Kiilerich and Klaus Mølmer. Input-output theory with quantum pulses. *Phys. Rev. Lett.*, 123:123604, Sep 2019. [Cited on pages 24 and 71.]

[59] C. W. Gardiner and M. J. Collett. Input and output in damped quantum systems: Quantum stochastic differential equations and the master equation. *Phys. Rev. A*, 31:3761–3774, Jun 1985. [Cited on pages 24 and 94.]

[60] John E. Gough and Guofeng Zhang. Generating nonclassical quantum input field states with modulating filters. *EPJ Quantum Technology*, 2(1):15, June 2015. [Cited on page 25.]

[61] Joshua Combes, Joseph Kerckhoff, and Mohan Sarovar. The slh framework for modeling quantum input-output networks. *Advances in Physics: X*, 2(3):784–888, 2017. [Cited on pages 25 and 26.]

[62] J Robert Johansson, Paul D Nation, and Franco Nori. Qutip: An open-source python framework for the dynamics of open quantum systems. *Computer Physics Communications*, 183(8):1760–1772, 2012. [Cited on page 25.]

[63] Daniel Thomas Sank. *Fast, Accurate State Measurement in Superconducting Qubits*. PhD thesis, University of California, Santa Barbara, 2014. [Cited on pages 27, 30, 140, 143, and 152.]

[64] Leandro Stefanazzi, Kenneth Treptow, Neal Wilcer, Chris Stoughton, Collin Bradford, Sho Uemura, Silvia Zorzetti, Salvatore Montella, Gustavo Cancelo, Sara Sussman, Andrew Houck, Shefali Saxena, Horacio Arnaldi, Ankur Agrawal, Helin Zhang, Chunyang

Ding, and David I. Schuster. The qick (quantum instrumentation control kit): Readout and control for qubits and detectors. *Review of Scientific Instruments*, 93(4):044709, 2022. [Cited on page 28.]

[65] Markus Ansmann. *Benchmarking the superconducting Josephson phase qubit: The violation of Bell's inequality*. PhD thesis, University of California, Santa Barbara, 2009. [Cited on page 29.]

[66] Fei Yan, Dan Campbell, Philip Krantz, Morten Kjaergaard, David Kim, Jonilyn L. Yoder, David Hover, Adam Sears, Andrew J. Kerman, Terry P. Orlando, Simon Gustavsson, and William D. Oliver. Distinguishing coherent and thermal photon noise in a circuit quantum electrodynamical system. *Phys. Rev. Lett.*, 120:260504, Jun 2018. [Cited on page 30.]

[67] J. B. Johnson. Thermal agitation of electricity in conductors. *Phys. Rev.*, 32:97–109, Jul 1928. [Cited on page 30.]

[68] Bishnu Patra, Rosario M. Incandela, Jeroen P. G. van Dijk, Harald A. R. Homulle, Lin Song, Mina Shahmohammadi, Robert Bogdan Staszewski, Andrei Vladimirescu, Masoud Babaie, Fabio Sebastiano, and Edoardo Charbon. Cryo-cmos circuits and systems for quantum computing applications. *IEEE Journal of Solid-State Circuits*, 53(1):309–321, 2018. [Cited on page 31.]

[69] Kurtis Lee Geerlings. *Improving Coherence of Superconducting Qubits and Resonators*. PhD thesis, Yale University, 2013. [Cited on page 31.]

[70] H. T. Friis. Noise figures of radio receivers. *Proceedings of the IRE*, 32(7):419–422, July 1944. [Cited on page 31.]

[71] Carlton M. Caves. Quantum limits on noise in linear amplifiers. *Phys. Rev. D*, 26:1817–1839, Oct 1982. [Cited on pages 32 and 109.]

[72] Manuel Angel Castellanos-Beltran. *Development of a Josephson Parametric Amplifier for the Preparation and Detection of Nonclassical States of Microwave Fields*. PhD thesis, University of Colorado, 2010. [Cited on pages 33, 35, 37, and 38.]

[73] J. Y. Mutus, T. C. White, R. Barends, Yu Chen, Z. Chen, B. Chiaro, A. Dunsworth, E. Jeffrey, J. Kelly, A. Megrant, C. Neill, P. J. J. O'Malley, P. Roushan, D. Sank, A. Vainsencher, J. Wenner, K. M. Sundqvist, A. N. Cleland, and John M. Martinis. Strong environmental coupling in a Josephson parametric amplifier. *Applied Physics Letters*, 104(26):263513, 2014. [Cited on pages 34 and 54.]

[74] V. E. Manucharyan, E. Boaknin, M. Metcalfe, R. Vijay, I. Siddiqi, and M. Devoret. Microwave bifurcation of a Josephson junction: Embedding-circuit requirements. *Phys. Rev. B*, 76:014524, Jul 2007. [Cited on page 34.]

[75] Christopher Eichler. *Experimental Characterization of Quantum Microwave Radiation and its Entanglement with a Superconducting Qubit*. PhD thesis, ETH Zurich, 2013. [Cited on pages 34 and 35.]

[76] Jose Aumentado. Superconducting parametric amplifiers: The state of the art in Josephson parametric amplifiers. *IEEE Microwave Magazine*, 21(8):45–59, 2020. [Cited on page 35.]

[77] B. Yurke, L. R. Corruccini, P. G. Kaminsky, L. W. Rupp, A. D. Smith, A. H. Silver, R. W. Simon, and E. A. Whittaker. Observation of parametric amplification and deamplification in a Josephson parametric amplifier. *Phys. Rev. A*, 39:2519–2533, Mar 1989. [Cited on page 35.]

[78] I. Siddiqi, R. Vijay, F. Pierre, C. M. Wilson, M. Metcalfe, C. Rigetti, L. Frunzio, and M. H. Devoret. RF-driven Josephson bifurcation amplifier for quantum measurement. *Phys. Rev. Lett.*, 93:207002, Nov 2004. [Cited on page 35.]

[79] M. A. Castellanos-Beltran and K. W. Lehnert. Widely tunable parametric amplifier based on a superconducting quantum interference device array resonator. *Applied Physics Letters*, 91(8):083509, 2007. [Cited on page 35.]

[80] N. Bergeal, F. Schackert, M. Metcalfe, R. Vijay, V. E. Manucharyan, L. Frunzio, D. E. Prober, R. J. Schoelkopf, S. M. Girvin, and M. H. Devoret. Phase-preserving amplification near the quantum limit with a Josephson ring modulator. *Nature*, 465:64, May 2010. [Cited on page 35.]

[81] R. Vijay, D. H. Slichter, and I. Siddiqi. Observation of quantum jumps in a superconducting artificial atom. *Phys. Rev. Lett.*, 106:110502, Mar 2011. [Cited on page 35.]

[82] Andrew Wilson Eddins. *Superconducting Circuits for Quantum Metrology with Nonclassical Light*. PhD thesis, University of California, Santa Barbara, 2017. [Cited on pages 35, 36, 37, and 98.]

[83] Rajamani Vijayaraghavan. *Josephson Bifurcation Amplifier: Amplifying quantum signals using a dynamical bifurcation*. PhD thesis, Yale University, 2008. [Cited on pages 35 and 38.]

[84] Samuel Boutin, David M. Toyli, Aditya V. Venkatramani, Andrew W. Eddins, Irfan Siddiqi, and Alexandre Blais. Effect of higher-order nonlinearities on amplification and squeezing in Josephson parametric amplifiers. *Phys. Rev. Applied*, 8:054030, Nov 2017. [Cited on pages 35, 38, and 40.]

[85] Stephen Wirkus, Richard Rand, and Andy Ruina. How to pump a swing. *The College Mathematics Journal*, 29(4):266–275, 1998. [Cited on page 35.]

[86] N. E. Frattini, V. V. Sivak, A. Lingenfelter, S. Shankar, and M. H. Devoret. Optimizing the nonlinearity and dissipation of a snail parametric amplifier for dynamic range. *Phys. Rev. Applied*, 10:054020, Nov 2018. [Cited on page 40.]

[87] Theodore White, Alex Opremcak, George Sterling, Alexander Korotkov, Daniel Sank, Rajeev Acharya, Markus Ansmann, Frank Arute, Kunal Arya, Joseph C. Bardin, Andreas Bengtsson, Alexandre Bourassa, Jenna Bovaird, Leon Brill, Bob B. Buckley,

David A. Buell, Tim Burger, Brian Burkett, Nicholas Bushnell, Zijun Chen, Ben Chiaro, Josh Cogan, Roberto Collins, Alexander L. Crook, Ben Curtin, Sean Demura, Andrew Dunsworth, Catherine Erickson, Reza Fatemi, Leslie Flores Burgos, Ebrahim Forati, Brooks Foxen, William Giang, Marissa Giustina, Alejandro Grajales Dau, Michael C. Hamilton, Sean D. Harrington, Jeremy Hilton, Markus Hoffmann, Sabrina Hong, Trent Huang, Ashley Huff, Justin Iveland, Evan Jeffrey, Mária Kieferová, Seon Kim, Paul V. Klimov, Fedor Kostritsa, John Mark Kreikebaum, David Landhuis, Pavel Laptev, Lily Laws, Kenny Lee, Brian J. Lester, Alexander Lill, Wayne Liu, Aditya Locharla, Erik Lucero, Trevor McCourt, Matt McEwen, Xiao Mi, Kevin C. Miao, Shirin Montazeri, Alexis Morvan, Matthew Neeley, Charles Neill, Ani Nersisyan, Jiun How Ng, Anthony Nguyen, Murray Nguyen, Rebecca Potter, Chris Quintana, Pedram Roushan, Kannan Sankaragomathi, Kevin J. Satzinger, Christopher Schuster, Michael J. Shearn, Aaron Shorter, Vladimir Shvarts, Jindra Skruzny, W. Clarke Smith, Marco Szalay, Alfredo Torres, Bryan W. K. Woo, Z. Jamie Yao, Ping Yeh, Juhwan Yoo, Grayson Young, Ningfeng Zhu, Nicholas Zobrist, Yu Chen, Anthony Megrant, Julian Kelly, and Ofer Naaman. Readout of a quantum processor with high dynamic range Josephson parametric amplifiers. *Applied Physics Letters*, 122(1):014001, 2023. [Cited on pages 40 and 54.]

[88] K. M. Sundqvist, S. Kintaş, M. Simoen, P. Krantz, M. Sandberg, C. M. Wilson, and P. Delsing. The pumpistor: A linearized model of a flux-pumped superconducting quantum interference device for use as a negative-resistance parametric amplifier. *Applied Physics Letters*, 103(10):102603, 2013. [Cited on page 42.]

[89] Kyle M. Sundqvist and Per Delsing. Negative-resistance models for parametrically flux-pumped superconducting quantum interference devices. *EPJ Quantum Technology*, 1(1):6, Mar 2014. [Cited on pages 42 and 43.]

[90] J. Y. Mutus, T. C. White, E. Jeffrey, D. Sank, R. Barends, J. Bochmann, Yu Chen, Z. Chen, B. Chiaro, A. Dunsworth, J. Kelly, A. Megrant, C. Neill, P. J. J. O'Malley, P. Roushan, A. Vainsencher, J. Wenner, I. Siddiqi, R. Vijay, A. N. Cleland, and John M. Martinis. Design and characterization of a lumped element single-ended superconducting microwave parametric amplifier with on-chip flux bias line. *Appl. Phys. Lett.*, 103(12):122602, January 2013. [Cited on pages 49, 54, and 59.]

[91] M. A. Castellanos-Beltran, K. D. Irwin, G. C. Hilton, L. R. Vale, and K. W. Lehnert. Amplification and squeezing of quantum noise with a tunable Josephson metamaterial. *Nature Physics*, 4:929, October 2008. [Cited on page 51.]

[92] C. Macklin, K. O'Brien, D. Hover, M. E. Schwartz, V. Bolkhovsky, X. Zhang, W. D. Oliver, and I. Siddiqi. A near–quantum-limited Josephson traveling-wave parametric amplifier. *Science*, 350(6258):307–310, 2015. [Cited on pages 51 and 53.]

[93] Philipp Kurpiers, Theodore Walter, Paul Magnard, Yves Salathe, and Andreas Wallraff. Characterizing the attenuation of coaxial and rectangular microwave-frequency waveguides at cryogenic temperatures. *EPJ Quantum Technology*, 4(1):8, May 2017. [Cited on page 53.]

[94] Crystek microwave: 12 ghz hand formable.086 coax cables. https://www.crystek.com/microwave/spec-sheets/rfcable/086.pdf, November 2017. [Cited on page 53.]

[95] Ez-flex.405-cu, non-magnetic. https://www.ezform.com/product/ez-flex-405-cu/, 2021. [Cited on page 53.]

[96] A. L. Cullen. A travelling-wave parametric amplifier. *Nature*, 181(4605):332–332, February 1958. [Cited on page 53.]

[97] Luca Planat, Arpit Ranadive, Rémy Dassonneville, Javier Puertas Martínez, Sébastien Léger, Cécile Naud, Olivier Buisson, Wiebke Hasch-Guichard, Denis M. Basko, and Nicolas Roch. Photonic-crystal Josephson traveling-wave parametric amplifier. *Phys. Rev. X*, 10:021021, Apr 2020. [Cited on page 53.]

[98] Tanay Roy, Suman Kundu, Madhavi Chand, A. M. Vadiraj, A. Ranadive, N. Nehra, Meghan P. Patankar, J. Aumentado, A. A. Clerk, and R. Vijay. Broadband parametric amplification with impedance engineering: Beyond the gain-bandwidth product. *Applied Physics Letters*, 107(26):262601, 2015. [Cited on pages 54, 55, 56, and 107.]

[99] Ofer Naaman and José Aumentado. Synthesis of parametrically coupled networks. *PRX Quantum*, 3:020201, May 2022. [Cited on page 55.]

[100] J. Grebel, A. Bienfait, É. Dumur, H.-S. Chang, M.-H. Chou, C. R. Conner, G. A. Peairs, R. G. Povey, Y. P. Zhong, and A. N. Cleland. Flux-pumped impedance-engineered broadband Josephson parametric amplifier. *Applied Physics Letters*, 118(14):142601, 2021. [Cited on page 56.]

[101] Hua-Lei Yin, Teng-Yun Chen, Zong-Wen Yu, Hui Liu, Li-Xing You, Yi-Heng Zhou, Si-Jing Chen, Yingqiu Mao, Ming-Qi Huang, Wei-Jun Zhang, Hao Chen, Ming Jun Li, Daniel Nolan, Fei Zhou, Xiao Jiang, Zhen Wang, Qiang Zhang, Xiang-Bin Wang, and Jian-Wei Pan. Measurement-device-independent quantum key distribution over a 404 km optical fiber. *Phys. Rev. Lett.*, 117:190501, November 2016. [Cited on page 61.]

[102] Andreas Reiserer. Colloquium: Cavity-enhanced quantum network nodes. *Rev. Mod. Phys.*, 94:041003, December 2022. [Cited on page 61.]

[103] H.-J. Briegel, W. Dür, J. I. Cirac, and P. Zoller. Quantum repeaters: The role of imperfect local operations in quantum communication. *Phys. Rev. Lett.*, 81:5932–5935, December 1998. [Cited on page 61.]

[104] William J. Munro, Koji Azuma, Kiyoshi Tamaki, and Kae Nemoto. Inside quantum repeaters. *IEEE Journal of Selected Topics in Quantum Electronics*, 21(3):78–90, 2015. [Cited on page 61.]

[105] Khabat Heshami, Duncan G. England, Peter C. Humphreys, Philip J. Bustard, Victor M. Acosta, Joshua Nunn, and Benjamin J. Sussman. Quantum memories: emerging applications and recent advances. *Journal of Modern Optics*, 63(20):2005–2028, 2016. PMID: 27695198. [Cited on page 62.]

[106] Raju Valivarthi, Samantha I. Davis, Cristián Peña, Si Xie, Nikolai Lauk, Lautaro Narváez, Jason P. Allmaras, Andrew D. Beyer, Yewon Gim, Meraj Hussein, George Iskander, Hyunseong Linus Kim, Boris Korzh, Andrew Mueller, Mandy Rominsky, Matthew Shaw, Dawn Tang, Emma E. Wollman, Christoph Simon, Panagiotis Spentzouris, Daniel Oblak, Neil Sinclair, and Maria Spiropulu. Teleportation systems toward a quantum internet. *PRX Quantum*, 1:020317, December 2020. [Cited on page 62.]

[107] Dounan Du, Paul Stankus, Olli-Pentti Saira, Mael Flament, Steven Sagona-Stophel, Mehdi Namazi, Dimitrios Katramatos, and Eden Figueroa. An elementary 158 km long quantum network connecting room temperature quantum memories. *arXiv preprint arXiv:2101.12742*, 2021. [Cited on page 62.]

[108] Joaquin Chung, Ely M. Eastman, Gregory S. Kanter, Keshav Kapoor, Nikolai Lauk, Cristián H. Peña, Robert K. Plunkett, Neil Sinclair, Jordan M. Thomas, Raju Valivarthi, Si Xie, Rajkumar Kettimuthu, Prem Kumar, Panagiotis Spentzouris, and Maria Spiropulu. Design and implementation of the illinois express quantum metropolitan area network. *IEEE Transactions on Quantum Engineering*, 3:1–20, 2022. [Cited on page 62.]

[109] Joshua Ramette, Josiah Sinclair, Nikolas P Breuckmann, and Vladan Vuletić. Fault-tolerant connection of error-corrected qubits with noisy links. *arXiv preprint arXiv:2302.01296*, 2023. [Cited on page 63.]

[110] P. Magnard, S. Storz, P. Kurpiers, J. Schär, F. Marxer, J. Lütolf, T. Walter, J.-C. Besse, M. Gabureac, K. Reuer, A. Akin, B. Royer, A. Blais, and A. Wallraff. Microwave quantum link between superconducting circuits housed in spatially separated cryogenic systems. *Phys. Rev. Lett.*, 125:260502, December 2020. [Cited on page 63.]

[111] Luke D. Burkhart, James D. Teoh, Yaxing Zhang, Christopher J. Axline, Luigi Frunzio, M.H. Devoret, Liang Jiang, S.M. Girvin, and R.J. Schoelkopf. Error-detected state transfer and entanglement in a superconducting quantum network. *PRX Quantum*, 2:030321, August 2021. [Cited on pages 63, 66, and 108.]

[112] Jingjing Niu, Libo Zhang, Yang Liu, Jiawei Qiu, Wenhui Huang, Jiaxiang Huang, Hao Jia, Jiawei Liu, Ziyu Tao, Weiwei Wei, Yuxuan Zhou, Wanjing Zou, Yuanzhen Chen, Xiaowei Deng, Xiuhao Deng, Changkang Hu, Ling Hu, Jian Li, Dian Tan, Yuan Xu, Fei Yan, Tongxing Yan, Song Liu, Youpeng Zhong, Andrew N. Cleland, and Dapeng Yu. Low-loss interconnects for modular superconducting quantum processors. *Nature Electronics*, 2023. [Cited on page 63.]

[113] M. Stobińska, G. Alber, and G. Leuchs. Perfect excitation of a matter qubit by a single photon in free space. *EPL (Europhysics Letters)*, 86(1):14007, April 2009. [Cited on pages 63 and 64.]

[114] J. I. Cirac, P. Zoller, H. J. Kimble, and H. Mabuchi. Quantum state transfer and entanglement distribution among distant nodes in a quantum network. *Phys. Rev. Lett.*, 78:3221–3224, Apr 1997. [Cited on pages 63 and 64.]

[115] P. Kurpiers, P. Magnard, T. Walter, B. Royer, M. Pechal, J. Heinsoo, Y. Salathé, A. Akin, S. Storz, J.-C. Besse, S. Gasparinetti, A. Blais, and A. Wallraff. Deterministic quantum state transfer and remote entanglement using microwave photons. *Nature*, 558(7709):264–267, June 2018. [Cited on pages 64 and 65.]

[116] P. Campagne-Ibarcq, E. Zalys-Geller, A. Narla, S. Shankar, P. Reinhold, L. Burkhart, C. Axline, W. Pfaff, L. Frunzio, R. J. Schoelkopf, and M. H. Devoret. Deterministic remote entanglement of superconducting circuits through microwave two-photon transitions. *Phys. Rev. Lett.*, 120:200501, May 2018. [Cited on pages 64 and 65.]

[117] Christopher J. Axline, Luke D. Burkhart, Wolfgang Pfaff, Mengzhen Zhang, Kevin Chou, Philippe Campagne-Ibarcq, Philip Reinhold, Luigi Frunzio, S. M. Girvin, Liang Jiang, M. H. Devoret, and R. J. Schoelkopf. On-demand quantum state transfer and entanglement between remote microwave cavity memories. *Nature Physics*, 14(7):705–710, July 2018. [Cited on pages 64 and 65.]

[118] Wolfgang Pfaff, Christopher J. Axline, Luke D. Burkhart, Uri Vool, Philip Reinhold, Luigi Frunzio, Liang Jiang, Michel H. Devoret, and Robert J. Schoelkopf. Controlled release of multiphoton quantum states from a microwave cavity memory. *Nature Physics*, 13(9):882–887, 2017. [Cited on page 64.]

[119] Simon E. Nigg, Hanhee Paik, Brian Vlastakis, Gerhard Kirchmair, S. Shankar, Luigi Frunzio, M. H. Devoret, R. J. Schoelkopf, and S. M. Girvin. Black-box superconducting circuit quantization. *Phys. Rev. Lett.*, 108:240502, Jun 2012. [Cited on page 70.]

[120] Stefan Krastanov, Victor V. Albert, Chao Shen, Chang-Ling Zou, Reinier W. Heeres, Brian Vlastakis, Robert J. Schoelkopf, and Liang Jiang. Universal control of an oscillator with dispersive coupling to a qubit. *Phys. Rev. A*, 92:040303, Oct 2015. [Cited on page 73.]

[121] Reinier W. Heeres, Brian Vlastakis, Eric Holland, Stefan Krastanov, Victor V. Albert, Luigi Frunzio, Liang Jiang, and Robert J. Schoelkopf. Cavity state manipulation using photon-number selective phase gates. *Phys. Rev. Lett.*, 115:137002, Sep 2015. [Cited on page 73.]

[122] Yu xi Liu, L. F. Wei, and Franco Nori. Generation of nonclassical photon states using a superconducting qubit in a microcavity. *Europhysics Letters*, 67(6):941, September 2004. [Cited on pages 73 and 98.]

[123] Max Hofheinz, E. M. Weig, M. Ansmann, Radoslaw C. Bialczak, Erik Lucero, M. Neeley, A. D. O'Connell, H. Wang, John M. Martinis, and A. N. Cleland. Generation of fock states in a superconducting quantum circuit. *Nature*, 454:310, July 2008. [Cited on page 73.]

[124] Max Hofheinz, H. Wang, M. Ansmann, Radoslaw C. Bialczak, Erik Lucero, M. Neeley, A. D. O'Connell, D. Sank, J. Wenner, John M. Martinis, and A. N. Cleland. Synthesizing arbitrary quantum states in a superconducting resonator. *Nature*, 459:546, May 2009. [Cited on pages 73 and 98.]

[125] H. Wang, Matteo Mariantoni, Radoslaw C. Bialczak, M. Lenander, Erik Lucero, M. Neeley, A. D. O'Connell, D. Sank, M. Weides, J. Wenner, T. Yamamoto, Y. Yin, J. Zhao, John M. Martinis, and A. N. Cleland. Deterministic entanglement of photons in two superconducting microwave resonators. *Phys. Rev. Lett.*, 106:060401, February 2011. [Cited on pages 73, 98, 103, and 104.]

[126] Nathan R. A. Lee, Marek Pechal, E. Alex Wollack, Patricio Arrangoiz-Arriola, Zhaoyou Wang, and Amir H. Safavi-Naeni. Propagation of microwave photons along a synthetic dimension. *Phys. Rev. A*, 101:053807, May 2020. [Cited on page 75.]

[127] Martina Esposito, Arpit Ranadive, Luca Planat, and Nicolas Roch. Perspective on traveling wave microwave parametric amplifiers. *Appl. Phys. Lett.*, 119(12):120501, September 2021. [Cited on page 80.]

[128] A. Wallraff, D. I. Schuster, A. Blais, J. M. Gambetta, J. Schreier, L. Frunzio, M. H. Devoret, S. M. Girvin, and R. J. Schoelkopf. Sideband transitions and two-tone spectroscopy of a superconducting qubit strongly coupled to an on-chip cavity. *Phys. Rev. Lett.*, 99:050501, July 2007. [Cited on pages 80 and 148.]

[129] Zijun Chen. *Metrology of quantum control and measurement in superconducting qubits*. PhD thesis, University of California, Santa Barbara, 2018. [Cited on page 82.]

[130] Charles James Neill. *A path towards quantum supremacy with superconducting qubits*. PhD thesis, University of California, Santa Barbara, 2017. [Cited on page 85.]

[131] Fernando Nogueira. Bayesian Optimization: Open source constrained global optimization tool for Python, 2014–. [Cited on page 93.]

[132] Serge Haroche and J-M Raimond. *Exploring the quantum: atoms, cavities, and photons*. Oxford university press, 2006. [Cited on page 97.]

[133] P. Bertet, A. Auffeves, P. Maioli, S. Osnaghi, T. Meunier, M. Brune, J. M. Raimond, and S. Haroche. Direct measurement of the wigner function of a one-photon fock state in a cavity. *Phys. Rev. Lett.*, 89:200402, October 2002. [Cited on page 98.]

[134] Brian Vlastakis, Gerhard Kirchmair, Zaki Leghtas, Simon E. Nigg, Luigi Frunzio, S. M. Girvin, Mazyar Mirrahimi, M. H. Devoret, and R. J. Schoelkopf. Deterministically encoding quantum information using 100-photon schrödinger cat states. *Science*, 342(6158):607–610, 2013. [Cited on page 98.]

[135] E. Alex Wollack, Agnetta Y. Cleland, Rachel G. Gruenke, Zhaoyou Wang, Patricio Arrangoiz-Arriola, and Amir H. Safavi-Naeini. Quantum state preparation and tomography of entangled mechanical resonators. *Nature*, 604(7906):463–467, 2022. [Cited on page 98.]

[136] Michael Grant and Stephen Boyd. CVX: Matlab software for disciplined convex programming, version 2.1. http://cvxr.com/cvx, March 2014. [Cited on pages 98 and 104.]

[137] Ingrid Strandberg. Simple, reliable, and noise-resilient continuous-variable quantum state tomography with convex optimization. *Phys. Rev. Appl.*, 18:044041, October 2022. [Cited on page 98.]

[138] Michael A Nielsen and Isaac Chuang. Quantum computation and quantum information, 2002. [Cited on page 101.]

[139] Agedi N. Boto, Pieter Kok, Daniel S. Abrams, Samuel L. Braunstein, Colin P. Williams, and Jonathan P. Dowling. Quantum interferometric optical lithography: Exploiting entanglement to beat the diffraction limit. *Phys. Rev. Lett.*, 85:2733–2736, September 2000. [Cited on page 103.]

[140] Itai Afek, Oron Ambar, and Yaron Silberberg. High-noon states by mixing quantum and classical light. *Science*, 328(5980):879–881, 2010. [Cited on page 103.]

[141] Connor T. Hann, Chang-Ling Zou, Yaxing Zhang, Yiwen Chu, Robert J. Schoelkopf, S. M. Girvin, and Liang Jiang. Hardware-efficient quantum random access memory with hybrid quantum acoustic systems. *Phys. Rev. Lett.*, 123:250501, December 2019. [Cited on page 108.]

[142] Hung-Shen Chang. *Remote entanglement via adiabatic passage using a tunably dissipative quantum communication system*. PhD thesis, The University of Chicago, 2021. [Cited on page 114.]

[143] Ming-Han Chou. *Quantum measurements of microwave-frequency acoustic resonators with superconducting circuits*. PhD thesis, The University of Chicago, 2023. [Cited on page 114.]

[144] Josephine B. Chang, Michael R. Vissers, Antonio D. Córcoles, Martin Sandberg, Jiansong Gao, David W. Abraham, Jerry M. Chow, Jay M. Gambetta, Mary Beth Rothwell, George A. Keefe, Matthias Steffen, and David P. Pappas. Improved superconducting qubit coherence using titanium nitride. *Applied Physics Letters*, 103(1):012602, 2013. [Cited on page 120.]

[145] B. T. Matthias, T. H. Geballe, and V. B. Compton. Superconductivity. *Rev. Mod. Phys.*, 35:1–22, January 1963. [Cited on page 122.]

[146] A. A. Houck, J. A. Schreier, B. R. Johnson, J. M. Chow, Jens Koch, J. M. Gambetta, D. I. Schuster, L. Frunzio, M. H. Devoret, S. M. Girvin, and R. J. Schoelkopf. Controlling the spontaneous emission of a superconducting transmon qubit. *Phys. Rev. Lett.*, 101:080502, August 2008. [Cited on page 148.]

[147] Anatole Abragam. *The principles of nuclear magnetism*. Number 32. Oxford university press, 1961. [Cited on page 149.]

[148] T. Walter, P. Kurpiers, S. Gasparinetti, P. Magnard, A. Potočnik, Y. Salathé, M. Pechal, M. Mondal, M. Oppliger, C. Eichler, and A. Wallraff. Rapid high-fidelity single-shot dispersive readout of superconducting qubits. *Phys. Rev. Applied*, 7:054020, May 2017. [Cited on page 150.]

[149] A. Wallraff, D. I. Schuster, A. Blais, L. Frunzio, J. Majer, M. H. Devoret, S. M. Girvin, and R. J. Schoelkopf. Approaching unit visibility for control of a superconducting qubit with dispersive readout. *Phys. Rev. Lett.*, 95:060501, August 2005. [Cited on page 150.]

[150] F. Motzoi, J. M. Gambetta, P. Rebentrost, and F. K. Wilhelm. Simple pulses for elimination of leakage in weakly nonlinear qubits. *Phys. Rev. Lett.*, 103:110501, September 2009. [Cited on page 151.]